

1-16-2013

IR820 Nanoconjugates for Theranostic Applications

Alicia Fernandez-Fernandez

Florida International University, afern042@fiu.edu

DOI: 10.25148/etd.FI13041501

Follow this and additional works at: <https://digitalcommons.fiu.edu/etd>

Recommended Citation

Fernandez-Fernandez, Alicia, "IR820 Nanoconjugates for Theranostic Applications" (2013). *FIU Electronic Theses and Dissertations*. 819.

<https://digitalcommons.fiu.edu/etd/819>

This work is brought to you for free and open access by the University Graduate School at FIU Digital Commons. It has been accepted for inclusion in FIU Electronic Theses and Dissertations by an authorized administrator of FIU Digital Commons. For more information, please contact dcc@fiu.edu.

FLORIDA INTERNATIONAL UNIVERSITY

Miami, Florida

IR820 NANOCONJUGATES FOR THERANOSTIC APPLICATIONS

A dissertation submitted in partial fulfillment of

the requirements for the degree of

DOCTOR OF PHILOSOPHY

in

BIOMEDICAL ENGINEERING

by

Alicia Fernandez-Fernandez

2013

To: Dean Amir Mirmiran
College of Engineering and Computing

This dissertation, written by Alicia Fernandez-Fernandez, and entitled IR820 Nanoconjugates for Theranostic Applications, having been approved in respect to style and intellectual content, is referred to you for judgment.

We have read this dissertation and recommend that it be approved.

Yen-Chih Huang

Fenfei Leng

Chenzhong Li

Wei-Chiang Lin

Anthony J. McGoron , Major Professor

Date of Defense: January 16, 2013

The dissertation of Alicia Fernandez-Fernandez is approved.

Dean Amir Mirmiran
College of Engineering and Computing

Dean Lakshmi N. Reddi
University Graduate School

Florida International University, 2013

© Copyright 2013 by Alicia Fernandez-Fernandez

All rights reserved.

American Scientific Publishers and Decker Publishing kindly provided copyright permission to use material contained in the following publications as part of this dissertation, and a copy of their written permission is included in the appendices.

Fernandez-Fernandez, A., R. Manchanda, et al. (2012). Comparative study of the optical and heat generation properties of IR820 and indocyanine green. *Mol Imaging* 11(2): 99-113. Permission from American Scientific Publishers.

Manchanda, R., A. Fernandez-Fernandez, et al. (2012). Nanoplexes for cell imaging and hyperthermia: in vitro studies. *J Biomed Nanotechnol* 8(4): 686-694. Permission from Decker Publishing.

DEDICATION

I want to dedicate this dissertation to my husband Jose and my 7-year-old son Jorge, who have patiently helped me throughout this journey. When my work in the lab kept me away from my family, they continued to support me unconditionally. I was at times –more often than I’d like to admit - the mom who could not make it to soccer practice or to school events, and the wife who was cranky after a long day of experiments. My husband and my son were always there for me and were able to help me value the importance of what I was doing. My husband has been so patient with me that he truly deserves a medal. Every time I was close to giving up, he was there to make me understand how much I had invested in this process.

I know that from this experience I have not only earned a doctoral degree, but I have taught my son that where there is a will there is a way, and hard work always pays off even if it seems insurmountable at times. Although he did not really understand what I worked on, I know that he understood it was an important accomplishment. When Jorge grows up, I will remind him that he used to believe that my job as a graduate student was “to feed rats and give them water”. I am looking forward to laughing with him about it in a few years.

Jorge, Jose, sois los mejores, y os debo mucho.

ACKNOWLEDGMENTS

I would like to acknowledge my major professor Dr. Anthony McGoron, for his guidance, mentoring and endless patience. He pushed me to have my own ideas and always think critically. His mentorship helped me to overcome the difficulties and struggles of the final stretch of this dissertation. He has taught me everything I know about being a scientist, and I know that every time he asked for a little more, he was just trying to get the best out of me. I am also very grateful to my former and current lab members, especially Denny Carvajal, Romila Manchanda, and Tingjun Lei for their help throughout the years. “I could not have done it without them” is often a token sentence, but in this case, it really reflects how much they helped me in the lab and how important their friendship was outside of it. I also want to thank Dr. Leng, Dr. Li, Dr. Lin and Dr. Huang for serving in my dissertation committee and for their good advice and their patience; all your feedback and questions helped to improve this dissertation. Additionally, a warm thanks to Dr. James Byrne, who was not formally in the committee, but was there every single time I had a question or needed advice. I admire him tremendously and he has been a mentor to so many of us. I also want to thank Dr. Pradeep Kumar, Dr. Joong-Ho Moon, and Tereza Vokata for sharing their chemistry expertise to help me with formulation and characterization questions.

American Scientific Publishers and Decker Publishing allowed me to use published material from our lab group as part of this dissertation, and I would like to thank them for providing copyright permission which is also acknowledged on the copyright page.

Financial support during my Ph.D. studies was provided by a Teaching Assistantship from the Biomedical Engineering Department at FIU from 2006-2007, by the RISE program funded by NIH/NIGMS grant #R25-GM061347 from 2007-2011, and by paid employment at Nova Southeastern University from 2011-present. I would like to give thanks to Dr. Hellmann and Dr. Brown-Cross at NSU, for being supportive of my efforts and for always believing that I was able to do whatever I put my mind to.

And of course, I thank my family, to whom this dissertation is dedicated. Jose, Jorge and everyone else, who made sure I stayed on track no matter how hard it seemed, and who were always there for me. And my mom and dad, who took me to English classes when I was little, regardless of how much I complained. I hope I have made you all proud.

ABSTRACT OF THE DISSERTATION

IR820 NANOCONJUGATES FOR THERANOSTIC APPLICATIONS

by

Alicia Fernandez-Fernandez

Florida International University, 2013

Miami, Florida

Professor Anthony J. McGoron, Major Professor

Near-infrared dyes can be used as theranostic agents in cancer management based on their optical imaging and localized hyperthermia capabilities. However, their clinical translatability is limited by issues such as photobleaching, short circulation times, and non-specific biodistribution. We studied the applications of IR820 in optical imaging and hyperthermia, and we prepared nanoconjugate formulations to overcome some of the aforementioned limitations. Free IR820 can be used for optical imaging, with a strong signal still present 24 hours after i.v. injection, an elimination plasma half-life in the order of hours, and primary biodistribution to liver, lung, and kidneys. After 808-nm laser exposure, IR820 can also raise in vitro temperatures to the 41-43°C range that can selectively inhibit cancer cell growth. We conjugated IR820 with PEG-diamine via ionic interactions to create nanoconjugates (IR820-PDNCs) with diameters of approximately 50-nm per SEM and a zeta potential of 2.0 ± 0.9 mV. IR820-PDNCs enhanced cellular internalization compared to IR820 for imaging in SKOV-3, MES-SA, and Dx5 cancer cells. The nanoconjugates also significantly enhanced hyperthermia-mediated cytotoxicity in MES-SA and Dx5 compared to the free dye ($p < 0.05$). Covalent conjugation of IR820 with PEG-diamine for further stabilization resulted in

nanoconjugates (IRPDcov) that have potential for in vivo applications. Our IRPDcov formulation retained the ability to fluoresce and to cause hyperthermia-mediated cell-growth inhibition, with enhanced internalization and significantly enhanced cytotoxic hyperthermia effects compared to free dye. Additionally, IRPDcov demonstrated significantly longer ($p < 0.05$) plasma half-lives, elimination half-lives, and area-under-the-curve values compared to IR820, indicating larger overall exposure to the theranostic agent. The IRPDcov conjugate had different organ localization than free IR820, with potential reduced accumulation in the kidneys and significantly lower ($p < 0.05$) accumulation in the lungs. Some potential advantages of IR820-PEG-diamine nanoconjugates may include passive targeting of tumor tissue through the enhanced permeability and retention effect, prolonged circulation times resulting in increased windows for combined diagnosis and therapy, and further opportunities for functionalization, targeting, and customization. The conjugation of PEG-diamine with a NIR dye provides a multifunctional delivery vector whose localization can be monitored with noninvasive techniques and that may also serve for guided hyperthermia cancer treatments.

TABLE OF CONTENTS

CHAPTER	PAGE
I. INTRODUCTION, LITERATURE REVIEW, AND SPECIFIC AIMS	1
1.1. Background and Relevance.....	1
1.1.1. The field of theranostics.....	1
1.1.2. Multifunctional agents used in theranostic applications: the advantages of nanomaterials	2
1.1.3. Multifunctional agents used in theranostic applications: image-guided therapy.....	5
1.1.4. The cyanine dyes indocyanine green and IR820 and their applications in imaging and hyperthermia	7
1.2. Statement of Purpose and Specific Aims.....	11
1.2.1. Specific aim #1: IR820 in vitro characterization and theranostic applications	11
1.2.2. Specific aim #2: Formulation and characterization of ionic IR820 nanoconjugate	12
1.2.3. Specific aim #3: formulation and characterization of covalent IR820 nanoconjugate	13
1.2.4. Specific aim #4: Biodistribution studies of IRPDcov, IR820 and ICG.....	13
Chapter 1 References	15
II. METHODOLOGY	21
2.1. Materials and Methods for Specific Aim 1	21
2.1.1. Chemicals.....	21
2.1.2. Absorbance studies	21
2.1.3. Fluorescent spectrum characterization.....	22
2.1.4. Effects of temperature and light on stability in aqueous solution.....	22
2.1.5. Stability in different solvents under constant light and temperature conditions.....	23
2.1.6. Heat generation properties	24
2.1.7. Cytotoxicity with and without hyperthermia	24
2.1.8. Cellular imaging.....	27
2.1.9. Rat model studies.....	28
2.2. Materials and Methods for Specific Aim 2.....	30
2.2.1. Chemicals.....	30
2.2.2. Nanoconjugate preparation	30
2.2.3. Nanoconjugate characterization.....	31
2.2.4. Dye content determination	32
2.2.5. Characterization of absorption properties	33
2.2.6. Characterization of fluorescence properties.....	33
2.2.7. Fluorescence stability studies	33
2.2.8. Cytotoxicity with and without hyperthermia	34

2.2.9. Cellular imaging.....	35
2.3. Materials and Methods for Specific Aim 3.....	36
2.3.1. Chemicals.....	36
2.3.2. Nanoconjugate preparation.....	36
2.3.3. Nanoconjugate characterization.....	37
2.3.4. Dye content determination.....	38
2.3.5. Fluorescence stability studies.....	38
2.3.6. Cytotoxicity with and without hyperthermia.....	38
2.3.7. Cellular imaging.....	39
2.4. Materials and Methods for Specific Aim 4.....	39
Chapter 2 References.....	41
III. IR820 CHARACTERIZATION AND THERANOSTIC APPLICATIONS.....	42
3.1. Physicochemical Characterization.....	42
3.1.1. Absorbance studies.....	42
3.1.2. Fluorescence spectrum characterization.....	43
3.1.3. Effects of temperature and light on stability in aqueous solution.....	46
3.1.4. Stability in different solvents under constant light and temperature conditions.....	49
3.1.5. Hyperthermia properties.....	49
3.2. Cellular Experiments.....	50
3.2.1. Cytotoxicity experiments.....	51
3.2.2. In vitro cell imaging.....	53
3.3. In vivo Imaging Studies.....	55
3.4. Summary.....	59
Chapter 3 References.....	61
IV. PREPARATION AND CHARACTERIZATION OF IONIC IR820-PEG DIAMINE NANOCONJUGATES (IR820-PDNCs).....	63
4.1. Characterization of IR820-PDNCs.....	64
4.1.1. Absorbance studies.....	66
4.1.2. Fluorescence properties of IR820-PDNCs.....	67
4.1.3. Fluorescence stability studies.....	68
4.2. Cell Imaging Studies.....	68
4.3. Cytotoxicity Studies without Hyperthermia.....	70
4.4. Hyperthermia Studies.....	71
4.5. Summary.....	76
Chapter 4 References.....	77
V. PREPARATION AND CHARACTERIZATION OF COVALENT IR820-PEG DIAMINE NANOCONJUGATES (IRPDcov).....	79
5.1. Characterization of IRPDcov.....	79
5.1.1. Absorbance studies.....	82
5.1.2. Fluorescence properties of IRPDcov.....	82
5.1.3. Fluorescence stability studies.....	84

5.2. Cell Imaging Studies.....	84
5.3. Cytotoxicity and Hyperthermia Studies.....	86
5.4. Summary.....	90
Chapter 5 References.....	92
VI. BIODISTRIBUTION AND PHARMACOKINETIC STUDIES OF COVALENT IR820-PEG DIAMINE NANOCONJUGATE (IRPD _{cov}), IR820, AND ICG IN MICE.....	94
6.1. Study Design.....	100
6.2. Specific Methodology.....	101
6.2.1. Injection and dosage.....	101
6.2.2. Time sequence of blood and organ sampling.....	102
6.2.3. In vivo imaging techniques.....	103
6.2.4. Plasma and organ sample processing.....	103
6.2.5. Pharmacokinetic analysis of plasma data.....	104
6.3. Results and Discussion.....	106
6.3.1. Animal imaging.....	106
6.3.2. Organ imaging.....	107
6.3.3. Organ dye content.....	110
6.3.4. Plasma dye concentration.....	111
6.3.5. Pharmacokinetic modeling.....	113
6.3.6. Limitations.....	119
6.4. Summary.....	123
Chapter 6 References.....	124
VII. OVERALL DISCUSSION AND CONCLUSION.....	126
Chapter 7 References.....	134
APPENDICES.....	135
VITA.....	140

LIST OF TABLES

TABLE	PAGE
Table 1. Emission Peak Location for Aqueous Solutions of ICG and IR820.....	44
Table 2. Stability characterization of aqueous solutions of IR820 and ICG following a pseudo-first order kinetics model.....	48
Table 3. Image intensity per area in μm^2 for different locations and time points after IR820 and ICG administration	56
Table 4. Organ dye content ($\mu\text{g/g}$ tissue) 24 hours after injection.....	57
Table 5. Study design for biodistribution experiments of IRPDcov, IR820 and ICG in mice	100
Table 6. Signal intensity ratios for liver, lungs, kidneys and intestines collected 24 hours after i.v. injection of IRPDcov, IR820, or ICG	108
Table 7. Quantitative organ content 24 hours after after i.v. injection of IRPDcov, IR820, or ICG.....	111
Table 8. Plasma concentrations ($\mu\text{g/mL}$) of IRPDcov, IR820, and ICG at different time points after i.v. injection.....	112
Table 9. Pharmacokinetic parameters from one-compartment analysis of dye data in mice	115
Table 10. Pharmacokinetic parameters from two-compartment analysis of dye data in mice	116

LIST OF FIGURES

FIGURE	PAGE
Figure 1. Molecular structures of indocyanine green (A) and IR820 (B).....	9
Figure 2. Reaction scheme and formulation of ionic IR820-PEG-diamine nanoconjugate (IR820-PDNCs)	31
Figure 3. Reaction scheme and formulation of covalent IR820-PEG-diamine nanoconjugate (IRPDcov)	37
Figure 4. Absorbance spectra of IR820 and ICG in deionized water (solid) and methanol (dashed).	43
Figure 5. Fluorescence spectra after 785-nm excitation of aqueous solutions of (A) ICG and (B) IR820	44
Figure 6. Fluorescence spectra after 691-nm excitation of aqueous solutions of IR820	45
Figure 7. Effect of temperature on degradation of aqueous solutions of IR820 and ICG	47
Figure 8. Effect of light on degradation of aqueous solutions of IR820 and ICG	47
Figure 9. Heat generation profile of wells containing IR820 (A) or ICG (B) when irradiated with NIR laser for a total of 3 minutes.....	49
Figure 10. IR820 and ICG cytotoxicity and hyperthermia effects in SKOV-3 cells	51
Figure 11. IR820 and ICG cytotoxicity and hyperthermia effects in Dx5 cells	51
Figure 12. IR820 and ICG cytotoxicity and hyperthermia effects in MES-SA cells	52
Figure 13. Cellular imaging after incubation with IR820 or ICG.....	54
Figure 14. Rat abdomen images 40 minutes after i.v. injection with IR820 (A) or ICG (B), and 24 hours after injection with IR820 (C) or ICG (D)	55
Figure 15. Rat liver, lung, and kidney images 24 hours after injection with IR820 or ICG.....	57

Figure 16. SEM image of IR820-PDNCs	65
Figure 17. Absorption spectra of IR820 (solid black), IR820-PDNCs (dashed black) and PEG-diamine (gray) in deionized water	66
Figure 18. Fluorescence spectra of IR820 and IR820-PDNCs in phosphate buffered saline.....	68
Figure 19. Cellular imaging of Dx5 (A, B), SKOV-3 (C,D) and MES-SA cells (E,F) after 2.5 hour incubation with 5 μ M dye content of IR820-PDNCs (top) or IR820 (bottom); 60x, exposure time 4000 ms.....	69
Figure 20. Cytotoxicity of IR820-PDNCs or IR820 in cancer cell lines	71
Figure 21. Cytotoxicity of hyperthermia treatment with 5 μ M dye content of IR820 or IR820-PDNCs, n = 3 experiments, 4 wells/experiment.....	73
Figure 22. SEM image of IRPDcov	80
Figure 23. H-NMR spectrum of IRPDcov in deuterated methanol	81
Figure 24. Absorption spectra of IR820 (solid black), IRPDcov (dashed black) and PEG-diamine (gray) in deionized water	82
Figure 25. Fluorescence spectra of IR820 and IRPDcov in phosphate buffered saline.....	83
Figure 26. Cellular imaging of Dx5 (A, B), SKOV-3 (C,D) and MES-SA cells (E,F) after 4 hour incubation with 5 μ M dye content of IRPDcov (top) or IR820 (bottom); 60x, exposure time 4000 ms.....	85
Figure 27. Cytotoxicity of IRPDcov or IR820 in cancer cell lines, with or without hyperthermia treatment at 5 μ M dye concentration, n = 3 experiments, 4 wells/experiment	88
Figure 28. Exemplification of a one-compartment model for pharmacokinetic studies	96
Figure 29. Exemplification of a two-compartment model for pharmacokinetic studies	97
Figure 30. Images taken 15 minutes and 24 hours after i.v. injection for IRPDcov, IR820, and ICG	107

Figure 31. Organ images taken 24 hours after i.v. injection of IRPDcov, IR820,
or ICG.....109

Figure 32. Sample curve fit for plasma concentration data using the curvefit tool in
Matlab.....114

Figure 33. Pharmacokinetics of IRPDcov, IR820, and ICG plasma concentrations vs.
time after i.v. dose114

CHAPTER 1: INTRODUCTION, LITERATURE REVIEW, AND SPECIFIC AIMS

1.1. Background and Relevance

1.1.1. The field of theranostics

Advances in early cancer diagnosis and therapy have improved the survival statistics of individuals with cancer in the last few decades. Based on data collected 2001-2007, the 5-year relative survival rate in cancer patients is 67%, which is 18% higher than thirty years ago (ACS, 2012). The use of multifunctional modalities which possess diagnostic and therapeutic properties, referred to as theranostics, can further enhance cancer management by enabling a combined approach to detection and treatment (Xie et al., 2010). In many cases, early detection is the most important variable affecting the choice of therapeutic intervention and regimen. The timeline for detection of a tumor will impact the feasibility of surgical resection without the need for adjuvant treatment. In later stages of cancer, a combination of management approaches will be needed, which typically include surgery, radiation, and chemotherapy (Minev, 2011).

One of the main challenges in combining early diagnosis and therapy is that imaging and therapeutic probes are typically different in terms of selectivity and biodistribution (Kelkar et al., 2011). This complicates the process of monitoring responses to treatment, which in turn creates difficulties in planning, timing, and assessing the success of interventions. By combining both therapy and diagnostic capabilities into a single platform, theranostic agents provide clinicians with a multipurpose tool that can be used

to detect, image, treat, and monitor therapeutic response over time (Sumer et al., 2008). As a result, clinicians can implement therapy at an earlier stage, as well as achieve increased safety, sensitivity and efficacy in heterogeneously natured diseases such as cancer (Melancon et al., 2012; Sumer et al., 2008). The ability to monitor disease progression in a more effective manner can also reduce delays in implementing plan of care changes when therapy regimes need to be adjusted.

From the patient's point of view, quality of care may be enhanced as well. Theranostic management strategies could minimize the need for repeated medical procedures that may involve multiple office visits or hospital stays, increased risk of side effects, increased risk of dosage or medical errors, delayed therapeutic interventions, discomfort, and impact on their psychological well-being and quality of life.

1.1.2. Multifunctional agents used in theranostic applications: the advantages of nanomaterials

Multifunctional approaches may be crucial to the development of customizable early detection systems, tailored cancer therapies, real-time monitoring of treatment progression, and clinically translatable advances in cancer diagnosis, intervention and prognosis (Fernandez-Fernandez et al., 2011). Although the field of theranostics is still in its infancy in terms of development, there has been an explosion of research in this field in the past few years, in part related to parallel developments in nanotechnology. Many nanomaterials have built-in imaging capabilities, and can be modified to become multifunctional by combining them with a therapeutic agent via entrapment, conjugation,

or adsorption; or by exploiting their inherent therapeutic properties such as heat generation hyperthermia or singlet oxygen generation for photodynamic applications. Additionally, nanoparticles can circumvent some delivery challenges, such as those posed by multidrug resistance phenomena and in some cases by physiological barriers, such as the blood-brain barrier (Zamboni et al., 2012).

The fact that both diagnosis and therapy require sufficient accumulation in target tissues is another reason why nanoformulations provide a desirable platform for theranostic purposes (Bharali et al., 2010; Xie et al., 2010). Due to their small size, nanoparticles are less susceptible to reticuloendothelial system clearance than larger agents, and for sizes around 100 nm with near neutral charge, they have better *in vivo* penetration into tissues and cells (Brigger et al., 2002; Xu et al., 2006). The enhanced permeability and retention effect (EPR) also provides nanosize vehicles with the inherent advantage of passive targeting to tumor sites (Iyer et al., 2006; Maeda, 2010; Maeda et al., 2000). When tumor tissues are compared to healthy tissues, research has found several anatomical and physiological differences, including larger pore sizes and increased leakiness, shape irregularities, and reduced lymphatic clearance (Kelkar et al., 2011). The end result is that there is preferential accumulation of nanoformulations in tumors due to enhanced delivery and reduced clearance from tumor tissues, which may translate into increased treatment efficacy and reduced systemic toxicity (Maeda et al., 2009; Maeda et al., 2000), although this approach is limited by its lack of true specificity. Another characteristic of many tumors is active angiogenesis, which increases blood vessel availability in the tumor area (Maeda, 2010). It is also possible to artificially enhance the EPR effect by

increasing regional blood pressure, or through the use of nitric oxide donors in the case of hypoxic tumors. Both of these approaches have been demonstrated to be successful in humans in increasing drug accumulation at target sites via nanocarriers (Maeda, 2010). Still, more specific approaches to deliver these formulations would be desirable, given that cancer is by definition a heterogeneous problem.

To overcome the limitations of passive targeting, nanoformulations can be actively targeted by decoration or conjugation with moieties such as small ligands, antibodies, or biomarkers that can direct them towards specific molecular targets, resulting in increased selectivity and specificity of cellular uptake (Fernandez-Fernandez et al., 2011). Additionally, nanoformulations can be coated with different substances to provide specific desirable properties. An excellent example is coating of nanoparticles with polyethylene glycol (PEG), either via adsorption or covalent conjugation, to obtain stealth formulations and reduce biological elimination. PEG is a hydrophilic polymer that reduces non-specific interactions with proteins, which would lead to subsequent phagocytosis of the nanosystems by circulating immune system agents such as macrophages. The mechanism by which PEG exerts this function is primarily through steric repulsion as well as surface charge shielding effects, so that PEGylation results in long-circulating formulations (Bazile et al., 1995; Gref et al., 2000; Li et al., 2001; Moghimi et al., 2001; Peracchia et al., 1999; Scott et al., 1998). PEGylation also minimizes van der Waals attractions between particles, resulting in reduced aggregation behaviors that would lead to additional reticuloendothelial system recognition and elimination (Jokerst et al., 2011); and it also reduces metabolic degradation by enzymes

(Veronese et al., 2005). Covalent attachment of PEG chains does not affect chain properties in solution, so that formulations where PEG has been covalently attached will maintain their functionality (Alexis et al., 2008; Hrkach et al., 1997). PEGylation is considered a safe procedure for molecules destined for human use, with a therapeutic index of at least 600-fold between PEGylated products and PEG exposure levels that are toxic to humans (Webster et al., 2007).

1.1.3. Multifunctional agents used in theranostic applications: image-guided therapy

The imaging capability of a theranostic agent is often crucial for detection and monitoring purposes (Caldorera-Moore et al., 2011). Molecular imaging agents can be used as a diagnostic tool to visualize tissues and also to measure cellular processes related to disease. Nuclear imaging techniques such as PET and SPECT can provide valuable functional information, but have some disadvantages such as radiation exposure and complexity of the equipment (Janib et al., 2010). Optical imaging methods have high sensitivity, are inexpensive, and can be incorporated into fiber optic systems allowing for minimally invasive approaches; but they are limited by absorption and scattering, which result in low penetration (Alfano et al., 1997). This limitation can be alleviated by the use of near-infrared (NIR) imaging agents. At wavelengths between 700 and 900 nm, *in vivo* absorption and scattering processes are reduced due to decreased interaction with biological chromophores compared to shorter wavelengths of light (Simpson et al., 1998). This property results in improved tissue penetration for *in vivo* NIR optical imaging compared to optical imaging at shorter wavelengths (Bloch et al., 2005).

Nanoparticles have been used for applications involving MRI, CT, nuclear, and optical imaging (Kang, 2010; Lee et al., 2008), and multifunctional nanoparticle designs allow for simultaneous *in vivo* delivery of imaging and therapeutic agents (Kim et al., 2010). In some cases, the intrinsic properties of the nanoparticle allow it to be used as an imaging agent and/or an agent for hyperthermia, radiation, or photodynamic therapy applications. This provides opportunities for image-guided therapy and truly integrated theranostic systems (Fernandez-Fernandez et al., 2011).

For example, iron-oxide nanoparticles can be used as MRI probes and as hyperthermia agents, and can also be loaded with chemotherapy agents to serve as drug delivery carriers (Wust et al., 2006; Yu et al., 2008). Gold nanoformulations such as nanospheres, nanorods, nanoshells, and nanocages have been applied to optical imaging, CT imaging, photothermal therapy, drug delivery, and combined imaging and therapy (Huang et al., 2008; Huff et al., 2007; Oyelere et al., 2007; von Maltzahn et al., 2009). Silica-based formulations have also been applied for multifunctional purposes in combination with other agents. Benachour et al have recently reported the preparation of multifunctional silica-based nanoparticles with encapsulated chlorin for photodynamic therapy, and decorated with gadolinium to serve as an MRI contrast agent as well as with peptides for active targeting (Benachour et al., 2012). Some NIR dyes such as cyanine dyes, rhodamine-based formulations, phthalocyanine and naphthalocyanine can also be used as photothermal and imaging agents (Bandichhor et al., 2006; Hilderbrand et al., 2005; Patonay et al., 2004). Cyanine dyes have large molar extinction coefficients, mid-range fluorescence quantum yields, and a wide choice of tunable wavelengths (Hilderbrand et

al., 2005; Patonay et al., 2004; Zaheer et al., 2001), which makes them attractive for *in vivo* applications.

1.1.4. The cyanine dyes indocyanine green and IR820 and their applications in imaging and hyperthermia

An example of a cyanine NIR dye with multifunctional applications is indocyanine green (ICG), which has been utilized for many years in clinical measurement of cardiac output, evaluation of liver and kidney function, photodynamic therapy, photothermal therapy and imaging (Dorshow et al., 1998; Johansen, 1990), and has low toxicity. Upon excitation by light, ICG can release energy as emitted fluorescence photons, as well as through non-radiative internal conversion and heat emission. Although the heat generation efficiency of ICG is smaller than that of gold nanoparticles (Hirsch et al., 2003; O'Neal et al., 2004), ICG is able to rapidly elevate temperature upon laser excitation to therapeutic thermal ranges that can selectively kill cancer cells (Abels et al., 2000; Chen et al., 1996; Tang et al., 2009). Hyperthermia has been widely utilized as an adjuvant treatment for cancer (Luk et al., 1980; van der Zee, 2002), and is less prone to toxic side effects than other therapeutic approaches such as chemotherapy (Kelkar et al., 2011). Cell culture, animal and human studies have also shown that hyperthermia has a synergistic effect with other cancer therapeutic modalities (Fotopoulou et al., 2010; Tang et al., 2009; West et al., 1980; Wust et al., 2002).

The main challenge of using ICG *in vivo* is its poor stability in aqueous solution and fast degradation rates, as well as its very short plasma half-life in the order of 3 to 5 minutes

(Desmettre et al., 2000; Haller et al., 1993; Saxena et al., 2003). This limits the *in vivo* therapeutic window for hyperthermia, imaging, or a dual combination using ICG, especially in the case of the combinational approach, where timing of the diagnostic and the therapeutic components may be an issue. In order for a multifunctional approach to be effective and clinically translatable, the combined diagnostic and therapeutic windows have to be large enough to make both processes practically feasible. If the window of opportunity is very short, it becomes very difficult to use the diagnostic information to guide therapy, or to follow the effects of therapy during a subsequent monitoring period. Since the main mechanism of fluorescence degradation in ICG is the formation of weakly-fluorescing ICG aggregates via intermolecular interactions (Zhou et al., 1994), some groups have attempted to increase the stability of ICG using stabilizer additives such as the Poly-(α,β)-DL-aspartic acid sodium salt PASP (Maarek et al., 2001; Rajagopalan et al., 2000). However, the additive can complicate the incorporation of the dye into delivery vehicles such as nanoparticles, and its toxicity profile for *in vivo* use has not been adequately evaluated.

Nanoformulations of ICG, such as ICG-loaded PLGA nanoparticles or ICG-loaded mesocapsules have demonstrated increased plasma circulation times and organ uptake in mice (Saxena et al., 2006; Yaseen et al., 2009). Our group has shown that ICG entrapped in nanoparticles can still produce hyperthermic cell killing (Tang et al., 2010), and we have developed a multifunctional ICG-DOX-PLGA delivery system for image-guided chemotherapy and hyperthermia (Manchanda et al., 2010). When exploring the effect of the multifunctional system in cancer cell lines MES-SA, DX-5, and SKOV-3, we found

that this delivery vehicle was able to circumvent multidrug resistance (MDR) in resistant cells which expressed p-glycoprotein, and that the combination of hyperthermia and chemotherapy resulted in improved cell killing compared to chemotherapy or hyperthermia alone (Tang et al., 2010).

A possible alternative to the use of ICG, either in free dye form or as a nanoformulation, is to explore the potential of other NIR dyes with similar optical and thermal generation abilities but improved stability profiles. It would be desirable to have the ability to use NIR-responsive molecules for imaging and hyperthermia while eliminating or minimizing some of the problems that complicate ICG in *in vivo* applications (Fernandez-Fernandez et al., 2012). An example of a NIR dye with strong similarities to ICG is the commercially available dye IR820. The chemical structures of ICG and IR820 are very similar, with the main difference being the addition of a chlorinated cyclohexene as an intermediate ring in the structure of IR820 (Figure 1).



Figure 1. Molecular structures of indocyanine green (A) and IR820 (B). Note the structural similarity, except for the chlorinated cyclohexene ring structure in IR820 which is absent in ICG.

The presence of this ring is expected to confer additional rigidity and stability to the molecular structure compared to ICG, given that substituents within the polymethine

chain will limit bond rotation (Levitus et al., 2011). The structural modification could also possibly result in enhanced molecular stability by providing steric hindrance to intermolecular aggregation processes. An additional advantage of the presence of the chlorohexene is that it provides IR820 with more options for functional conjugation through the chlorine group, which can result in more amenability to the creation of multifunctional or targeted conjugates.

Several recent studies have applied IR820 dye or conjugates of the dye for *in vivo* applications. Prajapati et al. used IR820 as a blood pool contrast agent to image tissue injuries and tumors in mice, and estimated the dye clearance half-life to be similar to that of albumin, approximately 35 hours, based on *in vitro* binding studies to albumin (Prajapati et al., 2009). Pandey et al. conjugated IR820 with a photodynamic therapy drug and studied the resulting conjugate in mice with IR820 being used exclusively for its imaging role (Pandey et al., 2008). Masotti et al. conjugated IR820 with polyethylenimine (PEI) for DNA binding applications and *in vivo* imaging (Masotti et al., 2008). Thierry et al prepared poly(allylamine hydrochloride)-poly(acrylic acid) coated magnetic iron oxide and gold nanoparticles, which were loaded with cisplatin as well as with a conjugate of IR820 and PEI following the work done by Masotti and colleagues (Thierry et al., 2009).

None of these studies exploited the inherent ability of IR820 to be used as a dual imaging and hyperthermia agent, with all of them just focusing on its imaging properties. Prior to our group's work, there were also no previous reports of any efforts to perform a detailed

in vitro characterization of IR820 in terms of thermal generation and optical characteristics, or to study its toxicity in cellular systems, which should all have preceded any *in vivo* applications (Fernandez-Fernandez et al., 2012). Additionally, there are to our knowledge no reports of nanoconjugates of IR820 except for those resulting from this dissertation.

1.2. Statement of Purpose and Specific Aims

The overarching goal of this project was to develop and characterize novel nanoconjugates of IR820, and explore the potential of IR820 and its conjugates for theranostic applications in cancer. As a result of the studies which are part of this dissertation, our group was the first to characterize IR820 in terms of optical and thermal generation properties; to compare IR820 properties to those of ICG for cellular hyperthermia, cellular imaging, and *in vivo* imaging; and to formulate and characterize long-circulating nanoconjugates of IR820 and polyethylene glycol (PEG) for theranostic applications.

The following were the four objective-based specific aims:

1.2.1. Specific aim #1: IR820 in vitro characterization and theranostic applications

- a. Characterize the *in vitro* absorption and fluorescence behavior of IR820, and compare it with ICG.
- b. Characterize the degradation of IR820 in aqueous solution under different light and temperature conditions, and compare degradation kinetics with those of ICG.

- c. Compare *in vitro* cell imaging capabilities of IR820 with those of ICG.
- d. Compare the *in vitro* heat generation capability of IR820 after NIR laser exposure with that of ICG.
- e. Characterize the *in vitro* cytotoxicity of IR820 on cancer cell lines MES-SA, SKOV-3, and Dx5, and compare with ICG.
- f. Characterize the *in vitro* cytotoxicity of IR820 on cancer cell lines MES-SA, SKOV-3, and Dx5 after NIR laser exposure, and compare with ICG.

Specific aim #1 is addressed in Chapter 3.

1.2.2. *Specific aim #2: Formulation and characterization of ionic IR820 nanoconjugate*

- a. Prepare IR820-PEG-diamine nanoconjugate using ionic interactions (IR820-PDNCs)
- b. Characterize IR820-PDNCs in terms of physicochemical properties, dye content, absorption/fluorescence properties, and stability in solution.
- c. Compare *in vitro* cell imaging capabilities of IR820-PDNCs with those of IR820.
- d. Characterize the *in vitro* cytotoxicity of IR820-PDNCs on cancer cell lines MES-SA, SKOV-3, and Dx5, and compare with IR820.
- e. Characterize the *in vitro* cytotoxicity of IR820-PDNCs on cancer cell lines MES-SA, SKOV-3, and Dx5 after NIR laser exposure, and compare with IR820.

Specific aim #2 is addressed in Chapter 4.

1.2.3. *Specific aim #3: Formulation and characterization of covalent IR820 nanoconjugate*

- a. Prepare covalently-linked IR820-PEG-diamine nanoconjugate (IRPDcov)
- b. Characterize IRPDcov in terms of physicochemical properties, dye content, absorption/fluorescence properties, and stability.
- c. Compare *in vitro* cell imaging capabilities of IRPDcov with IR820.
- d. Characterize the *in vitro* cytotoxicity of IRPDcov on cancer cell lines MES-SA, SKOV-3, and Dx5, and compare with IR820.
- e. Characterize the *in vitro* cytotoxicity of IRPDcov on cancer cell lines MES-SA, SKOV-3, and Dx5 after NIR laser exposure, and compare with IR820 cytotoxicity.

Specific aim #3 is addressed in Chapter 5.

1.2.4. *Specific aim #4: Biodistribution studies of IRPDcov, IR820, and ICG*

- a. Establish feasibility of using IRPDcov for *in vivo* imaging.
- b. Compare and contrast the biodistribution of IRPDcov, IR820, and ICG in an *in vivo* model, using Matlab image analysis of fluorescent organ images 24 hours after i.v. injection.
- c. Compare and contrast biodistribution of IRPDcov, IR820, and ICG in an *in vivo* model, by determining 24-hour quantitative content from organ sampling.

- d. Calculate and compare IRPDcov, IR820, and ICG pharmacokinetic parameters, including plasma half-life, from blood sampling data collected at 4 different time points after i.v. injection.

Specific aim #4 is addressed in Chapter 6.

Chapter 1 References

- Abels, C., S. Fickweiler, et al. (2000). Indocyanine green (ICG) and laser irradiation induce photooxidation. *Arch Dermatol Res* **292**(8): 404-411.
- American Cancer Society. (2012). *Cancer Facts & Figures 2012*. Atlanta, GA.
- Alexis, F., E. Pridgen, et al. (2008). Factors affecting the clearance and biodistribution of polymeric nanoparticles. *Mol Pharm* **5**(4): 505-515.
- Alfano, R. R., S. G. Demos, et al. (1997). Advances in optical imaging of biomedical media. *Ann. N. Y. Acad. Sci.* **820**: 248-270.
- Bandichhor, R., A. D. Petrescu, et al. (2006). Synthesis of a new water-soluble rhodamine derivative and application to protein labeling and intracellular imaging. *Bioconjugate Chem.* **17**(5): 1219-1225.
- Bazile, D., C. Prud'homme, et al. (1995). Stealth Me.PEG-PLA nanoparticles avoid uptake by the mononuclear phagocytes system. *J Pharm Sci* **84**(4): 493-498.
- Benachour, H., S. A, et al. (2012). Multifunctional peptide-conjugated hybrid silica nanoparticles for photodynamic therapy and MRI. *Theranostics* **2**(9): 889-904.
- Bharali, D. J. and S. A. Mousa (2010). Emerging nanomedicines for early cancer detection and improved treatment: current perspective and future promise. *Pharmacol Ther* **128**(2): 324-335.
- Bloch, S., F. Lesage, et al. (2005). Whole-body fluorescence lifetime imaging of a tumor-targeted near-infrared molecular probe in mice. *J Biomed Opt* **10**(5): 054003.
- Brigger, I., C. Dubernet, et al. (2002). Nanoparticles in cancer therapy and diagnosis. *Adv. Drug Delivery Rev.* **54**(5): 631-651.
- Caldorera-Moore, M. E., W. B. Liechty, et al. (2011). Responsive theranostic systems: integration of diagnostic imaging agents and responsive controlled release drug delivery carriers. *Acc Chem Res* **44**(10): 1061-1070.
- Chen, W. R., R. L. Adams, et al. (1996). Photothermal effects on murine mammary tumors using indocyanine green and an 808-nm diode laser: an in vivo efficacy study. *Cancer Lett.* **98**(2): 169-173.
- Desmettre, T., J. M. Devoisselle, et al. (2000). Fluorescence properties and metabolic features of indocyanine green (ICG) as related to angiography. *Surv Ophthalmol* **45**(1): 15-27.

- Dorshow, R. B., J. E. Bugaj, et al. (1998). Noninvasive fluorescence detection of hepatic and renal function. *J Biomed Opt* **3**(3): 340-345.
- Fernandez-Fernandez, A., R. Manchanda, et al. (2012). Comparative study of the optical and heat generation properties of IR820 and indocyanine green. *Mol Imaging* **11**(2): 99-113.
- Fernandez-Fernandez, A., R. Manchanda, et al. (2011). Theranostic applications of nanomaterials in cancer: drug delivery, image-guided therapy, and multifunctional platforms. *Appl Biochem Biotechnol* **165**(7-8): 1628-1651.
- Fotopoulou, C., C. H. Cho, et al. (2010). Regional abdominal hyperthermia combined with systemic chemotherapy for the treatment of patients with ovarian cancer relapse: Results of a pilot study. *Int J Hyperthermia* **26**(2): 118-126.
- Gref, R., M. Luck, et al. (2000). 'Stealth' corona-core nanoparticles surface modified by polyethylene glycol (PEG): influences of the corona (PEG chain length and surface density) and of the core composition on phagocytic uptake and plasma protein adsorption. *Colloids Surf B Biointerfaces* **18**(3-4): 301-313.
- Haller, M., C. Akbulut, et al. (1993). Determination of plasma volume with indocyanine green in man. *Life Sci* **53**(21): 1597-1604.
- Hilderbrand, S. A., K. A. Kelly, et al. (2005). Monofunctional near-infrared fluorochromes for imaging applications. *Bioconjugate Chem.* **16**(5): 1275-1281.
- Hirsch, L. R., R. J. Stafford, et al. (2003). Nanoshell-mediated near-infrared thermal therapy of tumors under magnetic resonance guidance. *Proc Natl Acad Sci U S A* **100**(23): 13549-13554.
- Hrkach, J. S., M. T. Peracchia, et al. (1997). Nanotechnology for biomaterials engineering: structural characterization of amphiphilic polymeric nanoparticles by ¹H NMR spectroscopy. *Biomaterials* **18**(1): 27-30.
- Huang, X., P. K. Jain, et al. (2008). Plasmonic photothermal therapy (PPTT) using gold nanoparticles. *Lasers Med Sci* **23**(3): 217-228.
- Huff, T. B., M. N. Hansen, et al. (2007). Controlling the cellular uptake of gold nanorods. *Langmuir* **23**(4): 1596-1599.
- Iyer, A. K., G. Khaled, et al. (2006). Exploiting the enhanced permeability and retention effect for tumor targeting. *Drug Discov Today* **11**(17-18): 812-818.
- Janib, S. M., A. S. Moses, et al. (2010). Imaging and drug delivery using theranostic nanoparticles. *Adv Drug Deliv Rev* **62**(11): 1052-1063.

- Johansen, P. L. (1990). The dye dilution method for measurement of cardiac output. *Eur. Heart J.* **11**: Suppl I:6-12.
- Jokerst, J. V., T. Lobovkina, et al. (2011). Nanoparticle PEGylation for imaging and therapy. *Nanomedicine (Lond)* **6**(4): 715-728.
- Kang, K. W. (2010). Preliminary Pre-Clinical Results and Overview on PET/MRI/Fluorescent Molecular Imaging. *Open Nucl Med J* **2**: 153-156.
- Kelkar, S. S. and T. M. Reineke (2011). Theranostics: combining imaging and therapy. *Bioconjug Chem* **22**(10): 1879-1903.
- Kim, K., J. H. Kim, et al. (2010). Tumor-homing multifunctional nanoparticles for cancer theragnosis: Simultaneous diagnosis, drug delivery, and therapeutic monitoring. *Journal of Controlled Release* **146**(2): 219-227.
- Lee, H. Y., Z. Li, et al. (2008). PET/MRI dual-modality tumor imaging using arginine-glycine-aspartic (RGD) - Conjugated radiolabeled iron oxide nanoparticles. *J Nucl Med* **49**(8): 1371-1379.
- Levitus, M. and S. Ranjit (2011). Cyanine dyes in biophysical research: the photophysics of polymethine fluorescent dyes in biomolecular environments. *Q Rev Biophys* **44**(1): 123-151.
- Li, Y., Y. Pei, et al. (2001). PEGylated PLGA nanoparticles as protein carriers: synthesis, preparation and biodistribution in rats. *J Control Release* **71**(2): 203-211.
- Luk, K. H., R. M. Hulse, et al. (1980). Hyperthermia in cancer therapy. *West J Med* **132**(3): 179-185.
- Maarek, J. M., D. P. Holschneider, et al. (2001). Fluorescence of indocyanine green in blood: intensity dependence on concentration and stabilization with sodium polyaspartate. *J Photochem Photobiol B* **65**(2-3): 157-164.
- Maeda, H. (2010). Tumor-selective delivery of macromolecular drugs via the EPR effect: background and future prospects. *Bioconjug Chem* **21**(5): 797-802.
- Maeda, H., G. Y. Bharate, et al. (2009). Polymeric drugs for efficient tumor-targeted drug delivery based on EPR-effect. *Eur J Pharm Biopharm* **71**(3): 409-419.
- Maeda, H., J. Wu, et al. (2000). Tumor vascular permeability and the EPR effect in macromolecular therapeutics: a review. *J Control Release* **65**(1-2): 271-284.

- Manchanda, R., A. Fernandez-Fernandez, et al. (2010). Preparation and characterization of a polymeric (PLGA) nanoparticulate drug delivery system with simultaneous incorporation of chemotherapeutic and thermo-optical agents. *Colloids and Surfaces B: Biointerfaces* **75**(1): 260-267.
- Masotti, A., P. Vicennati, et al. (2008). A novel near-infrared indocyanine dye-polyethylenimine conjugate allows DNA delivery imaging in vivo. *Bioconjug Chem* **19**(5): 983-987.
- Melancon, M. P., R. J. Stafford, et al. (2012). Challenges to effective cancer nanotheranostics. *J Control Release*.
- Minev, B. R. (2011). *Cancer Management in Man: Chemotherapy, Biological Therapy, Hyperthermia and Supporting Measures*. New York, NY, Springer.
- Moghimi, S. M., A. C. Hunter, et al. (2001). Long-circulating and target-specific nanoparticles: theory to practice. *Pharmacol Rev* **53**(2): 283-318.
- O'Neal, D. P., L. R. Hirsch, et al. (2004). Photo-thermal tumor ablation in mice using near infrared-absorbing nanoparticles. *Cancer Lett* **209**(2): 171-176.
- Oyelere, A. K., P. C. Chen, et al. (2007). Peptide-conjugated gold nanorods for nuclear targeting. *Bioconjugate Chemistry* **18**(5): 1490-1497.
- Pandey, R. K., N. James, et al. (2008). Cyanine-based compounds for tumor imaging with and without photodynamic therapy. *Top Heterocycl Chem* **14**: 41-74.
- Patonay, G., J. Salon, et al. (2004). Noncovalent labeling of biomolecules with red and near-infrared dyes. *Molecules* **9**(3): 40-49.
- Peracchia, M. T., S. Harnisch, et al. (1999). Visualization of in vitro protein-rejecting properties of PEGylated stealth polycyanoacrylate nanoparticles. *Biomaterials* **20**(14): 1269-1275.
- Prajapati, S. I., C. O. Martinez, et al. (2009). Near-infrared imaging of injured tissue in living subjects using IR-820. *Mol Imaging* **8**(1): 45-54.
- Rajagopalan, R., P. Uetrecht, et al. (2000). Stabilization of the optical tracer agent indocyanine green using noncovalent interactions. *Photochem Photobiol* **71**(3): 347-350.
- Saxena, V., M. Sadoqi, et al. (2003). Degradation kinetics of indocyanine green in aqueous solution. *J Pharm Sci* **92**(10): 2090-2097.

- Saxena, V., M. Sadoqi, et al. (2006). Polymeric nanoparticulate delivery system for Indocyanine green: Biodistribution in healthy mice. *International Journal of Pharmaceutics* **308**(1-2): 200-204.
- Scott, M. D. and K. L. Murad (1998). Cellular camouflage: fooling the immune system with polymers. *Curr Pharm Des* **4**(6): 423-438.
- Simpson, C. R., M. Kohl, et al. (1998). Near-infrared optical properties of ex vivo human skin and subcutaneous tissues measured using the Monte Carlo inversion technique. *Phys Med Biol* **43**(9): 2465-2478.
- Sumer, B. and J. Gao (2008). Theranostic nanomedicine for cancer. *Nanomedicine (Lond)* **3**(2): 137-140.
- Tang, Y., T. Lei, et al. (2010). Simultaneous Delivery of Chemotherapeutic and Thermal-Optical Agents to Cancer Cells by a Polymeric (PLGA) Nanocarrier: An In Vitro Study. *Pharm Res* **27**(10): 2242-2253.
- Tang, Y. and A. J. McGoron (2009). Combined effects of laser-ICG photothermotherapy and doxorubicin chemotherapy on ovarian cancer cells. *J Photochem Photobiol B* **97**(3): 138-144.
- Thierry, B., F. Al-Ejeh, et al. (2009). Multifunctional core-shell magnetic cisplatin nanocarriers. *Chem Commun (Camb)*(47): 7348-7350.
- van der Zee, J. (2002). Heating the patient: a promising approach? *Ann Oncol* **13**(8): 1173-1184.
- Veronese, F. M. and G. Pasut (2005). PEGylation, successful approach to drug delivery. *Drug Discov Today* **10**(21): 1451-1458.
- von Maltzahn, G., A. Centrone, et al. (2009). SERS-Coded Gold Nanorods as a Multifunctional Platform for Densely Multiplexed Near-infrared Imaging and Photothermal Heating. *Advanced Materials* **21**(31): 3175-+.
- Webster, R., E. Didier, et al. (2007). PEGylated proteins: evaluation of their safety in the absence of definitive metabolism studies. *Drug Metab Dispos* **35**(1): 9-16.
- West, K. W., T. R. Weber, et al. (1980). Synergistic effect of hyperthermia, papaverine, and chemotherapy in murine neuroblastoma. *J Pediatr Surg* **15**(6): 913-917.
- Wust, P., U. Gneveckow, et al. (2006). Magnetic nanoparticles for interstitial thermotherapy - feasibility, tolerance and achieved temperatures. *Int J Hyperther* **22**(8): 673-685.

- Wust, P., B. Hildebrandt, et al. (2002). Hyperthermia in combined treatment of cancer. *Lancet Oncol* **3**(8): 487-497.
- Xie, J., S. Lee, et al. (2010). Nanoparticle-based theranostic agents. *Adv Drug Deliv Rev* **62**(11): 1064-1079.
- Xu, Z. P., Q. H. Zeng, et al. (2006). Inorganic nanoparticles as carriers for efficient cellular delivery. *Chem. Eng. Sci.* **61**(3): 1027-1040.
- Yaseen, M. A., J. Yu, et al. (2009). Biodistribution of encapsulated indocyanine green in healthy mice. *Mol Pharm* **6**(5): 1321-1332.
- Yu, M. K., Y. Y. Jeong, et al. (2008). Drug-loaded superparamagnetic iron oxide nanoparticles for combined cancer imaging and therapy in vivo. *Angew Chem Int Ed Engl* **47**(29): 5362-5365.
- Zaheer, A., R. E. Lenkinski, et al. (2001). In vivo near-infrared fluorescence imaging of osteoblastic activity. *Nat. Biotechnol.* **19**(12): 1148-1154.
- Zamboni, W. C., V. Torchilin, et al. (2012). Best practices in cancer nanotechnology: perspective from NCI nanotechnology alliance. *Clin Cancer Res* **18**(12): 3229-3241.
- Zhou, J. F., M. P. Chin, et al. (1994). Aggregation and degradation of indocyanine green. *Proc SPIE* **2128**: 495-505.

CHAPTER 2: METHODOLOGY

This chapter describes the materials, methods, and protocols used in the experiments for each of the specific aims. Some of the descriptions in this chapter have been previously published as part of two manuscripts (Fernandez-Fernandez et al., 2012; Manchanda et al., 2012). Permission has been obtained in writing from the journal editors to utilize content from these publications in the dissertation manuscript, and copies of the aforementioned permission emails are included in the appendices.

2.1. Materials and Methods for Specific Aim 1

2.1.1. Chemicals

ICG (MW 775, IR-125) was obtained from Fisher Scientific (Pittsburgh, PA). IR-820 (MW 849.47), methanol, formaldehyde, and dimethyl sulfoxide (DMSO) were purchased from Sigma (St. Louis, MO).

2.1.2. Absorbance studies

Dye solutions were prepared in deionized water or in methanol and samples were placed in 1.5 mL cuvettes. Samples were diluted down to the linear absorption range (< 3 A.U.), and absorption spectra from 200 to 900 nm were recorded using a CaryWinUV spectrophotometer (Varian/Agilent Technologies, Switzerland). Automatic blank correction was performed using the appropriate solvent (water or methanol). The instrument was allowed to warm up for 30 minutes before measurements, and operating conditions were kept constant for all experiments.

2.1.3. Fluorescent spectrum characterization

We prepared ICG and IR-820 solutions in deionized water at 20 $\mu\text{g}/\text{mL}$ concentration, and then performed serial dilutions to 0.078 $\mu\text{g}/\text{mL}$. The fluorescence spectrum of each sample was measured using a Fluorolog-3 spectrofluorometer (Jobin Yvon Horiba, Edison, NJ) in steady-state mode. The device was allowed to warm up for 30 minutes, and then calibrated following manufacturer specifications for both the xenon lamp source and the expected Raman spectrum of water. Samples were placed in 4.5-mL cuvettes and measured immediately after preparation. For ICG and IR820 samples, we measured emission after excitation at 785-nm, because this is the wavelength that is typically used in ICG imaging systems. For IR820, we performed an additional set of measurements in which we used the peak absorption wavelength for IR820 in water as the excitation wavelength. We recorded spectral emission readings up to 900 nm, in 1-nm intervals. Deionized water was used as a blank for background correction. The samples were handled under reduced lighting conditions at all times to avoid photobleaching.

2.1.4. Effects of temperature and light on stability in aqueous solution

In order to characterize the optical stability of ICG and IR-820 in aqueous solution, we prepared solutions of ICG and IR-820 as described in section 2.1.3., and selected a concentration in the linear range, specifically, 0.625 $\mu\text{g}/\text{mL}$. Each sample (ICG or IR820) was aliquoted into five borosilicate glass containers and each container was assigned to one of five groups: (1) room temperature with constant direct light, (2) room temperature covered with foil, (3) room temperature in the dark, (4) refrigerator, or (5) covered water

bath at 42°C. A sample from each container was taken and measured at twenty-four hour intervals, following the same calibration and measurement procedure. Measurements of fluorescent intensity at the peak emission were done in triplicate. The instrument operating conditions were kept constant throughout the four-day period.

Data analysis followed the procedure described by Saxena et al in their study of ICG degradation in aqueous solution (Saxena et al., 2003). Briefly, data were plotted as percent peak fluorescence remaining versus time in hours, and fit to a pseudo-first order kinetics model to obtain the observed degradation rate constant k_{obs} . From this, the corresponding degradation half-time was calculated as shown in Equation 1 below.

$$t_{1/2} = \frac{\ln(2)}{K_{obs}} \quad \text{Equation 1}$$

2.1.5. Stability in different solvents under constant light and temperature conditions

The stability of ICG and IR820 dissolved in DMSO or methanol over a period of four days was studied by selecting a concentration in the linear range, specifically, 0.312 µg/mL, and placing a sample of each solution (ICG or IR820) at the chosen concentration in a borosilicate glass container in the refrigerator at 4°C in the dark. Samples from each container were measured at twenty-four hour intervals, following the same measurement procedure detailed in section 2.1.4., but using methanol or DMSO as the calibration blank as appropriate. Measurements were done in triplicate. The instrument operating conditions were kept constant throughout the four-day period.

2.1.6. Heat Generation Properties

A NIR Laser Module source (RLDH808-1200-5, Roithner Laserthchnik GmbH, Vienna, Austria) emitting at 808 nm with an output power of 1.0 Watts was used for the heat generation studies. Details of the setup have been provided by Tang et al. (Tang et al., 2009). Briefly, the laser module was fixed to a clamp to direct NIR light from above. A heated stage insert (World Precision Instruments Inc, Sarasota, Florida) was placed on a mobile stage positioned directly below the laser, and used to keep a 96-well plate containing dye samples at a baseline temperature of 37°C. The laser, when operational, was enclosed in a box to prevent external emission of the NIR light and to avoid air circulation that would affect the temperature of the sample. The mobile stage (holding the heated insert) had an extension arm to the outside of the box. The arm was used to move the location of the well plates, thereby allowing individual wells to be exposed to the NIR energy in succession one at a time without opening the box. We prepared 2.5 µM, 5 µM, and 10 µM solutions of ICG and IR820. Each sample was added to three wells in a 96-well plate sitting on the heated stage insert, and excited with the 808-nm laser at a power of 1440 J/cm² for 180 seconds. Temperature inside the well was measured with a thermocouple for the duration of exposure, and the three well values for a given dye were averaged.

2.1.7. Cytotoxicity with and without hyperthermia

The cytotoxic effect of ICG or IR820 with and without laser treatment was studied in human ovarian carcinoma SKOV-3 cells, human uterine sarcoma MES-SA cells, and

resistant human uterine sarcoma MES-SA/Dx5 (Dx5) cells. MES-SA is a chemotherapy sensitive uterine sarcoma line, and Dx5 is its multidrug-resistant counterpart. Multi drug resistance (MDR) in Dx5 cells is conferred by expression of membrane drug efflux protein P-gp. The ovarian epithelial adenocarcinoma line SKOV-3 also shows MDR properties, but in this case due to an inherent p53 deletion gene mutation. Therefore, these cell lines may respond differently to targeted therapy and hyperthermia, and they provide good models for testing of cancer treatment modalities. The cell lines, along with McCoy's 5A medium and fetal bovine serum (FBS) were purchased from ATCC (Manassas, VA, USA). Dulbecco's Phosphate Buffered Saline (DPBS) and penicillin were purchased from Sigma Aldrich.

The cells were cultured as monolayers in McCoy's 5A medium supplemented with 10% fetal bovine serum (FBS) and 1% penicillin in a humidified atmosphere of 95% air and 5% CO₂ at 37°C. For continuous culturing, cells were grown in plastic tissue culture flasks, subcultured twice weekly, and used for experiments while in the exponential growth phase. In the cytotoxicity experiments, cells were seeded into two 96-well plates, labeled plate A and B, at 5,000–8,000 cells per well. The plates were incubated overnight to allow for cell attachment.

On day 0, 24 hours after initial cell seeding, the cells in plate A were fixed and a Sulphorhodamine B (SRB) assay was performed using a TECAN plate reader (TECAN Systems Inc, San Jose California) at a wavelength of 530 nm to determine control growth of untreated cells. The absorbance values of the wells containing the cells were

background subtracted (from wells containing medium only) and averaged to give T_0 , defined as the initial amount of cells on day 0. Thus, plate A establishes a reference for the number of cells at the same time the experimental treatment is introduced in plate B.

On day 0, at the same time plate A was fixed to provide the T_0 value, plate B was treated with IR820 or ICG (final concentration of 0-10 μM). A final concentration of 0 μM indicates that no dye was added to the wells. Next, the cells in plate B were incubated at 37°C for approximately 2 hours, after which half of the wells in plate B were subjected to laser treatment for three minutes. For each concentration of dye (0-10 μM), half of the wells received laser treatment. Thus, for the control cells where no dye was added, half of the cells were exposed to laser. This provides a laser, no-dye control group. Plate B was returned to a 37°C incubator for another 24 hours. On day 1 (i.e. 48 hours after initial cell seeding and 24 hours after laser treatment), the cell protein amount was measured by the SRB assay. Potential cross talk between wells was eliminated by not using adjacent wells for cells that were exposed to laser treatment, thus ensuring that applying laser treatment to one well would not cause a temperature increase in another well. The SRB absorbance values were background subtracted to give T (absorbance of the treated cells) and C (absorbance of control cells not exposed to laser or dye). All measurements were done in four wells per treatment.

The following formulae were used to calculate net cell growth:

$$\text{if } T \geq T_0, \text{ net cell growth} = (T - T_0) / (C - T_0); \quad \text{Equation 2}$$

$$\text{if } T < T_0 \text{ then net cell growth (or cell death)} = (T - T_0) / (T_0). \quad \text{Equation 3}$$

T_0 is determined from SRB measurements in plate A, and represents the number of cells at the time treatment was initiated. C is determined from SRB measurements in plate B for the wells that were not exposed to either laser or dye, and T is the absorbance of the treated wells (laser treatment, dye treatment, or both). Net growth was plotted against dye concentration to show the toxicity effects as previously described in the literature (Monks et al., 1991). Statistical analysis ($\alpha = 0.05$) was performed using one-way ANOVA to compare (1) treatment values with the control value and (2) laser treatment versus no treatment for the same concentration of dye (0-10 μM).

2.1.8. Cellular imaging

SKOV3, MES-SA, and Dx5 cell lines were purchased from ATCC and cultured following ATCC specifications with 10% FBS-supplemented McCoy's 5A medium in a 37°C humidified incubator at 5% CO₂ level. D-poly coverslips, formalin and 24-well tissue culture plates were purchased from Fisher Scientific (Pittsburgh, PA, USA). Cells were seeded at a density of 4×10^4 cells per well (SKOV-3) or 1×10^5 cells per well (MES-SA, Dx5) in a 24-well plate over Poly-D-Lysine pre-coated glass coverslips placed in each well, and incubated overnight to reach confluence. The medium was removed and replaced with 0.5 mL of 10 μM IR820 or ICG solution and incubated for 30 minutes at 37°C without light exposure.

After incubation, cells were washed 3X with DPBS and fixed with 4% formaldehyde for 15 minutes at 37°C, followed by 3X washing with DPBS. The coverslips were then removed and mounted on precleaned glass microslides with prolong antifade

reagent/mounting medium mixture. Then, the specimens were observed using a fluorescent microscope (Olympus IX81, Japan) with a 60x water immersion objective and images were recorded with a CCD camera. The same filter set ($\lambda_{\text{ex}} = 775\text{nm}$ and $\lambda_{\text{em}} = 845\text{nm}$) was used for imaging of both fluorescence dyes. The CCD camera settings and exposures times were the same for both dyes for a given cell line (1000 ms for SKOV-3 and 4000 ms for MES-SA and Dx5). Green pseudo-color was added using EZ-C1 software (Nikon, Melville, NY).

2.1.9. Rat model studies

An imaging system consisting of a Sanyo DL 7140-201S laser (80 mW, 785 nm) and a Retiga 1300 CCD camera was used. The entire setup was covered by BK5 blackout material. The power at the imaging plane ranged from 0.1-0.5 mW. An equimolar solution of ICG or IR820 was prepared based on a dose of 0.24 mg/kg of body weight (Rajagopalan, 2000) and an injection volume of 0.25 mL. Wistar rats (160-224 g, nine weeks old) were purchased from Harlan (Indianapolis, IN), kept under standard housing conditions and fed ad libitum. All protocols followed the regulations of the Institutional Animal Care and Use Committee. Rats were randomly assigned to groups. On the day of the experiment, the animals were first anesthetized by inhalation of isoflurane in a closed chamber, and then injected intraperitoneally with a 40 mg/kg dose of pentobarbital. The chest and abdomen were shaved, and the animal was placed in supine facing the imaging setup. An image of the rat was obtained under white light illumination to determine the position of the target and to focus the camera before dye injection. Then, the laser was

turned on and another image was taken prior to dye injection to establish background. Laser current was set to 60 mA.

After the white and background images were obtained, ICG or IR820 dye was injected through the tail vein using a 3-way stopcock system connected to two syringes, one containing the dye and another one containing saline solution to flush the tail vein after injection. The camera started recording immediately before the injection, and 10-second exposure images of the abdomen were recorded in series using QCapture Pro software for at least 40 minutes or until the rat regained consciousness. An image focused on the chest was also taken before removing the animal from the setup on the day of the injection. Twenty four hours later, the rat was imaged again (abdomen and chest) using the same imaging setup under the same operating conditions. The protocol was completed in 6 rats, three per dye. Additionally, organs were carefully dissected and extracted after the 24-hour imaging protocol was completed in the intact animal. The lungs, kidneys and liver were then placed in black-coated Petri dishes and imaged using the same imaging setup.

Images were processed in Matlab to select a background-subtracted region of interest and calculate the normalized intensity, R , as the ratio of total pixel intensity (pixel index) in the region of interest to the area of the signal in μm^2 . Statistical analysis was performed to compare average ratios for each dye (t-test, 95% confidence level)

Quantitative measurements were performed by dye extraction in DMSO following the procedure detailed by Saxena et al for ICG (Saxena et al., 2006). Briefly, the organs were

homogenized and then incubated for four hours in DMSO. After four hours, the samples were centrifuged at 4,500 rpm for 5 minutes, the supernatant was collected, and sample emission was measured in a spectrofluorometer after 785 nm excitation. Dye mass in μg obtained from this measurement was normalized to homogenized organ mass in grams, and statistical analysis was performed to determine significant differences in dye content (t-test at 95% confidence level). Dye mass was determined from a standard calibration curve.

2.2. Materials and Methods for Specific Aim 2

2.2.1. Chemicals

PEG-diamine (6 kDa), IR820, methanol, dimethylsulfoxide (DMSO > 99.9% reagent grade) were purchased from Sigma-Aldrich (St. Louis, MO, USA).

2.2.2. Nanoconjugate preparation

To an aqueous solution of PEG-diamine (MW 6 kDa, 30 mg/5 ml), a solution of IR820 (8.4 mg/5 ml) dissolved in deionized water was added drop-wise over a period of 45 minutes through a 5-ml syringe with continuous stirring. The molar ratio was 1:2 PEG-diamine:IR820 based on available functional groups (two amines in PEG-diamine and one sulfonate in IR820). The reaction mixture was allowed to stir at room temperature for 3 hours. The ionic complex between PEG-diamine and IR820 was achieved by electrostatic interactions between the negatively charged sulphate groups of IR820 and the positively charged amine groups of PEG-diamine (Figure 2). The solution was centrifuged at 25,000 rpm for 30 minutes, the supernatant was discarded, and the

nanoconjugates thus formed were washed 3x with deionized water (5 ml). The resulting material was freeze-dried using the Freezezone system (Labconco, Free Zone Plus 6) for 24 hours.

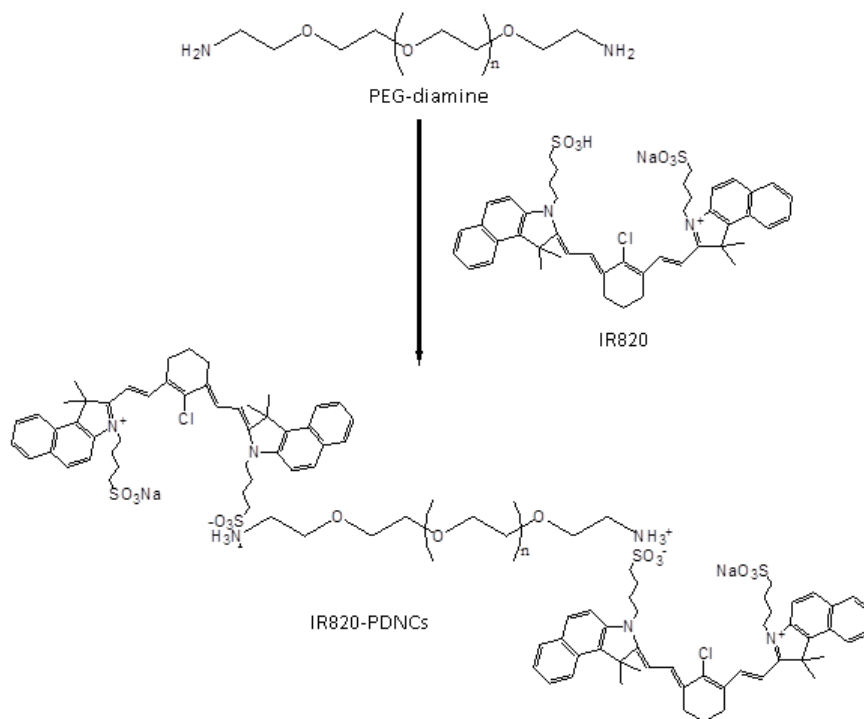


Figure 2. Reaction scheme and formulation of ionic IR820-PEG-diamine nanoconjugate (IR820-PDNCs).

2.2.3. Nanoconjugate characterization

Scanning electron microscopy (SEM) was used to verify size and uniformity of nanoplex shape and size. Freeze-dried IR820-PDNCs were resuspended in distilled water and were later dropped onto a silicon grid and dried under room temperature. The suspension was vacuum-coated with gold for 3 minutes. The surface morphology of the samples was observed under a scanning electron microscope (JEOL–JEM) operated at 15-keV pulse at different resolutions.

Nanoconjugate zeta potential was measured using a Zetasizer, Nano ZS (Malvern Instruments, UK) employing a nominal 5-mW He–Ne laser operating at 633 nm wavelength. The scattered light was detected at a 135° angle. The refractive index (1.33) and the viscosity (0.89) of ultrapure water at 25°C were used for measurements.

The FTIR spectra of dried material was recorded using the Perkin–Elmer®Spectrum™ 1000 FT-IR spectrometer (Perkin Elmer Inc., San Jose, CA), equipped with a Universal ATR (attenuated total reflectance) sampling device containing diamond crystal. Spectra were acquired and then processed with the Spectrum software. The spectra were scanned at room temperature over the wave number range of 4000–400 cm⁻¹, with a scan speed of 0.2cm/s and accumulations at a resolution of 4 cm⁻¹. Triplicates of each sample were averaged to obtain an average spectrum. A background spectrum of air was scanned under the same instrumental conditions before each series of measurements.

2.2.4. Dye content determination

The IR820 content in the freeze-dried nanoconjugates was determined by dissolving a known amount of sample in DMSO, sonicating to ensure complete dissolution, and performing serial dilutions in the fluorescence linear range. Sample fluorescence was measured at peak emission after 785-nm excitation with a Fluorolog-3 spectrofluorometer (Jobin Yvon Horiba, Edison, NJ, USA) under constant operating conditions. The amount of IR820 in the samples was determined from a calibration curve of free IR820 in DMSO after 785-nm excitation using blank subtraction.

2.2.5. Characterization of absorption properties

We prepared samples of IR820, PEG-diamine, and IR820-PDNCs in deionized water at 100 µg/mL concentration, and performed serial dilutions in the linear range. The concentration of IR820-PDNCs was normalized to dye content, and the concentration of PEG-diamine was also normalized based on the corresponding proportion of IR820 and PEG-diamine used in the formulation process. Sample absorption from 200 to 900 nm was measured with a Cary UV spectrophotometer (Varian/Agilent Technologies, Switzerland).

2.2.6. Characterization of fluorescence properties

We prepared samples of IR820 and IR820-PDNCs in PBS buffer at 100 µg/mL concentration, and performed serial dilutions in the linear range. Fluorescence emission from the samples was measured in 1-nm intervals after 690 nm-excitation, 785-nm excitation, and 844-nm excitation. Samples were measured using a Fluorolog-3 spectrofluorometer (Jobin Yvon Horiba, Edison, NJ, USA). Fluorescent curves were blank-subtracted and plotted versus emission wavelength.

2.2.7. Fluorescence stability studies

We prepared samples of IR820 and IR820-PDNCs in PBS buffer at concentrations in the linear range, and measured their baseline fluorescence emission profile after 785 nm excitation. Sample emission fluorescence was measured from 795 nm up to 850 nm, at 1-nm intervals. The samples were measured in 4-mL cuvettes using a Fluorolog-3

spectrofluorometer (Jobin Yvon Horiba, Edison, NJ, USA). Different aliquots from the same sample batch were kept in the refrigerator and measured following the same procedures 4 hours after preparation. The emission peak value was used to determine changes from baseline and the percent remaining fluorescence intensity was calculated. Statistical significance was determined by comparing percent remaining intensities using a t-test with $\alpha = 0.05$.

2.2.8. *Cytotoxicity with and without hyperthermia*

The cytotoxicity of four different treatments (IR820, IR820-PDNCs, IR820 plus laser, and IR820-PDNCs plus laser) in cancer cell lines was studied using the SRB colorimetric assay. Three different types of cancer cell lines (MES-SA, Dx5 and SKOV-3) were used for cytotoxicity assessment. Cells were seeded onto 96-well plates at an approximate density of 2×10^4 cells/well, and incubated overnight for attachment to the well, followed by treatment with free IR820 or IR820-PDNCs. The SRB assay was performed 24 hours post treatment to determine net cell growth. Tested IR820 concentrations ranged from 0 to 5 μM , where IR820 concentration equal to zero means that only DPBS and no drug was added to the wells (control group). Tested IR820-PDNCs concentrations were normalized to IR820 content in the particles so that the treatments were equivalent to tested concentrations of free dye.

In order to test the effect of hyperthermia, some of the cells were incubated for one hour with one of the following treatments: (1) 5 μM IR820, (2) IR820-PDNCs at concentrations equivalent to 5 μM of IR-820, (3) 2.5 μM PEG-diamine (based on the

molar ratio 1 PEG-diamine: 2 IR820 in the nanoplex formulation), or (4) only cell medium. These cells were then exposed to NIR laser illumination for 3 minutes, and the SRB assay was performed 24 hours post laser treatment. Temperature was measured with a thermocouple, and experimental wells were separated from each other by at least one empty well in all directions to avoid cross-effects. Data processing and analysis were as described in section 2.1.7., with net growth values generated by normalizing the data from each treatment to the growth of the control cells which were not exposed to IR820, IR820-PDNCs, or laser. Statistical significance was identified by one-way ANOVA for the difference among groups at the same treatment concentration, and between each group and the control group. A p-value <0.05 was considered to be statistically significant.

2.2.9. Cellular imaging

Lysine-coated coverslips were placed in each well of a 24-well plate. MES-SA, Dx5, and SKOV-3 cells were seeded on the coverslip at a density of 1×10^5 cells, 1×10^5 cells and 5×10^4 cells per well respectively in McCoy's 5A medium supplemented with 10% fetal bovine serum (FBS) and 1% penicillin, and were grown overnight for attachment. On the next day, the cell medium was removed and replaced with 5 μ M IR820 or equivalent free dye content of IR820-PDNCs. Cells were incubated in the dark at 37° C for 2.5 hours and then washed 3X with Dulbecco's phosphate buffered saline (DPBS). Then the cells were fixed with 4% formaldehyde for 15 minutes at 37°C, followed by 3X washing with DPBS. The coverslips were then removed and mounted on glass microslides with antifade reagent/mounting medium mixture. The cells were then examined by

fluorescence microscopy (Olympus IX81, Japan) with a 60X water-merged objective. The fluorescence was imaged at λ_{ex} (775 nm), λ_{em} (845 nm) with an exposure time of 4000 ms, which is well below the 20,000 ms threshold for autofluorescence. A CCD camera was used to capture the signals and the images were software-merged with pseudo color. The fluorescence microscope settings were kept the same throughout the experiment. Images were processed in Matlab to select a background-subtracted region of interest and to calculate the normalized intensity, R, as the ratio of total pixel intensity (pixel index) to signal area.

2.3. Materials and Methods for Specific Aim 3

2.3.1. Chemicals

PEG-diamine (6 kDa), IR820, methanol, dimethylsulfoxide (DMSO > 99.9% reagent grade), and triethylamine (TEA) were purchased from Sigma-Aldrich (St. Louis, MO, USA).

2.3.2. Nanoconjugate preparation

A mixture of PEG-diamine (MW 6 kDa, 30 mg/5 ml) and IR820 (9.4 mg/5 ml) in methanol was refluxed for 4 hours in the presence of triethylamine (2 eq.). The molar ratio was 1:2 PEG-diamine:IR820 based on available functional groups (two amines in PEG-diamine and one chloro group in IR820). The reaction scheme is illustrated in Figure 3, and involves covalent attachment of the amine group in PEG-diamine to the cyclohexene in IR820 at the chloro-substituted position via nucleophilic substitution, with displacement of the chlorine atom and production of triethylamine hydrochloride.

After the reaction progressed to completion, the sample was concentrated and the residue was dissolved in 5 ml of water, followed by dialysis against water using a MWCO 3.5 kDa for 24 hours. The nanoconjugates were freeze-dried using the Freezone system (Labconco, Free Zone Plus 6) for 24 hours, and stored in powder form at 4°C for further use. The reaction scheme was developed in consultation with Dr. Pradeep Kumar, from the Institute of Genomics and Integrative Biology in India.

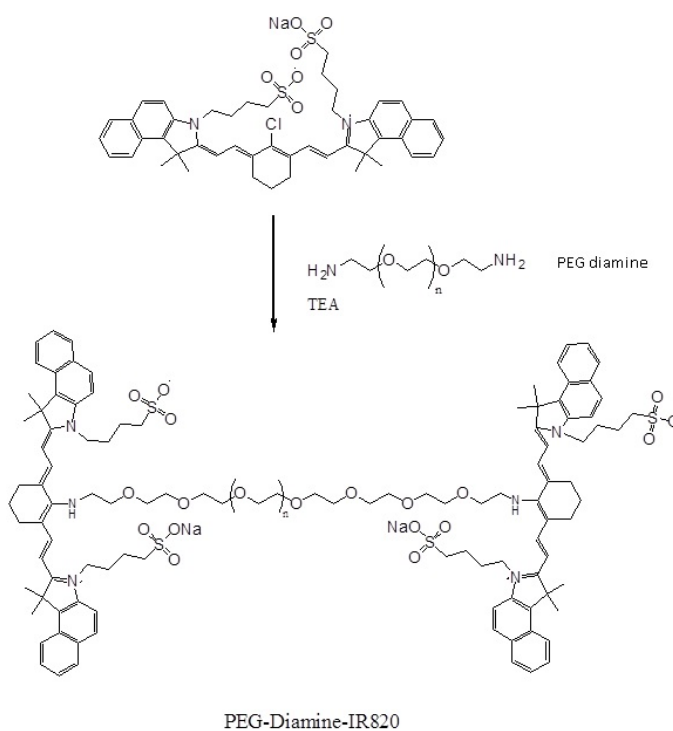


Figure 3. Reaction scheme and formulation of covalent IR820-PEG-diamine nanoconjugate (IRPDcov).

2.3.3. Nanoconjugate characterization

SEM pictures and zeta-potential measurements were obtained as described in section 2.2.3. H-NMR measurements were performed with the assistance of Tereza Vokata,

graduate student at the FIU Chemistry Department. For ¹H-NMR measurements, samples of IR820, PEG-diamine, and IRPDcov were dissolved in deuterated methanol. The ¹H NMR spectra were recorded on a 400 MHz Avance Bruker NMR spectrometer using 240 scans. Acquired data was processed and analyzed using MestReNova software. Chemical shifts were reported in parts per million (ppm) for ¹H NMR on δ scale based on the MeOD solvent peak ($\delta = 3.31$ ppm) as an internal standard.

2.3.4. Dye content determination

The IR820 content in the freeze-dried nanoconjugates was determined by dissolving a known amount of sample in DMSO, and following the procedures in section 2.2.4.

2.3.5. Fluorescence stability studies

We prepared samples of IR820 and IRPDcov in PBS buffer at concentrations in the linear range, and measured their baseline fluorescence emission profile after 785 nm excitation. The same procedures were followed as those described in section 2.2.5., except that fluorescence measurements were taken for up to 72 hours after sample preparation.

2.3.6. Cytotoxicity with and without hyperthermia

The cytotoxicity of four different treatments (IR820, IRPDcov, IR820 plus laser, and IRPDcov plus laser) was studied in cancer cell lines MES-SA, Dx5 and SKOV-3. The procedures followed were as described in section 2.2.8., with the use of IRPDcov in lieu of IR820-PDNCs.

2.3.7. Cellular imaging

MES-SA, Dx5 and SKOV-3 cells were imaged after 4-hour exposure to either 5 μ M IR820 or equivalent free dye content of IR820PDcov, following the same procedures described in section 2.2.9.

2.4. Materials and Methods for Specific Aim 4

The methods used in the fulfillment of specific aim 4 are described and discussed in complete detail in chapter 6. Briefly, thirty-six healthy ND4 Swiss-Webster outbred mice, weighing between 25 and 30 grams, were purchased from Harlan (Indianapolis, IN), housed at the FIU Animal Care Facility under a 12-hour light/dark cycle and fed *ad libitum*. Mice were randomly assigned to one of twelve groups (n=3) based on optical agent (ICG, IR820, or IRPDcov), and time point of data collection after injection (15 minutes, 30 minutes, 60 minutes, and 24 hours).

For time groups in the range of minutes, mice were anesthetized with i.p. pentobarbital (100 mg/kg), shaved, placed supine on the imaging setup described in section 2.1.9., injected through the tail vein with their assigned agent, and imaged. At the predetermined time point, a blood sample was obtained under anesthesia by heart puncture into the ventricle, and the animal was then euthanized by removal of the heart.

For mice in the 24-hour groups, each animal was anesthetized with 40 mg/kg of i.p. pentobarbital, injected with the assigned agent, and imaged. These mice were then

returned to their cage alive until the 24 hour time point. After 24 hours, they were anesthetized with pentobarbital (100 mg/kg) and imaged again under the same operating conditions. After imaging, a blood sample was obtained by heart puncture, and organs were carefully harvested for imaging and subsequent homogenization and dye extraction. Organ and plasma dye content were calculated from spectrofluorometric measurements of the samples using a previously created calibration curve of IR820 or ICG in DMSO at 785 nm excitation. Specific pharmacokinetic analysis of plasma data and the choice of models for data fitting are both discussed in depth in chapter 6.

Chapter 2 References

- Fernandez-Fernandez, A., R. Manchanda, et al. (2012). Comparative study of the optical and heat generation properties of IR820 and indocyanine green. *Mol Imaging* **11**(2): 99-113.
- Manchanda, R., A. Fernandez-Fernandez, et al. (2012). Nanoplexes for cell imaging and hyperthermia: in vitro studies. *J Biomed Nanotechnol* **8**(4): 686-694.
- Monks, A., D. Scudiero, et al. (1991). Feasibility of a high-flux anticancer drug screen using a diverse panel of cultured human tumor cell lines. *J Natl Cancer Inst* **83**(11): 757-766.
- Rajagopalan, R., P. Uetrecht, et al. (2000). Stabilization of the optical tracer agent indocyanine green using noncovalent interactions. *Photochem Photobiol* **71**(3): 347-350.
- Saxena, V., M. Sadoqi, et al. (2003). Degradation kinetics of indocyanine green in aqueous solution. *J Pharm Sci* **92**(10): 2090-2097.
- Saxena, V., M. Sadoqi, et al. (2006). Polymeric nanoparticulate delivery system for Indocyanine green: biodistribution in healthy mice. *Int J Pharm* **308**(1-2): 200-204.
- Tang, Y. and A. J. McGoron (2009). Combined effects of laser-ICG photothermotherapy and doxorubicin chemotherapy on ovarian cancer cells. *J Photochem Photobiol B* **97**(3): 138-144.

CHAPTER 3: IR820 CHARACTERIZATION AND THERANOSTIC APPLICATIONS

The purpose of specific aim #1 was to determine the feasibility of using IR820 as a substitute for ICG in imaging and photothermotherapy applications, and to perform a general characterization of IR820 that can serve as a foundation for these applications. We performed an *in vitro* comparison of the two dyes with respect to their optical properties, thermal generation properties, stability profiles, and toxicity effects on cellular systems. Additionally, we directly compared *in vivo* imaging characteristics of ICG and IR820 in a rat model. This work has been published as a full journal article (Fernandez-Fernandez et al., 2012). Permission has been obtained in writing from the journal editors to utilize content from this publication in the dissertation manuscript, and a copy of the aforementioned permission email is included in the appendices.

Materials and methods for this specific aim were discussed in chapter 2.

3.1. Physicochemical Characterization

3.1.1. Absorbance studies

Figure 4 shows the absorbance curves of IR820 and ICG in deionized water and methanol. In methanol, absorption peaks are located at 820 nm for IR820 and 779 nm for ICG. In water, the IR820 peak shifts to 691 nm, whereas peak absorption for ICG occurs at 784 nm. The observed hypsochromic shift in IR820 peak absorption in water versus methanol has been reported to exist in some heptamethine cyanine dyes, possibly as a

result of intramolecular charge transfer (ICT) or excited-state proton transfer (Peng et al., 2005). Considering this property, we expect that the absorption peak for *in vivo* applications is likely to be located close to the 691 nm peak observed in water, and the higher wavelength methanol peak would only be relevant for *in vitro* applications in non-physiological solvents.

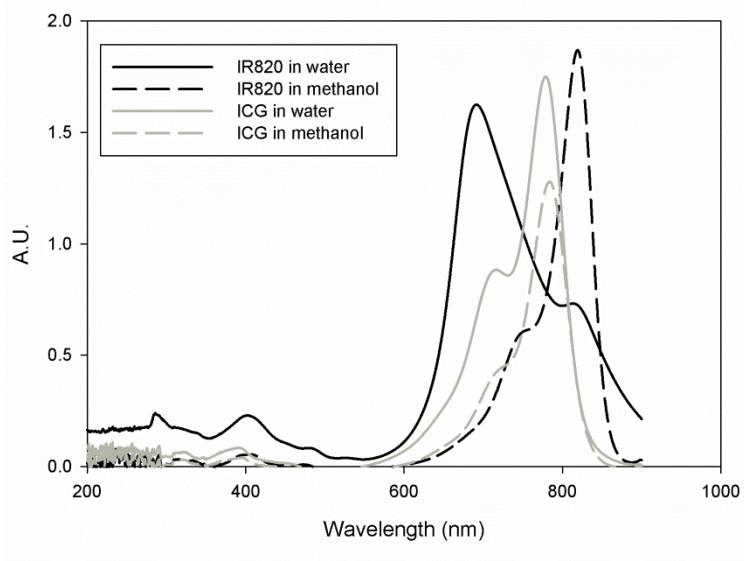


Figure 4. Absorbance spectra of IR820 and ICG in deionized water (solid) and methanol (dashed).

3.1.2. Fluorescent spectrum characterization

Figure 5 shows curves of fluorescence emission intensity versus wavelength for different ICG (5A) and IR820 (5B) concentrations in deionized water after excitation at 785 nm. Both dyes showed quenching for concentrations greater than 1.25 $\mu\text{g/mL}$, with similar linear ranges for both IR820 and ICG. This value is consistent with Saxena's reports of linearity for ICG aqueous solutions at concentrations below 2 $\mu\text{g/mL}$ (Saxena et al., 2003). Our results also show that, for a given concentration, IR820 has approximately ten times lower fluorescent yield than ICG after excitation at 785 nm.

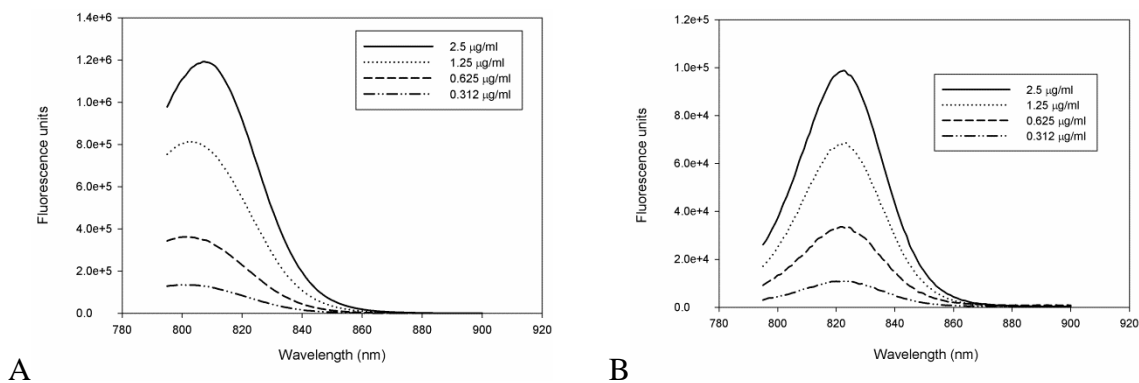


Figure 5. Fluorescence spectra after 785-nm excitation of aqueous solutions of (A) ICG and (B) IR820.

Table 1 shows peak emission location for different concentrations of ICG and IR820. For ICG, the peak emission wavelength is dependent on concentration, and more concentrated samples show emission shifts toward longer wavelengths. In the case of IR820, peak location was not as dependent on concentration and remained between 822 and 823 nm.

Concentration ($\mu\text{g/mL}$)	Emission Peak Location in nm, intensity	
	IR820	ICG
2.5	823 nm, 9.86E4	807 nm, 1.19E6
1.25	823 nm, 6.87E4	802 nm, 8.12E5
0.625	822, 3.36E4	802 nm, 3.62E5
0.3125	822, 1.09E4	800 nm, 1.35E5

Table 1. Emission Peak Location for Aqueous Solutions of ICG and IR820.

Besides comparing the fluorescent behavior of IR820 and ICG after 785-nm excitation, we also studied the fluorescence properties of IR820 upon excitation at its 691-nm peak absorption in water. The profiles are shown in Figure 6 and are similar to those obtained for IR820 aqueous solutions after excitation at 785 nm. Again, quenching occurs above 1.25 $\mu\text{g/mL}$, and peak emission is located at 822-823 nm. A slight increase in fluorescence emission of approximately 13-16% was observed for the emission spectrum after 691-nm excitation when compared with excitation at 785 nm.

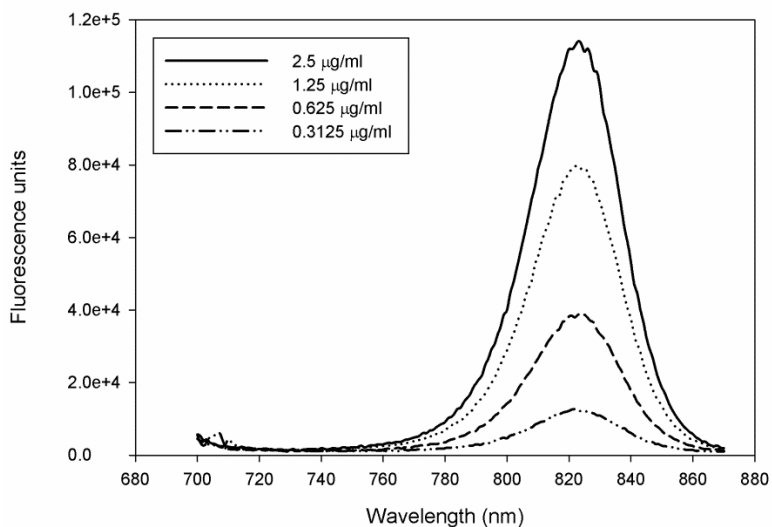


Figure 6. Fluorescence spectra after 691-nm excitation of aqueous solutions of IR820.

The fluorescent emission profiles of IR820 show lower fluorescence intensities than ICG for equivalent concentrations. This was observed after 785-nm excitation as well as after 691-nm excitation (at the optimal absorption peak of IR820 in water). The lower quantum yield after 785-nm excitation is expected based on the almost 100-nm difference with the absorption peak of IR820 in water. After 691-nm excitation, peak fluorescence intensities are higher than those observed after 785-nm excitation, but still lower than those of ICG.

Therefore, there must be a structural factor that contributes to this behavior. Most likely, the observed phenomenon is related to the intrinsic low quantum yield of the chlorohexene ring (Shimoda et al., 1979), as well as to the internal heavy atom effect by which a chlorine atom within the structure typically results in decreased quantum yields and fluorescent lifetimes (Mac et al., 2003).

An advantage of IR820 fluorescence emission is that peak location for fluorescent emission has little dependence on concentration, in contrast with ICG where we observe more variability and a shift towards lower wavelengths with decreasing concentration. The predictability of peak location for IR820 could facilitate the design of imaging systems targeting IR820 emission wavelengths and diminish some of the challenges that may arise with concentration-dependent peaks in ICG.

3.1.3. Effects of temperature and light on stability in aqueous solution

Aqueous solutions of IR820 and ICG were exposed to different temperatures (4°C, room temperature, and 42°C) and light conditions (dark room, covered with foil, or direct exposure to light). The degradation profiles of IR820 and ICG solutions, as shown in Figure 7 (different temperatures) and Figure 8 (different light levels), follow pseudo-first order kinetics with exponential decay. Covering the samples with foil was comparable, in terms of delaying degradation, to keeping them in a dark room. As expected based on the presence of the mesochlorohexene ring that confers rigidity to the molecule, IR820 demonstrated higher stability than ICG in aqueous solution under all temperature and light conditions, with degradation half-times approximately double those of ICG for a

given experimental condition. This is illustrated in Table 2. The degradation half-times for ICG in this study were consistent with those reported by other groups for this dye (Saxena et al., 2003). Direct light exposure and high temperatures resulted in fast degradation for both dyes and loss of smooth spectral features by day 4.

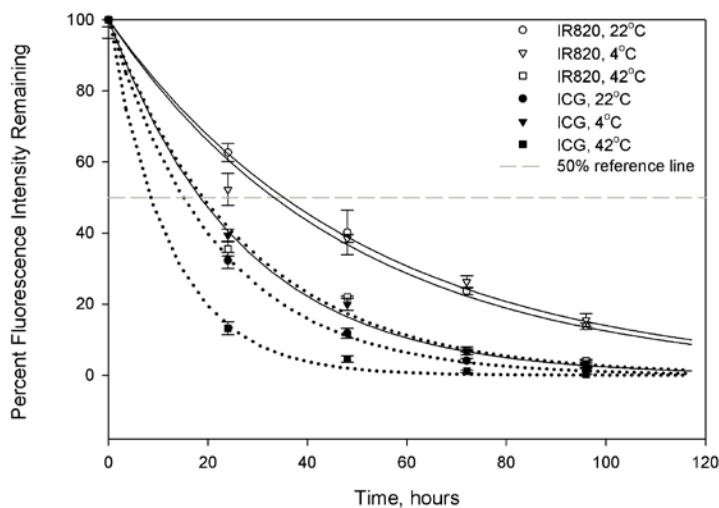


Figure 7. Effect of temperature on degradation of aqueous solutions of IR820 and ICG. Solid lines correspond to IR820 and dotted lines correspond to ICG. Error bars are \pm SD.

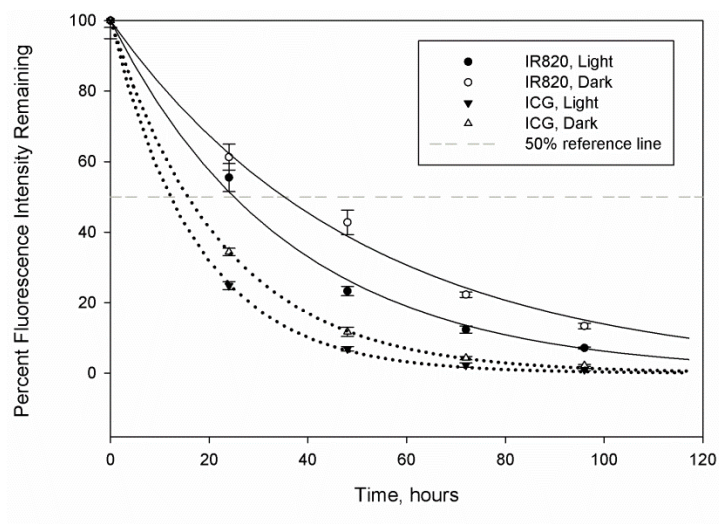


Figure 8. Effect of light on degradation of aqueous solutions of IR820 and ICG. Solid lines correspond to IR820 and dotted lines correspond to ICG. Error bars are \pm SD.

Experimental conditions	IR820			ICG		
	k_{obs} (hour ⁻¹)	$t_{1/2}$ (hours)	R^2	k_{obs} (hour ⁻¹)	$t_{1/2}$ (hours)	R^2
Light, 22°C	0.028	24.75	0.994	0.051	13.59	0.987
Dark, 22°C	0.020	34.65	0.992	0.042	16.50	0.992
Dark, 4°C	0.019	36.47	0.981	0.036	19.25	0.995
Dark, 42°C	0.035	19.80	0.984	0.064	10.83	0.989

Table 2. Stability characterization of aqueous solutions of IR820 and ICG following a pseudo-first order kinetics model.

Our results showing that IR820 is more stable in aqueous solution than ICG are consistent with other literature reports that describe structure-function relationships for fluorescent cyanine dyes (Lee et al., 2008). Lee's group reported that increased rigidity of the molecular structure of a dye results in enhanced stabilization of the molecule. Interestingly, temperature seemed to not be as important as light exposure in determining the degradation behavior of IR820 solutions. We did not observe any enhancement in stability when IR820 solutions were kept at 4°C in the dark versus when samples were stored at room temperature in the dark; however, there was a difference between the two conditions for ICG. Therefore, light exposure seems to be the most important influencing factor in degradation mechanisms of IR820, rather than temperature, unless temperatures are as extreme as those of a water bath (42°C). At such elevated temperatures, heat collisions increase significantly and the molecules tend to aggregate closer together, leading to increased degradation of the fluorescence properties.

3.1.4. Stability in different solvents under constant light and temperature conditions

ICG and IR820 were both stable in DMSO and methanol over a period of 4 days, with no significant decrease in fluorescence intensity when comparing samples measured on day 1 versus samples measured on day 4 ($p > 0.05$, paired t-test). Thus, both dyes showed excellent stability in methanol and DMSO.

3.1.5. Hyperthermia properties

Figure 9 illustrates changes in temperature during 180 seconds of 808-nm laser exposure for IR820 (Figure 9A) and ICG (Figure 9B), with a starting temperature of 37°C. For equivalent concentrations, the peak temperature increase for IR820 was significantly smaller than the increase observed in ICG (4-9% difference in peak temperature, $p < 0.05$ for comparisons between equivalent dye concentrations).

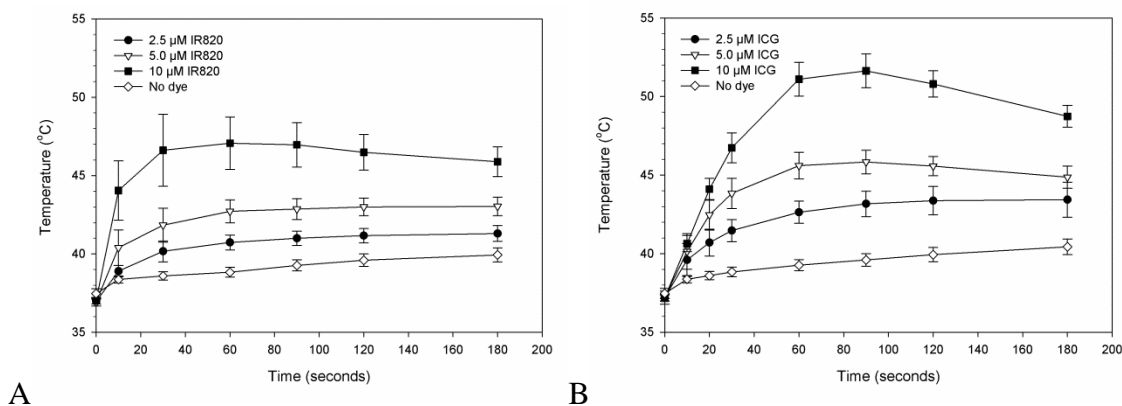


Figure 9. Heat generation profile of wells containing IR820 (A) or ICG (B) when irradiated with NIR laser for a total of 3 minutes.

Although IR820 did not generate peak temperatures as high as those of ICG after three-minute laser exposure, at 5 μM and 10 μM the IR820 temperatures were still within the

hyperthermia range of 40-43°C that is able to selectively impact tumor cell growth. Tumor cells are sensitive to temperatures in this range, whereas the growth of normal cells is not affected until temperatures reach higher levels (Baronzio et al., 2006). Although a higher concentration of IR820 will be needed to attain the same temperature as ICG in hyperthermia applications, it is still feasible to achieve temperatures in the desirable 40-43°C range with as little as 5 μ M IR820.

Samples from the 5 μ M stock solutions, kept at 4°C in the dark, were also tested 3 days and 6 days after the initial experiment to investigate the stability of heat generation properties after the dye is in solution. The hyperthermia properties of both dye solutions when irradiated with 808-nm light are stable over a period of 3 days, with no significant changes in peak temperature generation in terms of percent of original peak temperature recorded on the day of preparation. After 6 days, there is a significant decrease in peak temperature for both dyes ($p < 0.05$ compared to the initial peak). Even though the decrease is significant with respect to the initial time point, both dyes still reach peak temperatures higher than 41°C after 6 days. The stability of hyperthermia generation presents a stark contrast to the rapid decay of fluorescence properties in aqueous solution, indicating that non-radiative processes such as heat generation show a different behavior over time compared to radiative processes such as fluorescence.

3.2. Cellular Experiments

Cellular experiments included cytotoxicity experiments with and without hyperthermia, as well as fluorescent cell imaging.

3.2.1. Cytotoxicity experiments

Figures 10, 11, and 12 show the results of cytotoxicity experiments in SKOV-3, Dx5, and MES-SA cells, respectively.

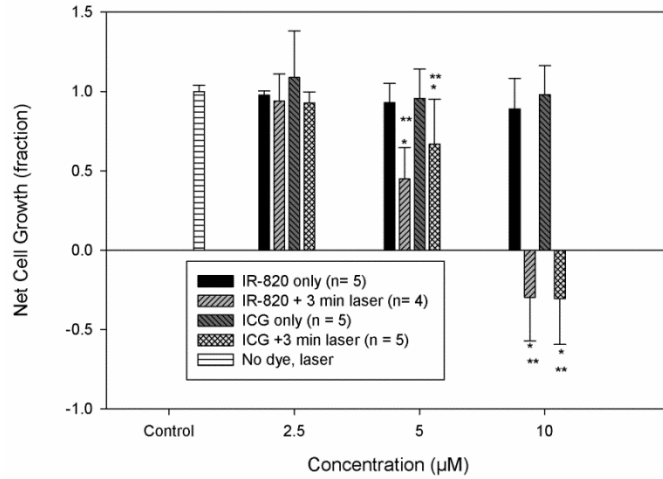


Figure 10. IR820 and ICG cytotoxicity and hyperthermia effects in SKOV-3 cells. * = significant difference ($p < 0.05$) versus control group; ** = significant difference ($p < 0.05$) versus same concentration of dye without laser.

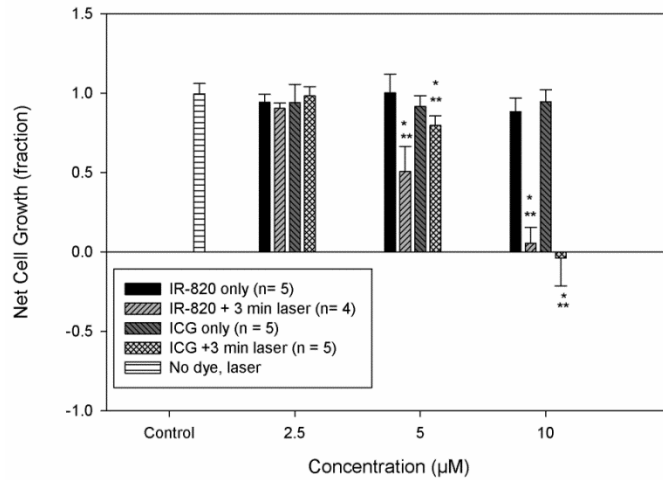


Figure 11. IR820 and ICG cytotoxicity and hyperthermia effects in Dx5 cells. * = significant difference ($p < 0.05$) versus control group; ** = significant difference ($p < 0.05$) versus same concentration of dye without laser.

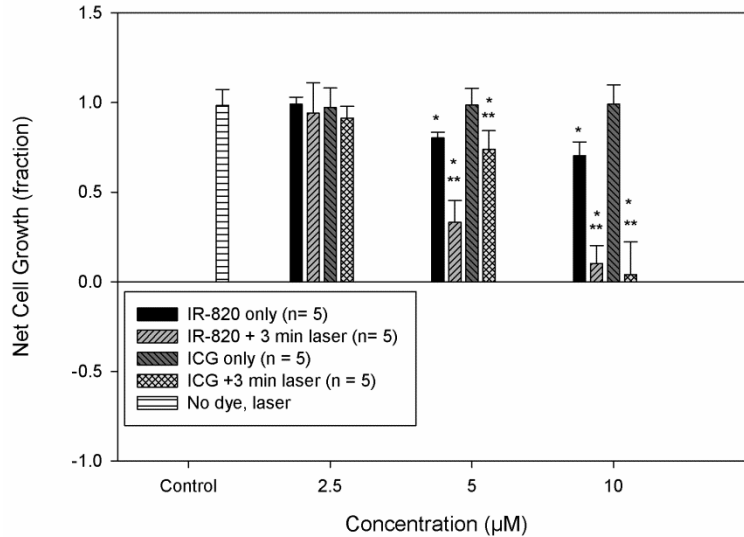


Figure 12. IR820 and ICG cytotoxicity and hyperthermia effects in MES-SA cells. * = significant difference ($p < 0.05$) versus control group; ** = significant difference ($p < 0.05$) versus same concentration of dye without laser.

Net cell growth was normalized to a control group that was not exposed to either dye or laser. NIR-laser treatment by itself without addition of IR820 or ICG did not affect cell viability for any of the cell lines. In the presence of ICG or IR820, the cytotoxicity profiles of SKOV-3 (Figure 10) and Dx5 (Figure 11) were very similar. In these two cell lines, concentrations up to 10 μM IR820 or ICG without laser treatment did not cause significant decreases in cell viability when compared to the control group that received no dye and no laser treatment. In MES-SA cells (Figure 12), there was significant ($p < 0.05$) cell growth inhibition upon exposure to 5 μM or 10 μM IR820 dye without laser treatment. This is likely due to the fact that MES-SA cells are more sensitive to environmental stressors than the other two cell lines, which are resistant to chemotherapy.

When compared to the group that received laser treatment only, laser treatment of cell lines exposed to IR820 or ICG caused significant ($p < 0.05$) cell growth inhibition at 5 μM dye concentration, and significant cell growth inhibition or cell killing at 10 μM , indicating that both dyes can cause hyperthermia that impacts cell viability. Additionally, for all cell lines, when comparing the effects of a given dye concentration with and without NIR-laser treatment, cell proliferation was significantly lower in the NIR laser treatment group versus the dye-only group for both dyes at 5 and 10 μM .

Thus, our cytotoxicity data shows that both IR820 and ICG hyperthermia cause significant cancer cell growth inhibition at 5 μM , and significant cell growth inhibition or cell killing at 10 μM . There is no statistical difference in the effect on net cell growth between IR820 and ICG hyperthermia for a given concentration, indicating that IR820 is a good substitute for ICG in therapeutic applications of hyperthermia.

3.2.2. In vitro cell imaging

Figure 13 shows images of MES-SA, SKOV-3, and Dx5 cells after 30-minute incubation with IR820 or ICG, at image exposure times well under the 20,000 ms threshold for cellular autofluorescence. The level of fluorescent brightness for both dyes allows for sensitive cell imaging of cancer cell lines, and IR820 images are very similar to those obtained with ICG. Similar dye distributions were observed for all cell lines in the fluorescence microscope images. Both dyes resulted in widespread cytoplasmic fluorescence along with a localized perinuclear signal. The cell images show some areas in the cytoplasm where the fluorescent intensity seems to be higher for both dyes. This may be due to intravesicle storage of the dyes (Quarta et al., 2009), or binding to

cytoplasmic proteins such as ligandin (Kaplowitz et al., 1975). Other researchers have reported that the amphiphilic characteristics of ICG cause specific interactions with the phospholipid bilayer (Desmettre et al., 2000), and the structural similarity of IR820 may result in similar interactions.

Image intensities for cells exposed to IR820 and ICG were comparable, despite the fact that our spectrofluorometer studies show smaller emission intensities for IR820 compared to ICG at equivalent concentrations. An additional consideration is that, based on its better stability in aqueous solution, it is possible that IR820 could show an advantage over ICG in long incubation periods and longer imaging windows.

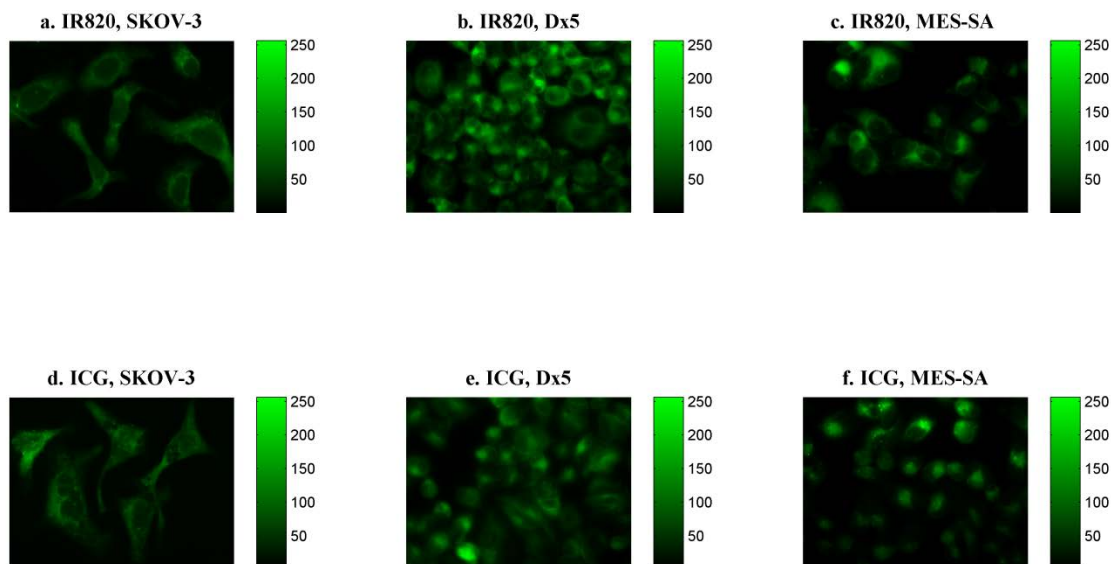


Figure 13. Cellular imaging after incubation with IR820 or ICG. A and D, SKOV-3 were incubated for 30 minutes with 10 μ M IR820 and ICG respectively. B and E, Dx5 were incubated for 30 minutes with 10 μ M IR820 and ICG respectively. C and F, MES-SA were incubated for 30 minutes with 10 μ M IR820 and ICG respectively. $\lambda_{\text{ex}} = 775$ nm and $\lambda_{\text{em}} = 845$ nm. Objective magnification, 60X.

3.3. In vivo Imaging Studies

Figure 14 shows sample abdominal images of a rat 40 minutes after i.v. injection with IR820 (14A) or ICG (14B) and excitation with a 60 mA 785-nm laser module. Both dyes accumulated primarily in the liver, which is consistent with literature reports for the biodistribution of ICG (Jiao et al., 2000). As expected from the lower fluorescence intensities observed during *in vitro* optical experiments, the intensity of the IR820 image following injection was lower than for the ICG image at equivalent molar dosages. An additional reason could be that our imaging system was optimized for ICG imaging with excitation at 785 nm. It is important to consider, however, that *in vitro* profiles cannot fully predict behavior in an *in vivo* environment, where protein and surface binding could have a large effect on fluorescent properties (Mordon et al., 1998). Interestingly, despite the initial larger signal for ICG, imaging the same animal after 24 hours resulted in normalized intensities that were higher for IR820 (14C) than for ICG (14D).

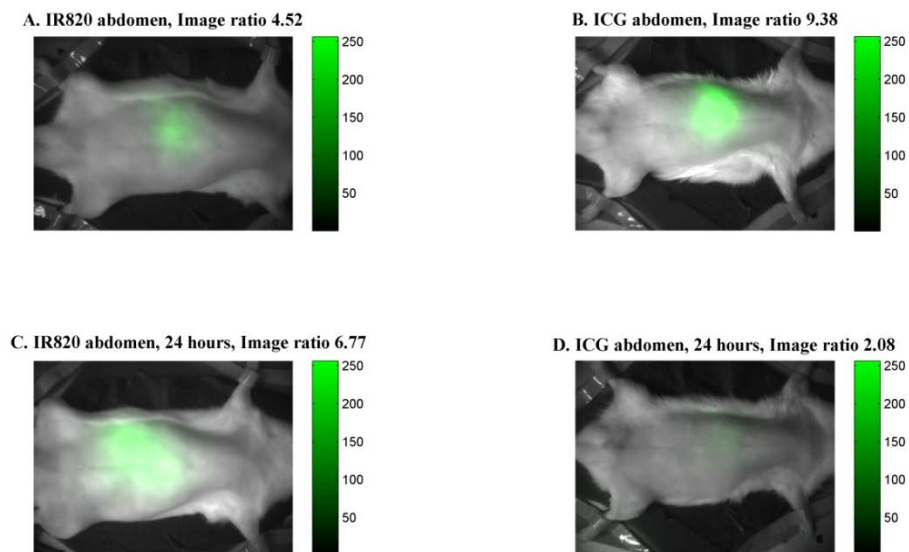


Figure 14. Rat abdomen images 40 minutes after i.v. injection with IR820 (A) or ICG (B), and 24 hours after injection with IR820 (C) or ICG (D). Image ratios indicate signal intensity normalized to area in μm^2 .

Area normalized image intensities (n=3) for IR820 and ICG are shown in Table 3. The quantitative measurements confirm that the abdominal ICG signal was significantly stronger than the abdominal IR820 signal immediately after injection ($p < 0.05$), but the opposite was true 24 hours later.

Image at 60 mA laser current	Image intensity per area, R ($1/\mu\text{m}^2$)	
	ICG (n =3)	IR820 (n=3)
Abdomen, 40 minutes after injection	11.49 \pm 2.49 (*)	4.74 \pm 0.52
Abdomen, 24 hours after injection	1.86 \pm 0.52	5.79 \pm 0.86 (*)
Liver, 24 hours after injection	7.01 \pm 4.01	14.87 \pm 2.90 (*)
Kidneys, 24 hours after injection	2.18 \pm 0.48	9.52 \pm 3.04 (*)
Lungs, 24 hours after injection	1.06 \pm 1.84	4.10 \pm 0.81 (*)

Table 3. Image intensity per area in μm^2 for different locations and time points after IR820 and ICG administration. Values are average \pm standard deviation. (*) = significant difference between dye signals, $p < 0.05$, for a given location and time point.

Also, when the organs were extracted and imaged after 24 hours, as shown in Figure 15, we can see that IR820 was present in liver, lungs and kidneys, whereas the ICG signal was mostly limited to the liver. In Table 3, this qualitative observation is confirmed by the area-normalized intensities, which are significantly higher ($p < 0.05$) for IR820 compared to ICG in liver, lungs, and kidneys 24 hours after the animal was injected with the dye.

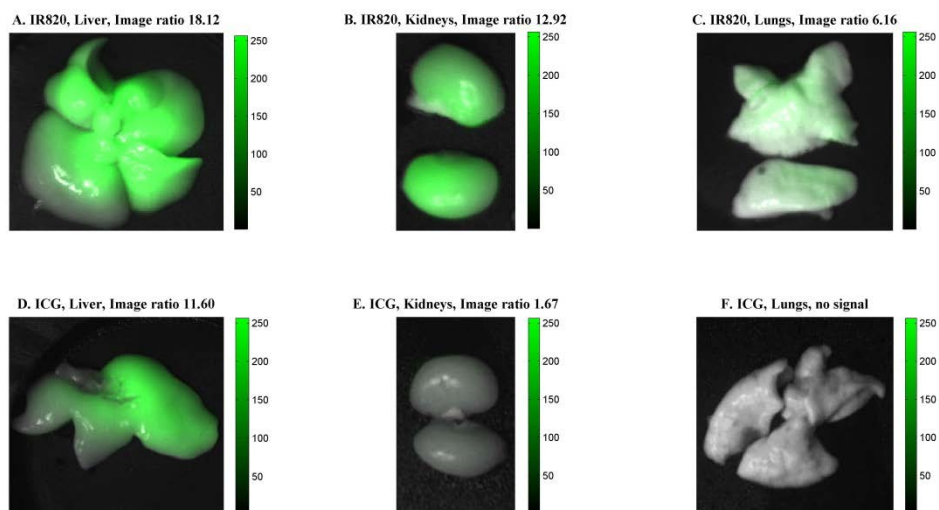


Figure 15. Rat liver, lung, and kidney images 24 hours after injection with IR820 or ICG. Ratios indicate signal intensity normalized to area in μm^2 .

Table 4 shows the quantitative organ dye content data obtained after homogenization and DMSO extraction.

	Organ dye content ($\mu\text{g/g}$ tissue)	
	ICG (n =3)	IR820 (n=3)
Liver	0.014 \pm 0.009	0.819 \pm 0.290 (*)
Lungs	0.021 \pm 0.026	0.066 \pm 0.018
Kidneys	0.005 \pm 0.002	0.166 \pm 0.020 (*)

Table 4. Organ dye content ($\mu\text{g/g}$ tissue) 24 hours after injection. Values shown are average \pm standard deviation, and (*) = significant difference, $p < 0.05$.

In accordance with the images shown above and the area-normalized intensities, organ content of IR820 ($\mu\text{g/g}$ tissue) was significantly higher ($p < 0.05$) than ICG in liver and

kidneys 24 hours post injection. For the lungs, IR820 content was higher than ICG content, but the difference did not reach statistical significance ($p = 0.066$).

Our rat organ studies showed that both dyes are processed primarily in the liver, but IR820 seems to significantly accumulate in the kidneys as well. Interestingly, when images were taken from the chest area after 24 hours, there was a signal from IR820 but not from ICG, indicating that IR820 may localize to the lungs to a larger extent than ICG. The lung image data is consistent with this observation, and shows a significant difference in intensity ratios for IR820 and ICG in the lungs ($p < 0.05$). However, the difference in lung dye content did not reach statistical significance ($p = 0.066$). In one of the ICG experiments, small “hot spots” were observed in the lungs 24 hours after injection, which may have been due to ICG aggregation in the blood resulting in lung accumulation. There was no ICG detected in the lungs of the other two rats 24 hours after injection. On the other hand, the lack of statistical significant could also be due to simple individual variability between subjects, which is also the source of other differences between fluorescent images.

In summary, after 24 hours we observed a stronger signal in the intact animal for IR820 compared to ICG, and both the organ images and quantitative dye content analysis show that IR820 is present in higher amounts than ICG in liver, kidneys, and lungs. This may result in an advantage over ICG for imaging studies by providing longer image collection windows, and is consistent with data reported by Prajapati *et al* (Prajapati et al., 2009). This group observed increases in IR820 fluorescence upon binding to serum albumin, and

they estimated that IR820 would have an approximate clearance half-life of 35 hours in mice based on the half-life of albumin and on images collected over a span of 8 days in mice. They did not take plasma samples or perform pharmacokinetic analysis upon *i.v.* injection. As we will discuss in chapter 6, our pharmacokinetic experiments in mice confirmed the increased plasma half-life of IR820 when compared to ICG. Our studies in mice support Prajapati's estimates, as well as the results discussed in the current chapter for the rat model.

3.4. Summary

IR820 could be an alternative to ICG in imaging and hyperthermia applications based on its enhanced stability, feasibility of use for *in vitro* and *in vivo* imaging, and hyperthermia generation properties. IR820 may be used under circumstances where longer image collection times or more predictable peak locations are desirable, and even though it does not elevate temperature as sharply as ICG for equimolar concentrations, IR820 is able to generate a cytotoxic environment upon laser exposure that can inhibit the growth of cancer cells, or even result in cell killing. The optimal dye concentration for dual *in vivo* imaging and hyperthermia treatment would depend on dye toxicity, hyperthermia tumor killing effect, plasma clearance and instrument sensitivity. Additional issues that must be considered include *in vivo* attenuation, as well as accumulation at desired target sites such as tumor areas. Potential approaches to solve these problems include targeted formulations of the dye, nanoformulations which can take advantage of the EPR effect, and endoscopic or orthoscopic delivery of light for imaging and inducing hyperthermia. The presence of the chlorohexene ring makes IR820 more amenable to conjugation

chemistry compared to ICG, and provides opportunities for preparation of conjugate formulations of the dye. Since aggregation of dye molecules is an important mechanism for degradation of cyanine dyes, covalent conjugation of IR820 to other moieties could result in formulations with enhanced stability. Versatility in selecting the conjugation moiety also opens opportunities for imparting different functionality or properties to the molecule. The development of specific nanoformulations of IR820 to enhance target site accumulation, exposure, and toxicity to cancer cells while providing longer windows for imaging and therapy may have significant potential as a theranostic approach to cancer management.

Chapter 3 References

- Baronzio, G. F., E. D. Hager, et al. (2006). On the Biochemical Basis of Tumour Damage by Hyperthermia. *Hyperthermia in Cancer Treatment: A Primer*, Springer US: 110-118.
- Desmettre, T., J. M. Devoisselle, et al. (2000). Fluorescence properties and metabolic features of indocyanine green (ICG) as related to angiography. *Surv Ophthalmol* **45**(1): 15-27.
- Fernandez-Fernandez, A., R. Manchanda, et al. (2012). Comparative study of the optical and heat generation properties of IR820 and indocyanine green. *Mol Imaging* **11**(2): 99-113.
- Jiao, L. R., A. A. El-Desoky, et al. (2000). Effect of liver blood flow and function on hepatic indocyanine green clearance measured directly in a cirrhotic animal model. *Br J Surg* **87**(5): 568-574.
- Kaplowitz, N., J. Kuhlenkamp, et al. (1975). Hepatic glutathione S-transferases: identification by gel filtration and in vitro inhibition by organic anions. *Proc Soc Exp Biol Med* **149**(1): 234-237.
- Lee, H., M. Y. Berezin, et al. (2008). Fluorescence lifetime properties of near-infrared cyanine dyes in relation to their structures. *J Photochem Photobiol A Chem* **200**(2-3): 438-444.
- Mac, M., A. Danel, et al. (2003). Investigations of the heavy atom effect occurring in bianthryl and 10,10[prime or minute]-dibromobianthryl. Fluorescence, cyclovoltamperometric and actinometric studies. *Physical Chemistry Chemical Physics* **5**(6): 988-997.
- Mordon, S., J. M. Devoisselle, et al. (1998). Indocyanine green: physicochemical factors affecting its fluorescence in vivo. *Microvasc Res* **55**(2): 146-152.
- Peng, X. J., F. L. Song, et al. (2005). Heptamethine cyanine dyes with a large stokes shift and strong fluorescence: A paradigm for excited-state intramolecular charge transfer. *J. Am. Chem. Soc.* **127**(12): 4170-4171.
- Prajapati, S. I., C. O. Martinez, et al. (2009). Near-infrared imaging of injured tissue in living subjects using IR-820. *Mol Imaging* **8**(1): 45-54.
- Quarta, A., A. Ragusa, et al. (2009). Bioconjugation of rod-shaped fluorescent nanocrystals for efficient targeted cell labeling. *Langmuir* **25**(21): 12614-12622.

Saxena, V., M. Sadoqi, et al. (2003). Degradation kinetics of indocyanine green in aqueous solution. *J Pharm Sci* **92**(10): 2090-2097.

Shimoda, A., T. Hikida, et al. (1979). Fluorescence quantum yields and lifetimes of dichlorobenzenes. *The Journal of Physical Chemistry* **83**(10): 1309-1312.

CHAPTER 4: PREPARATION AND CHARACTERIZATION OF IONIC IR820- PEG DIAMINE NANOCONJUGATES (IR820-PDNCs)

Clinical translation of NIR-imaging and hyperthermia approaches in cancer must overcome the challenges presented by free dye formulations in terms of plasma circulation times and non-specific biodistribution. Nanotechnology provides some opportunities to improve *in vivo* stability and target delivery. Intrinsic characteristics of nanoformulations such as size, surface moieties, and charge can be customized in order to modify their interactions with circulating proteins and cellular membranes. Additionally, due to their size, nanosize agents are less susceptible to reticuloendothelial system clearance, and in general have improved *in vivo* penetration into tissues and cells (Brigger et al., 2002; Xu et al., 2006). The enhanced permeability and retention (EPR) effect also acts as a passive targeting mechanism allowing nanoformulations to accumulate preferentially at tumor sites. Immune responses to circulating foreign objects can be reduced by coating nanoformulations with polyethylene glycol (PEG), thus resulting in improved plasma circulation times (Harris et al., 2001). PEG can also be utilized as a linker for antibody conjugation, which opens the possibility of actively targeted therapy to further reduce uptake in non-tumor areas and increase the efficacy and safety of these nanoformulations.

Specific aim #2 focused on the development and characterization of ionic IR820-PEG-diamine nanoplexes (IR820-PDNCs), and on researching their potential use in localized hyperthermia and imaging. The size and surface morphology of these nanoplexes were

characterized by SEM, and the optical properties in solution were studied using spectrofluorometry and spectrophotometry. We explored possible applications through *in vitro* experiments with three different human cancer cell lines (MES-SA, Dx5, and SKOV-3) to investigate the feasibility of using the nanoplexes as imaging agents, and to determine whether this formulation retained the ability to induce hyperthermic cell killing.

This work has been published as a full journal article (Manchanda et al., 2012). Permission has been obtained in writing from the journal editors to utilize images and content from this publication in the dissertation manuscript, and a copy of the aforementioned permission email is included in the appendices.

Materials and methods for this specific aim were discussed in chapter 2.

4.1. Characterization of IR820-PDNCs

Nanoplexes of PEG-diamine and IR820 were formed by electrostatic interactions between oppositely charged groups in PEG-diamine and IR820. Since IR820 is a monosodium salt, 50% of the molecules will remain in acid form at physiological pH. IR820-PDNCs size and morphology were characterized using SEM, which showed nanoplexes of approximately 50-100 nm diameter (Figure 16). The zeta potential of IR820-PDNCs was 2.0 ± 0.9 mV. PEG-diamine charges are neutralized during formulation, so the remaining charge arises primarily from the sodium salt charge of IR820 in its acid form and from nitrogen moieties. These charges make the nanoplexes

dispersible in aqueous solution, with PEG-mediated steric repulsion also playing a role in enhancing water dispersibility by preventing complex aggregation.

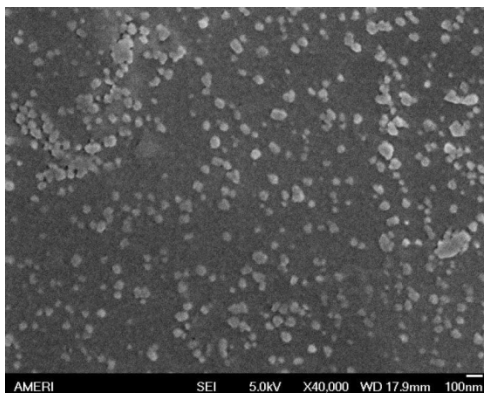


Figure 16. SEM image of IR820-PDNCs.

Particle yield was 25% for a 6k-PEG diamine formulation. IR820-PDNCs fluorescent dye content was determined by spectrofluorometry to be approximately 0.125 mg IR820/mg IR820-PDNCs. Samples of IR820-PDNCs were also analyzed by FTIR, $\nu = 1395 \text{ cm}^{-1}$ (C-S stretching), 1055 cm^{-1} (C-O-C stretching), 894 cm^{-1} (C-Cl stretching on conjugated dienes). These characteristic peaks indicate the participation of PEG-diamine as well as IR820 in the complex driven by electrostatic interactions. Although ionic formulations may not be as stable as a covalent linkage, ionic formulations have been used to provide improved delivery of therapeutic agents to cells (Nimesh et al., 2006), indicating that they have potential for clinical translation. Molecules coupled by electrostatic interactions typically maintain their native structure and activity, thus preserving their biological function (Wu et al., 2011). Ionic formulations may also present physiological advantages in terms of enhanced ion exchange processes or enhanced degradation after cellular internalization (Nimesh et al., 2006). Additionally,

many ionic formulations can be readily converted into covalent interactions through the use of coupling agents or linkers. The study of IR820-PDNCs can provide valuable information as to whether IR820 remains optically and thermally active when in close proximity to other molecules, and to determine whether molecular interactions impact its ability to function as a theranostic agent.

4.1.1. Absorbance studies

The UV-visible spectra of IR820, PEG-diamine and IR820-PDNCs are shown in Figure 17. Concentrations of PEG-diamine and IR820 were chosen based on molar ratios used in the formulation of the nanocomplexes, and IR820-PDNCs concentration was chosen to approximately match the concentration of the IR820 solution given the previously estimated dye content (0.125 mg IR820/mg IR820-PDNCs).

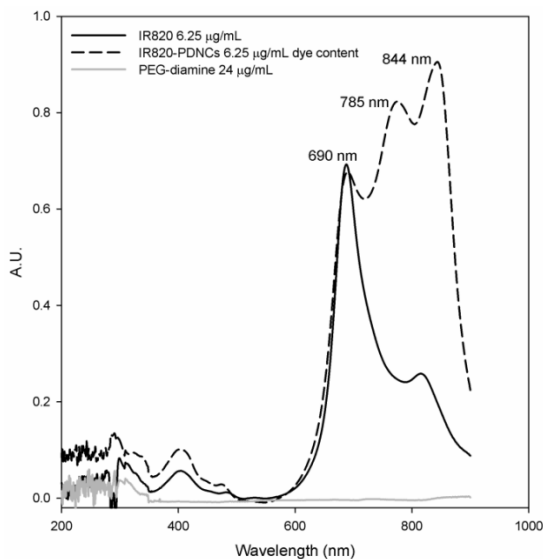


Figure 17. Absorption spectra of IR820 (solid black), IR820-PDNCs (dashed black) and PEG-diamine (gray) in deionized water.

IR820-PDNCs displayed three characteristic absorption peaks located at 690, 785, and 844 nm, between 0.677 and 0.906 A.U. at 6.25 $\mu\text{g/mL}$ dye concentration. There were no peaks above 0.01 A.U. between 200 and 900 nm for PEG-diamine at 24 $\mu\text{g/mL}$. The free dye spectrum showed a single peak at 688 nm with almost the same absorption intensity as the IR820-PDNCs solution. Therefore, the absorption spectra confirmed the validity of the spectrofluorometric dye content determination, based on the close match for the 688-690 nm peak. The other two peaks are unique to the nanoplex formulation and reflect additional vibrational transitions, which may stem from interactions between functional groups within the conjugate lattice, or from intermolecular hydrogen bonding (Mansoori et al., 2010)

4.1.2. Fluorescence properties of IR820-PDNCs

Excitation of IR820-PDNCs at 690 nm or 844 nm did not produce a significant fluorescence emission. There is probably translation of excitation energy into heat or vibrational energy at these wavelengths. After 785-nm excitation, the nanocomplexes demonstrated fluorescent emission. A representative fluorescence emission spectrum of IR820-PDNCs after 785-nm excitation is shown in Figure 18 along with the corresponding profile for IR820 at comparable dye content. The shape of the two profiles is quite similar, although the emission peak intensity is about 15% lower for IR820-PDNCs than IR820. The slight reduction in fluorescence intensity may be a result of interactions with the buffer solvent, changes in electronic excitation energy transfer mechanisms after the dye becomes part of the nanoplex lattice, absorption of fluorescence emission at secondary absorption peaks, or perhaps a combination thereof.

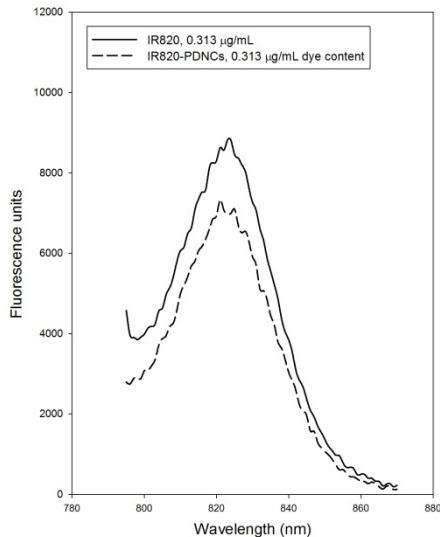


Figure 18. Fluorescence spectra of IR820 and IR820-PDNCs in phosphate buffered saline.

4.1.3. Fluorescence stability studies

IR820-PDNCs and IR820 solutions in buffer were measured 4 hours after preparation to determine the percent remaining fluorescent intensity compared to baseline. IR820-PDNCs showed a significantly ($p < 0.05$) higher percent remaining intensity (68.9%) compared to IR820 (58.9%) after 4 hours. This indicates that the ionic interactions within the nanoplex lattice conferred added stability and protected the dye from degradation.

4.2. Cell Imaging Studies

Figure 19 shows fluorescence microscopy images of Dx5, SKOV-3 and MES-SA cell lines after 2.5 hours incubation at 5 µM concentration of IR820 and IR820-PDNCs at equivalent dye content. This concentration was chosen based on our previous cellular studies with IR820 (Fernandez-Fernandez et al., 2012). In all three cell lines, intense fluorescence was observed inside the cells after 2.5 hour incubation with IR820 or IR820-

PDNCs, indicating that both the free dye and the nanoplexes were capable of entering the cells. However, the images taken after IR820-PDNCs incubation showed higher normalized intensity ratios than those taken after incubation with equivalent concentrations of IR820, especially in SKOV-3 and Dx5. Normalized intensity ratios for IR820-PDNCs were 2.1 times larger than for IR820 in SKOV-3 ($R = 2.6$ for IR820 versus $R = 5.6$ for IR820-PDNCs) and 1.7 times larger in Dx5 ($R = 3.8$ for IR820 versus $R = 6.5$ for IR820-PDNCs). In MES-SA, the ratio showed a moderate increase ($R = 5.7$ for IR820 versus $R = 6.9$ for IR820-PDNCs).

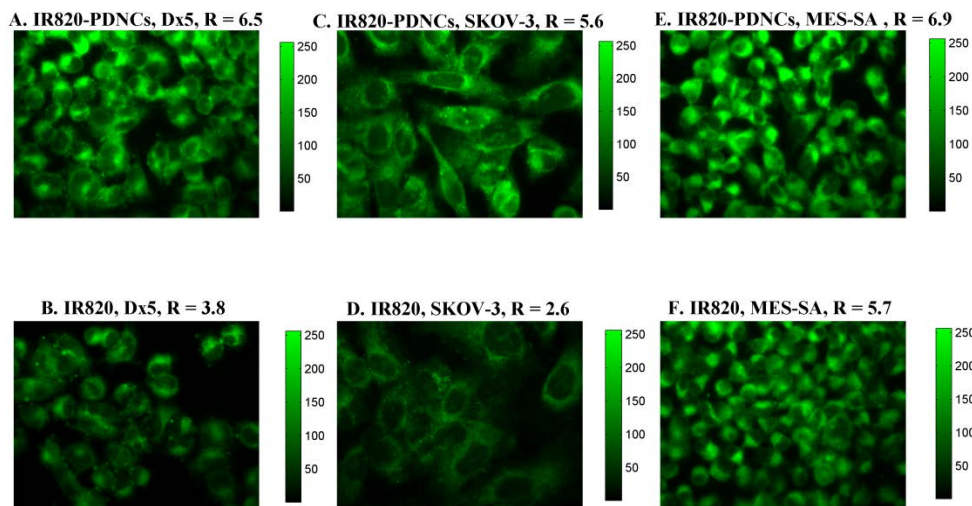


Figure 19. Cellular imaging of Dx5 (A, B), SKOV-3 (C,D) and MES-SA cells (E,F) after 2.5 hour incubation with 5 μ M dye content of IR820-PDNCs (top) or IR820 (bottom); 60x, exposure time 4000 ms.

It is possible that the presence of PEG resulted in enhanced cell membrane interaction and increased internalization compared to free dye, as PEG has been reported to mediate solubilization of nanoformulations in the lipid bilayer. This results in enhanced solubility in cell membranes and increased non-specific cellular uptake (Yamazaki et al., 1990; Zhang et al., 2002). High concentrations of PEG in close proximity to cellular

membranes create osmotic stress and osmoelastic coupling, which result in membrane instability, enhanced leakiness and PEG-induced fusion vesicles without the need for direct contact with PEG (Yamazaki et al., 1990). It is possible that exposure of cells to IR820-PDNCs creates such an effect based on the osmotic effects of PEG, even if some of the charge was neutralized during nanocomplex formation.

4.3. Cytotoxicity Studies without Hyperthermia

SKOV-3, Dx5 and MES-SA cells were chosen to study the cytotoxic effect of IR820 and IR820-PDNCs on tumor cells using the SRB assay. The cells were incubated with increasing concentrations of IR820 or IR820-PDNCs for 24 hours up to a maximum dose of 5 μ M IR820 content, in order to compare the toxicity profile of the nanoplexes and the free dye. Figure 20 shows net cell growth following incubation with IR820 or IR820-PDNCs for SKOV-3, Dx5, and MES-SA.

There was no significant difference in net cell growth between the IR820 group and the IR820-PDNCs group for equivalent dye concentrations for any cell line. In SKOV-3 and Dx5, there was also no significant cytotoxicity for any concentration of IR820 or IR820-PDNCs compared to the control group which was not exposed to dye. On the other hand, MES-SA cells showed significant ($p < 0.05$) 17-25% cell growth inhibition at 5 μ M concentrations of either treatment, consistent with our prior observations discussed in chapter 3, and again likely due to the fact that MES-SA cells are more sensitive to environmental stressors than the other two cell lines, which are resistant to chemotherapy.

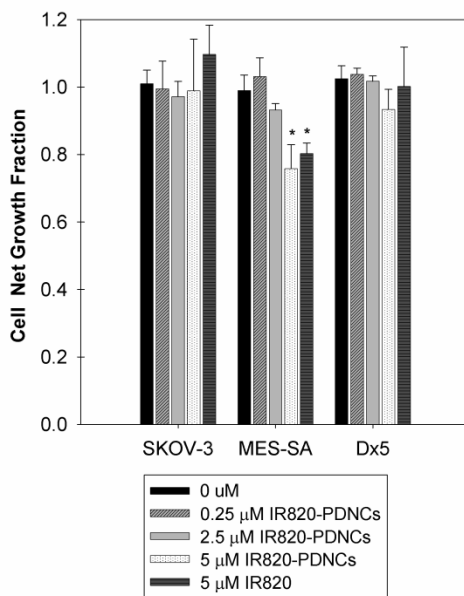


Figure 20. Cytotoxicity of IR820-PDNCs or IR820 in cancer cell lines. Bars represent net cell growth after 24-hour exposure, n = 3 experiments, 4 wells per treatment. * = significant difference ($p < 0.05$) versus control (0 μ M) group.

We also performed studies with exposure to (1) dye content of 25 μ M, which resulted in > 50% growth inhibition in all three cell lines for both IR820 and IR820-PDNCs; and (2) PEG-diamine at 50 μ M concentration, which is 20 times higher than the concentration of PEG-diamine in nanoplexes containing 5 μ M of IR820, and showed no toxicity in any of the cell lines. The overall cytotoxicity results indicated that IR820-PDNCs have a toxicity profile comparable to the free dye, and they can be safely used up to at least 5 μ M, which is within the applicable range for biological studies such as imaging.

4.4. Hyperthermia Studies

Our previous work has shown the ability of IR820 to induce hyperthermic cell growth inhibition and cell killing (Fernandez-Fernandez et al., 2012). We tested IR820-PDNCs

to determine whether the dye within the nanoplex still retained the ability to generate heat when exposed to an 808-nm NIR laser. At a laser fluence rate of 8 W/cm², a solution of 0.034 mg/ml IR820-PDNCs (containing 5 μM IR820) caused an increase in temperature from 37°C to 42.5°C after 3 minutes of exposure. This temperature is within the range used for localized hyperthermia aiming to affect tumor cells while sparing healthy cells.. Research has shown that moderate hyperthermia (41-43 °C) is able to cause significant tumor cell growth inhibition but does not greatly affect healthy cells. The reason for this differential behavior upon hyperthermia exposure is that cancer cells have mechanisms that inhibit oxidative metabolism which are specifically activated by temperatures in this range (Cavaliere et al., 1967; Luk et al., 1980; Tang et al., 2009). We also tested PEG-diamine by itself, which did not result in significant changes in temperature after 3-minute laser exposure compared to wells containing medium only. Therefore, hyperthermia generation stems from the IR820 portion of the nanoplexes.

Nanoplex-induced hyperthermia may have the potential to enhance toxicity compared to free dye based on factors unique to the nanoformulation such as size, charge, enhanced interaction with cell membranes, or overall increased internalization of the nanoplexes. In order to study the effects of nanoplex hyperthermia on cellular systems, we tested MES-SA, Dx5 and SKOV-3 cell proliferation with and without laser irradiation. The results are shown in Figure 21. All groups were normalized to the control group not exposed to dye or laser. As discussed in chapter 3, there was no significant effect of laser exposure on cell growth without exposure to dye. Cell growth was significantly inhibited in all three cell lines by both IR820 and IR820-PDNCs when exposed to laser. In MES-SA and Dx5

cell lines, IR820-PDNCs hyperthermia resulted in significantly higher cytotoxicity ($p < 0.05$) compared to IR820. In SKOV-3 cells, IR820-PDNCs hyperthermia produced higher cytotoxicity than free dye, but not enough to reach statistical significance.

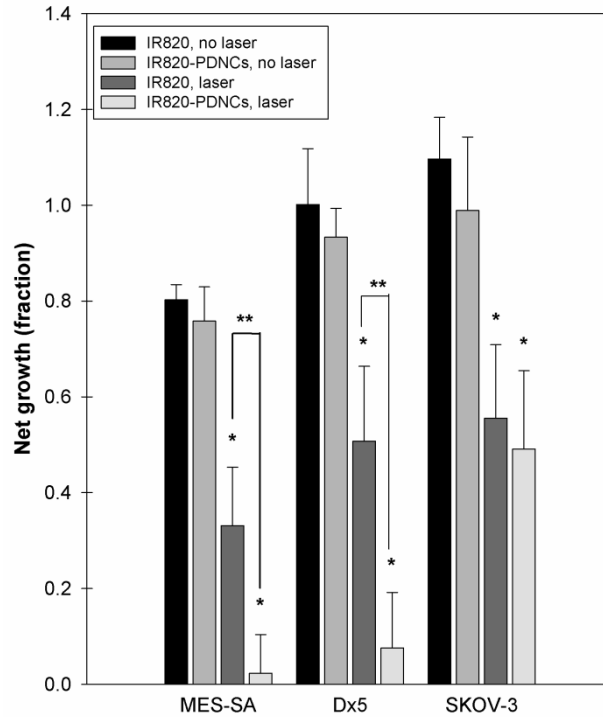


Figure 21. Cytotoxicity of hyperthermia treatment with 5 μM dye content of IR820 or IR820-PDNCs, $n = 3$ experiments, 4 wells/experiment. All groups are normalized to the control group not exposed to dye or laser. There was no significant effect of laser exposure per se without IR820-PDNCs or IR820, and there was no significant effect of PEG-diamine exposed to laser. * = significant difference ($p < 0.05$) versus non-laser group, ** = significant difference ($p < 0.05$) between laser groups.

Based on the cell imaging results displayed in Figure 19, IR820-PDNCs were internalized more readily by cells than the free dye. This is consistent with the increased cytotoxicity effect of the hyperthermia treatment that can be observed in Figure 21. Enhanced internalization would result in improved ability to cause damage to cells by

heat generation compared to free dye. It is interesting to note that the enhanced cytotoxic effect reached statistical significance in MES-SA and Dx5 cell lines, but not in SKOV-3. This could be due to inherent insensitivity to hyperthermia in SKOV-3. These cells have a p53 deletion gene mutation that affects their response to different cytotoxic agents. It is possible that the mutation may also influence apoptotic response to hyperthermia events, although this issue is controversial.

Some studies suggest that hyperthermia-induced apoptosis is independent of p53 mutations (Fukami et al., 2004; Sturm et al., 2006). Tang et al found that simultaneous use of ICG hyperthermia and doxorubicin chemotherapy in SKOV-3 resulted in increased cell growth inhibition compared to chemotherapy alone or hyperthermia alone. This would seem to indicate that these cells can still be affected by hyperthermia despite the p53 mutation (Tang et al, 2009). However, other groups have reported that the process of apoptosis after hyperthermia can depend on p53 expression and may occur in both a p53-dependent and -independent manner (Goto et al., 1999; Ohnishi et al., 2008; Seo et al., 1999; Takahashi et al., 2003). Further studies are needed to clarify the effect of p53 gene deletion on the response to localized NIR-dye mediated hyperthermia.

Given that PEG diamine has the potential to generate peroxide radicals upon light exposure, it may create increased oxidative stress in cells exposed to a laser. In order to explore this possibility, we also tested a PEG-diamine only group. MES-SA, Dx5, and SKOV-3 were exposed to 2.5 μ M PEG-diamine (based on the molar formulation ratio of 1:2 PEG-diamine to IR820) and received laser treatment as previously described. Our

results showed that there were no significant differences in cell growth ($p>0.05$) for the PEG plus laser group compared to either the control group that was not exposed to PEG-diamine, or to the group that received PEG-diamine without laser treatment. Therefore, PEG-diamine by itself did not cause oxidative stress levels able to significantly affect cell growth after laser exposure.

Our results showed an enhanced effect of IR820-PDNCs hyperthermia in Dx5 and MES-SA cells. Increases in cell internalization may play a role in explaining this difference, but the co-localization of PEG-diamine and IR820 could also be an important factor to consider. Although PEG-diamine free radical generation is not sufficient to significantly affect cell growth, research has shown that the presence of free radical generators can enhance the effect of hyperthermia, because some mechanisms of cell death in hyperthermia are tied to oxidative stress responses (Li et al., 2001; Skibba et al., 1997; Wada et al., 2005; Yuki et al., 2003).

In the case of IR820-PDNCs, which contain both IR820 and PEG-diamine, it is possible that simultaneous increased temperature (from IR820 hyperthermia) and free radical generation (from PEG-diamine laser exposure) could have resulted in enhanced cytotoxicity compared to free dye hyperthermia for Dx5 and MES-SA cells, even if free radical generation from PEG-diamine in isolation does not have an effect. This could provide an advantage to the nanoplex formulation with respect to individual therapies by achieving codelivery and combined action of its components.

4.5. Summary

Under this specific aim, we successfully prepared ionic nanocomplexes of IR820 and PEG-diamine (IR820-PDNCs), characterized their optical properties and investigated their cytotoxicity with and without laser exposure in cancer cell lines MES-SA, SKOV-3 and Dx5. The nanoplexes were able to generate a cytotoxic hyperthermia effect, as well as to emit a fluorescence signal that can be used for imaging. This formulation can potentially provide an advantage over the use of free agents by enhancing cell uptake, allowing simultaneous co-localization of imaging and therapy, and accentuating the cytotoxic effect of hyperthermia. Modifications in nanoplex formulation to create covalent conjugates could improve on the stability of the lattice and result in nanosize conjugates that may be used in *in vivo* applications.

Chapter 4 References

- Brigger, I., C. Dubernet, et al. (2002). Nanoparticles in cancer therapy and diagnosis. *Adv. Drug Delivery Rev.* **54**(5): 631-651.
- Cavaliere, R., E. C. Ciocatto, et al. (1967). Selective heat sensitivity of cancer cells. Biochemical and clinical studies. *Cancer* **20**(9): 1351-1381.
- Fernandez-Fernandez, A., R. Manchanda, et al. (2012). Comparative study of the optical and heat generation properties of IR820 and indocyanine green. *Mol Imaging* **11**(2): 99-113.
- Fukami, T., S. Nakasu, et al. (2004). Hyperthermia induces translocation of apoptosis-inducing factor (AIF) and apoptosis in human glioma cell lines. *J. Neurooncol.* **70**(3): 319-331.
- Goto, A., K. Shomori, et al. (1999). Hyperthermia-induced apoptosis occurs both in a p53 gene-dependent and -independent manner in three human gastric carcinoma cell lines. *Oncol. Rep.* **6**(2): 335-339.
- Harris, J. M., N. E. Martin, et al. (2001). Pegylation: a novel process for modifying pharmacokinetics. *Clin. Pharmacokinet.* **40**(7): 539-551.
- Li, F. J., T. Kondo, et al. (2001). Enhancement of hyperthermia-induced apoptosis by a free radical initiator, 2,2'-azobis (2-amidinopropane) dihydrochloride, in human histiocytic lymphoma U937 cells. *Free Radic Res* **35**(3): 281-299.
- Luk, K. H., R. M. Hulse, et al. (1980). Hyperthermia in cancer therapy. *West J Med* **132**(3): 179-185.
- Manchanda, R., A. Fernandez-Fernandez, et al. (2012). Nanoplexes for cell imaging and hyperthermia: in vitro studies. *J Biomed Nanotechnol* **8**(4): 686-694.
- Mansoori, N., K. S. Brandenburg, et al. (2010). A Comparative Study of Two Folate-Conjugated Gold Nanoparticles for Cancer Nanotechnology Applications. *Cancers* **2**: 1911-1928.
- Nimesh, S., A. Goyal, et al. (2006). Polyethylenimine nanoparticles as efficient transfecting agents for mammalian cells. *J. Control. Release* **110**(2): 457-468.
- Ohnishi, T., A. Takahashi, et al. (2008). p53 Targeting can enhance cancer therapy via radiation, heat and anti-cancer agents. *Anticancer Agents Med. Chem.* **8**(5): 564-570.

- Seo, Y. R., M. L. Smith, et al. (1999). Mild hyperthermia-induced apoptosis is dependent on p53 in human lymphoid cells. *Res. Commun. Mol. Pathol. Pharmacol.* **104**(3): 285-292.
- Skibba, J. L. and E. A. Gwartney (1997). Liver hyperthermia and oxidative stress: role of iron and aldehyde production. *Int J Hyperthermia* **13**(2): 215-226.
- Sturm, I., B. Rau, et al. (2006). Genetic dissection of apoptosis and cell cycle control in response of colorectal cancer treated with preoperative radiochemotherapy. *BMC Cancer* **6**: 124.
- Takahashi, A., I. Ota, et al. (2003). p53-dependent hyperthermic enhancement of tumour growth inhibition by X-ray or carbon-ion beam irradiation. *Int J Hyperthermia* **19**(2): 145-153.
- Tang, Y. and A. J. McGoron (2009). Combined effects of laser-ICG photothermotherapy and doxorubicin chemotherapy on ovarian cancer cells. *J. Photochem. Photobiol. B* **97**(3): 138-144.
- Wada, S., Z. G. Cui, et al. (2005). A hydrogen peroxide-generating agent, 6-formylpterin, enhances heat-induced apoptosis. *Int J Hyperthermia* **21**(3): 231-246.
- Wu, S., A. Buthe, et al. (2011). Organic-Soluble Enzyme Nano-Complexes Formed by Ion-Pairing with Surfactants. *Nanoscale Biocatalysis - Methods in Molecular Biology* **743**: 51-63.
- Xu, Z. P., Q. H. Zeng, et al. (2006). Inorganic nanoparticles as carriers for efficient cellular delivery. *Chem. Eng. Sci.* **61**(3): 1027-1040.
- Yamazaki, M. and T. Ito (1990). Deformation and instability in membrane structure of phospholipid vesicles caused by osmophobic association: mechanical stress model for the mechanism of poly(ethylene glycol)-induced membrane fusion. *Biochemistry* **29**(5): 1309-1314.
- Yuki, H., T. Kondo, et al. (2003). A free radical initiator, 2,2'-azobis (2-aminopropane) dihydrochloride enhances hyperthermia-induced apoptosis in human uterine cervical cancer cell lines. *Free Radic Res* **37**(6): 631-643.
- Zhang, Y., N. Kohler, et al. (2002). Surface modification of superparamagnetic magnetite nanoparticles and their intracellular uptake. *Biomaterials* **23**(7): 1553-1561.

CHAPTER 5: PREPARATION AND CHARACTERIZATION OF COVALENT IR820-PEG DIAMINE NANOCONJUGATES (IRPDcov)

Specific aim #3 focused on the development and characterization of covalent IR820-PEG-diamine nanoconjugates (IRPDcov), and on researching their potential use in localized hyperthermia and imaging. The size and surface morphology of these nanoconjugates were characterized by SEM, conjugation was confirmed by H-NMR, and the optical properties in solution were studied using spectrofluorometry and spectrophotometry. We explored possible applications through *in vitro* experiments with three different human cancer cell lines (MES-SA, Dx5, and SKOV-3) to investigate the feasibility of using the nanoconjugates as imaging agents, and to determine whether this formulation retained the ability to induce hyperthermic cell killing. Promising results led to *in vivo* testing, which is discussed under chapter 6 as specific aim #4.

The work described in chapters 5 and 6 is currently a manuscript in preparation for submission to the Journal of Biomedical Optics.

Materials and methods for specific aim # 3 were discussed in chapter 2.

5.1. Characterization of IRPDcov

Covalent nanoconjugates of PEG-diamine and IR820 were prepared by mixing IR820 and 6kDa PEG-diamine (2:1 ratio) in methanol and refluxing for 4 hours in the presence of triethylamine (2 eq.), with displacement of the chlorine atom by nucleophilic

substitution and production of triethylamine hydrochloride. Then, the solvent was removed, the residue dissolved in water, dialyzed against water, freeze-dried, and stored in powder form at 4°C for further use. IRPDcov size and morphology were characterized using SEM, which showed nearly-spherical uniformly distributed nanoconjugates of approximately 150 nm diameter (Figure 22). Hydrodynamic diameter (DLS) measurements were around 348 nm, whereas the SEM image showed smaller particle sizes. This difference is expected because DLS measures hydration and swelling of the conjugates in an aqueous phase, which results in increased diameters compared to the dry sample in SEM. The zeta potential of IRPDcov was -0.4 ± 0.3 mV, due to charge neutralization during formulation. The nanoconjugates are soluble in aqueous solution, and PEG-mediated steric repulsion assists in preventing the formation of aggregates, with a solubility limit of approximately 2 mg IRPDcov/mL in deionized water.



Figure 22. SEM image of IRPDcov.

Particle yield was 74% for a 6k-PEG diamine formulation. IRPDcov fluorescent dye content was determined by spectrofluorometry to be approximately 0.113 mg IR820/mg

IRPDcov. Samples of IRPDcov in deuterated methanol were also analyzed by H-NMR, which confirmed conjugate formation. Figure 23 illustrates the H-NMR spectrum of the conjugate denoting the main identifiable peaks. The conjugate spectrum contains peaks contributed both from IR820 and PEG-diamine, which suggests that we have indeed made the conjugate. Any unreacted IR820 would have been removed during the dialysis process, so the presence of aromatic peaks (in the region between 7 and 9 ppm) indicates that the covalent linkage between IR820 and PEG-diamine was successful. It is important to note that there are small extra peaks in the spectrum that indicate that the sample is not completely pure, however, this can be attributed to the fact that IR820 is only available as a commercial grade chemical.

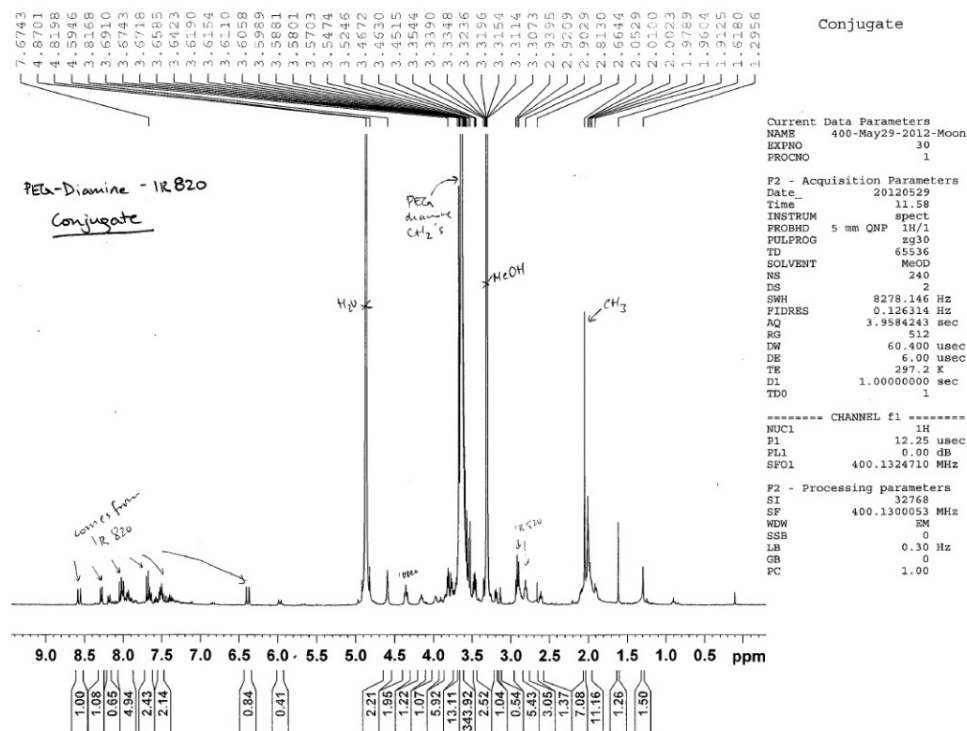


Figure 23. H-NMR spectrum of IRPDcov in deuterated methanol.

5.1.1. Absorbance studies

The UV-visible spectra of IR820, PEG-diamine and IRPDcov are shown in Figure 24. Concentrations of PEG-diamine and IR820 were chosen based on molar ratios used in the formulation of the nanocomplexes, and IRPDcov concentration was chosen to approximately match the concentration of the IR820 solution given the previously estimated dye content (0.113 mg IR820/mg IRPDcov).

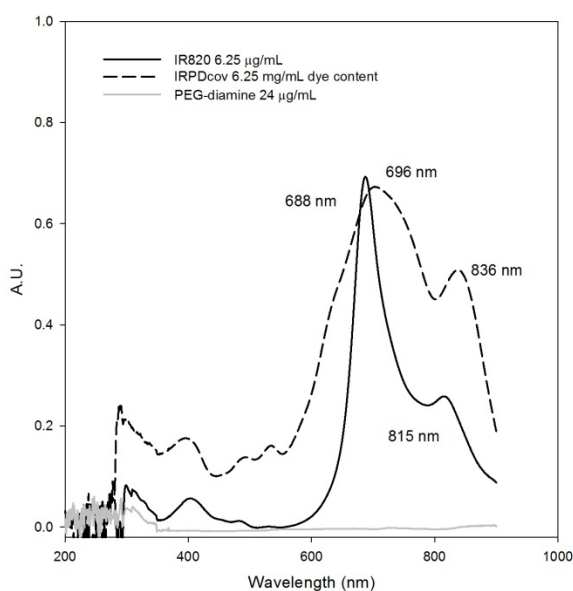


Figure 24. Absorption spectra of IR820 (solid black), IRPDcov (dashed black) and PEG-diamine (gray) in deionized water.

IRPDcov displayed a bathochromic main absorption peak shift compared to IR820 (IRPDcov λ_{\max} = 696 nm, IR820 λ_{\max} = 688 nm) as well as a shift in the secondary absorption peak (located at 836 nm for IRPDcov versus 815 nm for IR820). These shifts can be attributed to the formation of an extended π system by the conjugation process. There was also an overall broadening of the spectral profile. Increased absorption and

scattering within the environment of the nanoconjugate may explain the spectral observations. There were no peaks above 0.01 A.U. between 200 and 900 nm for PEG-diamine at 24 $\mu\text{g}/\text{mL}$. The free dye spectrum showed a single peak at 688 nm with almost the same absorption intensity as the IRPDcov solution, confirming our dye content determination.

5.1.2. Fluorescence properties of IRPDcov

A representative fluorescence emission spectrum of IRPDcov after 785-nm excitation is shown in Figure 25 along with the corresponding profile for IR820 at comparable dye content. After 785-nm excitation, the peak emission for IRPDcov was located at 822 nm, with fluorescence intensity 6% smaller than IR820. The slight reduction in fluorescence intensity may be due to absorption of emitted fluorescence at secondary absorption peaks.

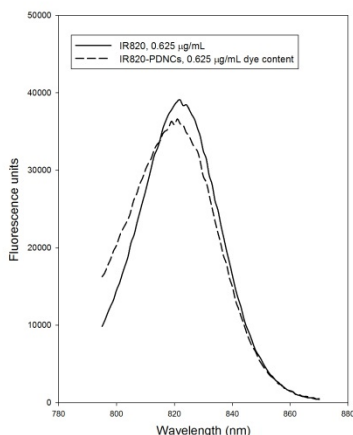


Figure 25. Fluorescence spectra of IR820 and IRPDcov in phosphate buffered saline.

In the case of IR820-PDNCs which were formulated by ionic interactions, fluorescence intensity of the conjugates was approximately 15% less than that of free dye. Therefore,

the covalent formulation demonstrates improved fluorescence with respect to the ionic formulation, likely by reducing unwanted interactions between IR820 and the buffer solvent.

5.1.3. *Fluorescence stability studies*

IRPDcov and IR820 solutions in buffer were measured up to 72 hours after preparation to determine the percent remaining fluorescent intensity compared to baseline. Samples were kept at 4°C in the dark. The decrease in fluorescence from baseline after 72 hours was significantly lower for IRPDcov (39.9% decrease) compared to IR820 (80% decrease), $p < 0.05$. This indicates that covalent conjugation provides significant stabilization to the dye, likely as a result of increased rigidity of the IR820 molecule by incorporation into the nanoconjugate lattice, which would reduce intermolecular IR820 aggregation. PEG-mediated steric hindrance may also play a role in preventing aggregation of IR820 molecules and the subsequent degradation process. The enhanced preservation of fluorescence properties also indicates that the conjugate is stable as formulated for at least 72 hours, based on the large differences in fluorescence observed between conjugate and free dye samples after that time period.

5.2. **Cell Imaging Studies**

Figure 26 shows fluorescence microscopy images of Dx5, SKOV-3 and MES-SA cell lines after 4 hours incubation at 5 μ M concentration of IR820 and IRPDcov at equivalent dye content. This concentration was chosen based on our previous cellular studies with IR820 (Fernandez-Fernandez et al., 2012). In all three cell lines, intense fluorescence was

observed inside the cells after 4 hour incubation with IR820 or IRPDcov, indicating that both the free dye and the nanoconjugates were capable of entering the cells. However, the images taken after IRPDcov incubation showed higher normalized intensity ratios than those taken after incubation with equivalent concentrations of IR820, especially in Dx5. Normalized intensity ratios were 1.8 times larger for IRPDcov than for IR820 in Dx5, 1.4 times larger in MES-SA, and 1.2 times larger in SKOV-3.

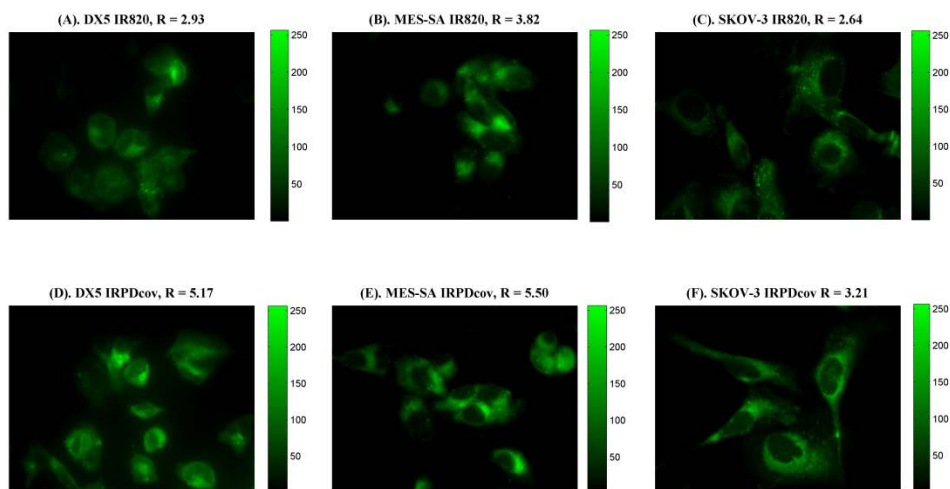


Figure 26. Cellular imaging of Dx5 (A, B), SKOV-3 (C,D) and MES-SA cells (E,F) after 4 hour incubation with 5 μ M dye content of IRPDcov (top) or IR820 (bottom); 60x, exposure time 4000 ms.

We had previously discussed how PEG can enhance cell membrane interaction and increase cell internalization by osmoelastic coupling and formation of PEG-induced fusion vesicles (Yamazaki et al., 1990; Zhang et al., 2002). In the case of IRPDcov, this may be one of the contributing factors to the enhanced internalization shown by the fluorescent images, as direct contact with PEG is not necessary to induce such effects. In comparison to the ionic IR820-PDNCs, IRPDcov produce comparable increases in internalization for Dx5 (1.7 increase ionic, 1.8 covalent) and MES-SA (1.2 increase ionic,

1.4 covalent), and a smaller increase in SKOV-3 (2.1 increase ionic, 1.2 covalent). Taking into consideration the additional fact that incubation times were 2.5 hours for the ionic agent versus 4 hours for the covalent formulation, it seems that IRPDcov does not result in as much enhancement in cellular internalization as the ionic formulation. This is likely due to the fact that IRPDcov charge is near neutral, which would not facilitate interaction with the typically negatively-charged cancer cell membranes (Albanese et al., 2012). Another factor that may account for the difference is that IRPDcov are larger in diameter than the ionic formulation, and this may cause slower diffusion through the cell membrane. Ionic IR820-PDNCs are smaller and have a small positive charge, which may result in increased interaction with negative membranes and larger increases in internalization based on a combination of size effects, osmotic stress, and charge effects. However, IRPDcov still show enhanced internalization compared to free dye, most likely as a result of the PEG-induced osmotic effect. We must also weigh that *in vitro* behavior is not the only important parameter to consider. Having a near neutral or zwitterionic nanoformulation has its own advantages, such as prolonged plasma half-lives and reduced clearance, which will be important for *in vivo* applications (Arvizo et al., 2011) and could render IRPDcov superior to IR820-PDNCs.

5.3. Cytotoxicity and Hyperthermia Studies

We tested IRPDcov to determine whether the dye in nanoconjugate form was still able to generate heat upon exposure to an 808-nm NIR laser. At a laser fluence rate of 8 W/cm², a solution of 0.038 mg/ml IRPDcov (containing 5 μM IR820) caused an increase in temperature from 37°C to 42.2°C after 3 minutes of exposure, demonstrating that

covalent binding of IR820 did not interfere with heat generation properties. As previously discussed, this temperature is in the moderate hyperthermia range (41-43 °C) which can cause significant tumor cell growth inhibition but does not greatly affect healthy cells. We also tested PEG-diamine by itself, which did not result in significant changes in temperature after 3-minute laser exposure compared to wells containing medium only. Therefore, the IR820 component of the nanoconjugates is responsible for hyperthermia generation.

SKOV-3, Dx5 and MES-SA cells were chosen to study the cytotoxic effect of IR820 and IRPDcov on tumor cells with and without hyperthermia. Figure 27 shows net cell growth following incubation with IR820 or IRPDcov, with or without exposure to laser, for SKOV-3, Dx5, and MES-SA. All groups were normalized to the control group not exposed to dye or laser.

Without laser, IRPDcov demonstrates toxicity comparable to the free dye. There was no significant toxicity in SKOV-3 or Dx5 compared to the control group which was not exposed to IRPDcov or IR820, and there was a slight growth inhibition in MES-SA cells for IRPDcov treatment, consistent with our previous observations for IR820. There was no significant difference in net cell growth between the IR820 group and the IRPDcov group without laser exposure for any cell line, indicating that IRPDcov can be safely used up to at least 5 μ M. From our previous studies, we determined that laser exposure by itself or PEG-diamine by itself did not cause any significant effect on cell growth for any of the three cell lines (Manchanda et al., 2012).

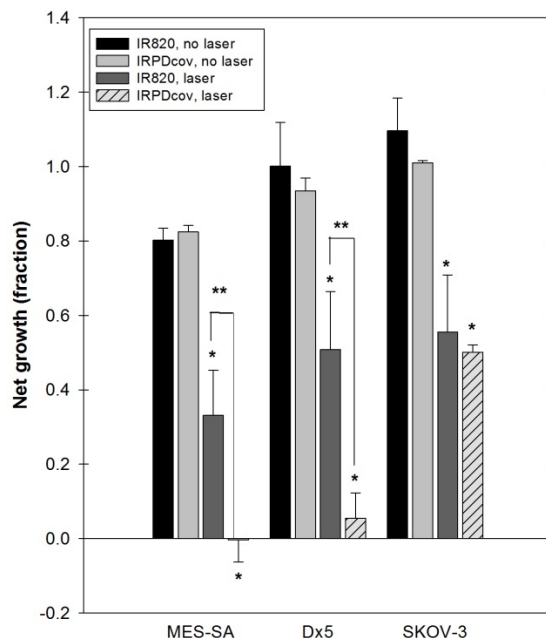


Figure 27. Cytotoxicity of IRPDcov or IR820 in cancer cell lines, with or without hyperthermia treatment at 5 μ M dye concentration, n = 3 experiments, 4 wells/experiment. All groups are normalized to the control group not exposed to dye or laser. There was no significant effect of laser exposure per se without IRPDcov or IR820, and there was no significant effect of PEG-diamine exposed to laser. * = significant difference ($p < 0.05$) versus non-laser group, ** = significant difference ($p < 0.05$) between laser groups.

When exposed to laser, cell growth was significantly inhibited in all three cell lines by both IR820 and IRPDcov. In MES-SA and Dx5 cell lines, IRPDcov hyperthermia resulted in significantly higher cytotoxicity ($p < 0.05$) compared to IR820. In the case of MES-SA, IRPDcov plus laser resulted in cell killing, versus IR820 plus laser which caused cell growth inhibition. In SKOV-3 cells, IRPDcov hyperthermia produced higher cytotoxicity than free dye, but not enough to reach statistical significance. Based on the cell imaging results displayed in Figure 26, there may be a larger degree of internalization for IRPDcov than for free dye. This is consistent with the increased

cytotoxicity effect of the hyperthermia treatment that can be observed in Figure 27. Enhanced internalization would result in larger accumulation of the dye inside the cell and an accentuated damaging effect of temperature increases within the cell. This seems to be most apparent in MES-SA cells, where laser exposure of cells treated with IRPDcov resulted in a cell killing effect.

When comparing ionic IR820-PDNCs and covalent IRPDcov conjugates, there were no statistically significant differences in cell growth inhibition between the two formulations. For both conjugates, the hyperthermia enhanced cytotoxic effect versus free dye reached statistical significance in MES-SA and Dx5 cell lines, but not in SKOV-3. This further solidifies the hypothesis that there could be an inherent insensitivity to hyperthermia in SKOV-3, possibly related to the p53 deletion mutation that could affect apoptotic responses. These results are consistent with similar observations reported by other researchers who were unable to induce death in SKOV3 cells by treating them with branched gold nanoparticles exposed to laser at 38 W/cm^2 for 5 minutes with an 11°C temperature increase (Van de Broek et al., 2011), even though the thermal cross section of gold nanoparticles is higher than that of organic dyes (Yguerabide et al., 1998). It is apparent that SKOV-3 has inherent thermotolerance. Hyperthermia-induced cytotoxicity is controlled by both p53-dependent and-independent pathways (Fukami et al., 2004; Ohnishi et al., 2008; Sturm et al., 2006). Based on existing knowledge, thermosensitivity and thermotolerance depend on an array of biological, genetic, and environmental factors, so that a specific cause for SKOV-3 thermotolerance within the context of our studies cannot be determined.

As previously discussed in chapter 4, PEG-diamine by itself does not cause oxidative stress levels able to significantly affect cell growth after laser exposure. However, for both IR820-PDNCs and IRPDcov, our results showed an enhanced effect of hyperthermia in Dx5 and MES-SA cells. Increases in cell internalization may play a role in explaining this difference, but the co-localization of PEG-diamine and IR820 could also have an effect based on the fact that some mechanisms of cell death in hyperthermia are tied to oxidative stress responses (Li et al., 2001; Skibba et al., 1997; Wada et al., 2005; Yuki et al., 2003). IRPDcov nanoconjugates may provide advantages over IR820 alone based on simultaneous hyperthermia and free radical generation creating a toxic environment for cancer cells.

5.4. Summary

Under this specific aim, we successfully prepared nanocomplexes of IR820 and PEG-diamine (IRPDcov) and investigated cellular uptake and cytotoxicity in cancer cell lines MES-SA, SKOV-3 and Dx5. The nanoconjugates were able to generate a cytotoxic hyperthermia effect, as well as to emit a fluorescence signal that can be used for imaging. The IPDcov formulation can potentially provide an advantage over the use of free agents by significantly enhancing the stability of the NIR dye, increasing cell internalization, allowing simultaneous co-localization of imaging and therapy, and accentuating the cytotoxic effect of hyperthermia. Additionally, the conjugate nanosize can provide the advantage of passive targeting by the EPR effect. The next step toward clinical application is performing animal studies to determine the behavior of the conjugate *in vivo* in terms of biodistribution and plasma pharmacokinetics. The expectation is that, due

to the presence of PEG, the nanoconjugate will have prolonged distribution and elimination half-lives with respect to the free dye, resulting in advantages for theranostic applications.

Chapter 5 References

- Albanese, A., P. S. Tang, et al. (2012). The effect of nanoparticle size, shape, and surface chemistry on biological systems. *Annu Rev Biomed Eng* **14**: 1-16.
- Arvizo, R. R., O. R. Miranda, et al. (2011). Modulating pharmacokinetics, tumor uptake and biodistribution by engineered nanoparticles. *PLoS One* **6**(9): e24374.
- Fernandez-Fernandez, A., R. Manchanda, et al. (2012). Comparative study of the optical and heat generation properties of IR820 and indocyanine green. *Mol Imaging* **11**(2): 99-113.
- Fukami, T., S. Nakasu, et al. (2004). Hyperthermia induces translocation of apoptosis-inducing factor (AIF) and apoptosis in human glioma cell lines. *J. Neuro-Oncol.* **70**(3): 319-331.
- Li, F. J., T. Kondo, et al. (2001). Enhancement of hyperthermia-induced apoptosis by a free radical initiator, 2,2'-azobis (2-amidinopropane) dihydrochloride, in human histiocytic lymphoma U937 cells. *Free Radic Res* **35**(3): 281-299.
- Manchanda, R., A. Fernandez-Fernandez, et al. (2012). Nanoplexes for cell imaging and hyperthermia: in vitro studies. *J Biomed Nanotechnol* **8**(4): 686-694.
- Ohnishi, T., A. Takahashi, et al. (2008). p53 Targeting can enhance cancer therapy via radiation, heat and anti-cancer agents. *Anti-Cancer Agents Med. Chem.* **8**(5): 564-570.
- Skibba, J. L. and E. A. Gwartney (1997). Liver hyperthermia and oxidative stress: role of iron and aldehyde production. *Int J Hyperthermia* **13**(2): 215-226.
- Sturm, I., B. Rau, et al. (2006). Genetic dissection of apoptosis and cell cycle control in response of colorectal cancer treated with preoperative radiochemotherapy. *BMC Cancer* **6**: 124.
- Van de Broek, B., N. Devoogdt, et al. (2011). Specific cell targeting with nanobody conjugated branched gold nanoparticles for photothermal therapy. *ACS Nano* **5**(6): 4319-4328.
- Wada, S., Z. G. Cui, et al. (2005). A hydrogen peroxide-generating agent, 6-formylpterin, enhances heat-induced apoptosis. *Int J Hyperthermia* **21**(3): 231-246.
- Yamazaki, M. and T. Ito (1990). Deformation and instability in membrane structure of phospholipid vesicles caused by osmophobic association: mechanical stress model for the mechanism of poly(ethylene glycol)-induced membrane fusion. *Biochemistry* **29**(5): 1309-1314.

- Yguerabide, J. and E. E. Yguerabide (1998). Light-scattering submicroscopic particles as highly fluorescent analogs and their use as tracer labels in clinical and biological applications. *Anal. Biochem.* **262**(2): 137-156.
- Yuki, H., T. Kondo, et al. (2003). A free radical initiator, 2,2'-azobis (2-aminopropane) dihydrochloride enhances hyperthermia-induced apoptosis in human uterine cervical cancer cell lines. *Free Radic Res* **37**(6): 631-643.
- Zhang, Y., N. Kohler, et al. (2002). Surface modification of superparamagnetic magnetite nanoparticles and their intracellular uptake. *Biomaterials* **23**(7): 1553-1561.

**CHAPTER 6: BIODISTRIBUTION AND PHARMACOKINETIC STUDIES
OF COVALENT IR820-PEG DIAMINE NANOCONJUGATE (IRPD_{cov}), IR820,
AND ICG IN MICE**

In vitro studies can provide valuable information, predicting the *in vivo* behavior of therapeutic agents by informing us of their physicochemical characteristics in an aqueous environment and inside cells, however, they cannot reflect the complexity of an actual living system. Studies using an animal model are the natural follow-up to *in vitro* studies of a molecule or agent that shows promise based on *in vitro* experimental results. In our case, we proceeded to study the biodistribution and pharmacokinetics of IRPD_{cov} in a mouse model, and established a comparison with free IR820 as well as ICG in the same model. The questions we wanted to answer were:

1. Can the IRPD_{cov} conjugate be used for *in vivo* optical imaging?
2. Is there any difference in biodistribution between IRPD_{cov}, IR820, and ICG?
3. Is there any difference in pharmacokinetic behavior of IRPD_{cov}, IR820, and ICG in terms of half-life and other pharmacokinetic parameters?

Biodistribution and pharmacokinetics studies are typically done in mice due to their low cost, ease of handling, and the valuable information they can provide. Mouse models have been successfully used in many instances of preclinical exploration to determine pharmacokinetic behavior and safety of drug candidates before they are tested in humans (European Commission, 2010). There are many examples in the literature of *in vivo* testing of optical and therapeutic agents, in their free forms as well as nanoformulations,

using mouse models. Some examples include studies of the pharmacokinetics of different formulations of paclitaxel (gel, film, prodrug, liposomes and micelles) in Swiss mice (Dhanikula et al., 2005); the biodistribution of ICG versus ICG-PLGA nanoparticles in C57BL/6 mice (Saxena et al., 2006); the biodistribution of ICG versus ICG-containing electrostatically assembled mesocapsules (MCs) in Swiss Webster mice (Yaseen et al., 2009); the biodistribution of inorganic luminescent nanoparticles in healthy Swiss mice as well as tumor-bearing C57BL/6 mice (de Chermont et al., 2007); among countless others.

Different models can be used in pharmacokinetic analysis to try to approximate the behavior of a molecular agent *in vivo*. In the compartmental approach, the researcher assumes that the drug will be distributed into one or more so called “compartments”, which represent distinct regions of the body, such as organs or body fluids (Fournier, 2007). In this model, an input function represents drug administration, an output function represents drug clearance, and mass transfer can occur between compartments at specific rates (Truskey et al., 2009).

The most straightforward approach to compartmental modeling is to assume the body is a single compartment. In one compartment models of i.v. bolus administration, the assumption is that the agent under study distributes uniformly in the body. A drug injection goes into the “central compartment”, which has a specific volume, and is eliminated by either inactivation of the agent by metabolism, or excretion in urine and feces (Truskey et al., 2009).

A one-compartment model is illustrated in figure 28.

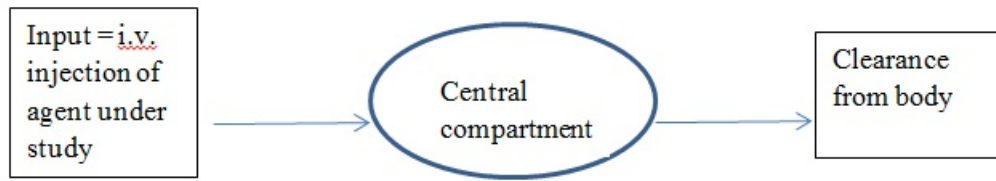


Figure 28. Exemplification of a one-compartment model for pharmacokinetic studies.

Concentration of a molecule over time in one-compartment models can be represented mathematically by a monoexponential decay equation of the form

$$C(t)=C_0*e^{-kt} \quad \text{Equation 4}$$

where $C(t)$ is the concentration as a function of time, C_0 is the modeled initial concentration, k is the rate constant for clearance, and t is time. The rate constant can be used to calculate half-life, the amount of time it takes for 50% of the agent to disappear from the system, as follows:

$$t_{1/2} = \frac{\ln(2)}{k} \quad \text{Equation 5}$$

A more complex approach is the two-compartment model, which takes into account the fact that molecule transport in plasma is often different from transport in tissue. In a two compartment model of i.v. bolus administration, the central compartment represents plasma and well-perfused organs such as the liver, whereas another compartment called the peripheral compartment represents other organs which uptake the agent (Truskey et al., 2009). The input injection and the output clearance are still assumed to be happening to and from the central compartment, but there is also bidirectional mass transfer between

the central compartment and the peripheral compartment (Fournier, 2007). Figure 29 illustrates the concept of a two-compartment model.

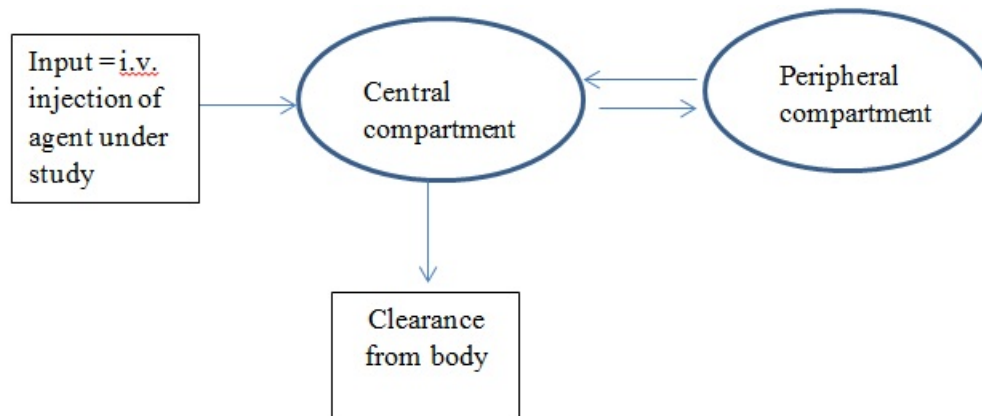


Figure 29. Exemplification of a two-compartment model for pharmacokinetic studies.

In a two-compartment model, pharmacokinetic behavior is biphasic and is characterized by two distinct phases called distribution and elimination. In the initial distribution phase, the agent rapidly equilibrates in solution in the central compartment comprised of plasma and other fluids, and is simultaneously (1) being eliminated from the central compartment by liver metabolism and kidney excretion, and (2) moving towards or distributing into the peripheral compartment comprised of other tissues (Bauer, 2008; Truskey et al., 2009). Although elimination occurs during this phase, the governing process is distribution. The initial distribution phase corresponds to rapidly declining plasma concentrations. At the end of this phase, both compartments momentarily equilibrate reaching steady state, but the concentration gradient is quickly reversed by the fact that elimination continues to occur in the central compartment, and the second phase starts. In the subsequent slowly-progressing second phase, the predominant process is elimination, as the agent is redistributed from the peripheral compartment to the central

compartment and is eventually cleared from the body (Bauer, 2008; Fournier, 2007). Concentration vs. time profiles in a two-compartment model can be represented mathematically by a bi-exponential decay equation of the form:

$$C(t)=A*e^{-at}+B*e^{-bt} \quad \text{Equation 6}$$

where $C(t)$ is the concentration as a function of time, A and B are constants whose sum models the initial concentration, a is the rate constant for distribution, b is the rate constant for elimination, and t is time (Truskey et al., 2009). From this model, we can calculate two separate half-lives, one for distribution (initial, rapidly-declining phase) and one for elimination (slower second phase), based on their corresponding time constants. The distribution half-life is given by

$$t_{1/2} = \frac{\ln 2}{a} \quad \text{Equation 7}$$

And the elimination half-life is given by

$$t_{1/2} = \frac{\ln 2}{b} \quad \text{Equation 8}$$

For small molecules, higher order compartmental models with a larger number of compartments may be appropriate to fully understand their behavior in different tissues (Truskey et al., 2009). In this case, one would follow the same exponential decay models that were previously described, but with additional terms representing mass transfer between different compartments.

As is the case for any model, compartmental models are obviously an oversimplification of a living system. The choice of a specific compartmental model to represent a set of data is commonly dictated by expected physiological behavior, the goodness of fit between data and model, and the degree of improvement in fit when a higher order model is used. Although a higher order model will often give a better fit, the improvement may not be significant enough to justify the introduction of complexity into the model, and there are some inherent dangers in “overfitting” data, such as creating a model that cannot be generalized (Zuegge et al., 2001). The common approach in the absence of prior knowledge to guide the researcher seems to be to start with the simplest model possible, including those reported for agents that could theoretically have a similar behavior. One can then progress toward increasingly complex models until a satisfactory fit is achieved.

A way to interpret goodness of fit is to look at the root mean square error (*RMSE*). Given the error *E* as the difference between experimental data and predicted data at a given time point *t*, the *RMSE* is calculated as:

$$RMSE = \sqrt{\frac{1}{n} \sum_{i=0}^t (E_i)^2} \quad \text{Equation 9}$$

The advantage of the *RMSE* is that it is given in the same units as the original data, so that it can provide a representation of the size of the average error. As a way to determine the percent error inherent in our model -and thus in parameters that are computed from

said model- we can use the root mean square percentage error (*RMSPE*). To calculate *RMSPE*, we calculate the percent error for each prediction and compute *RMSPE* as:

$$PE=100* \frac{\text{predicted value-observed value}}{\text{observed value}} \quad \text{Equation 10}$$

$$RMSPE=\sqrt{\frac{1}{n} \sum_{i=0}^t (PE_i)^2} \quad \text{Equation 11}$$

Obtaining the value of *RMSPE* allows us to estimate the percent error that is to be expected in parameters derived from model equations.

6.1. Study Design

Thirty-six healthy ND4 Swiss-Webster outbred mice, weighing between 25 and 30 grams, were purchased from Harlan (Indianapolis, IN). Animals were housed at the FIU Animal Care Facility under a 12-hour light/dark cycle and fed ad libitum. All IUCAC regulations were followed. Table 5 reflects group assignments.

	15 minutes	30 minutes	60 minutes	24 hours
IRPDcov	Group 1	Group 4	Group 7	Group 10
IR820	Group 2	Group 5	Group 8	Group 11
ICG	Group 3	Group 6	Group 9	Group 12

Table 5. Study design for biodistribution experiments of IRPDcov, IR820 and ICG in mice. Each group was comprised of 3 mice.

Mice were randomly assigned to groups based on optical agent (ICG, IR820, or IRPDcov), and time point of data collection after injection (15 minutes, 30 minutes, 60 minutes, and 24 hours). Random assignment was performed by card draw, with n=3 for each group.

6.2. Specific Methodology

6.2.1. Injection and dosage

The literature recommends that a safe i.v. injection volume for mice is 0.2 mL (Wolfensohn et al., 2003), and other authors have used a 0.24 mg/kg dose of dye for studies of optical agents in mice (Rajagopalan et al., 2000). Following these guidelines, animals were weighed and the appropriate solution concentration for this injection volume based on desired dosage was calculated as follows:

- a. For free dye, we used a 0.24 mg/kg dose, i.e.:

$$\text{Injection mass} = (\text{mouse weight in kg}) * \left(0.24 \frac{\text{mg}}{\text{kg}}\right)$$

$$\text{Solution concentration} = \frac{\text{injection mass}}{0.2 \text{ mL}}$$

- b. For conjugate, we used a 0.24 mg dye/kg dose by adjusting for conjugate dye content, as follows:

$$\text{Injection mass} = (\text{mouse weight in kg}) * \left(0.24 \frac{\text{mg}}{\text{kg}}\right) * \left(\frac{\text{mg dye}}{\text{mg conjugate}}\right)$$

$$\text{Solution concentration} = \frac{\text{injection mass}}{0.2 \text{ mL}}$$

For example: for a 25-g mouse,

$$0.025 \text{ kg} * \frac{0.24 \text{ mg IR820}}{\text{kg}} * \frac{1 \text{ mg IRPDcov}}{0.113 \text{ mg IR820}} = 0.053 \text{ mg IR820PDcov}$$

For an injection volume of 0.2 mL,

$$\text{need solution of } \frac{0.053 \text{ mg IRPDcov}}{0.2 \text{ mL}} = 0.265 \frac{\text{mg IRPDcov}}{\text{mL}}$$

Solutions for injection were prepared by first dissolving the agents in small volumes of deionized water, and then diluting in saline solution to the final desired concentration. Then, 0.2 mL of the solution was placed in a 1-mL syringe with a 30g needle, and the syringe was covered with aluminum foil to protect it from light. The use of a 30g needle (instead of the 26g needles utilized in the rat studies) was chosen to accommodate the smaller diameter and size of the mouse tail veins. Also, because of the small volumes allowed, no flushing was performed and a direct method of injection was used instead of the three-way stopcock method we had utilized in rats. Before the injection, an infrared lamp was used to warm the tail, dilate the veins and facilitate visual localization of the injection site.

6.2.2. Time sequence of blood and organ sampling

Mice in groups 1-9 were anesthetized with i.p. pentobarbital (100 mg/kg obtained from a 10 mg/mL stock solution), shaved, placed supine on the imaging setup, injected through the tail vein with their assigned agent, and imaged. At the predetermined time point while under anesthesia, a blood sample was obtained by heart puncture into the ventricle, and the animal was then euthanized by removal of the heart. For mice in groups 4-9, the pentobarbital dose was given in two injections, the first 50 mg/kg before imaging, and the

second 50 mg/kg administered 15 minutes before the terminal time point. The dose was split in this manner, rather than given in a single dose, in order to ensure survival until the terminal time point. For mice in groups 10-12, each animal was anesthetized with 40 mg/kg of i.p. pentobarbital, injected with the assigned agent, and imaged. These mice were then returned to their cage alive until the 24-hour time point. After 24 hours, they were anesthetized with 100 mg/kg of i.p. pentobarbital and imaged again under the same operating conditions. After imaging, a blood sample was obtained by heart puncture, and organs were carefully harvested for imaging and subsequent homogenization and dye extraction. These animals were finally euthanized by removal of the heart.

6.2.3. In vivo imaging techniques

The same general techniques for animal and organ imaging that were described in chapter 2 were followed for the mice studies, including the setup used and the software for processing the data.

6.2.4. Plasma and organ sample processing

Plasma and organ sample processing followed the procedures described by other researchers who have performed biodistribution studies of NIR dyes and related compounds (Saxena et al., 2006; Yaseen et al., 2009). In the case of blood samples, immediately after collection the samples were centrifuged 2x for 3 minutes at 12,000 rpm to extract plasma. Plasma samples were then incubated in DMSO (1 plasma: 50 DMSO) in glass vials covered with aluminum foil for thirty minutes and centrifuged again. The resulting supernatant was used to perform spectrofluorometric measurements of dye

concentration in plasma using a previously created calibration curve of IR820 or ICG in DMSO at 785-nm excitation.

For organ samples in the 24-hour groups, organs were carefully dissected and placed in black-coated Petri dishes for imaging as previously described for our rat studies. Fluorescent organs were then cut into small pieces using a scalpel, placed in pre-weighed glass vials, and homogenized using a tissue homogenizer. The vials with homogenized samples were reweighed, and 5 mL of DMSO was added for dye extraction. Samples were incubated in DMSO for 4 hours covered with aluminum foil, and centrifuged at 9,000 rpm for 15 minutes. The supernatant was used to perform spectrofluorometric measurements of dye content using a previously created calibration curve of IR820 or ICG in DMSO at 785-nm excitation. To report the data, organ dye content was normalized to organ mass.

6.2.5. Pharmacokinetic analysis of plasma data

Dye concentration in plasma obtained from spectrofluorometer measurements was averaged for each group, and the average concentration for each time point was entered into Matlab (MathWorks, Natick, MA). The initial concentration (concentration at injection) was estimated for an average 25-g mouse. The injected amount was approximately 6 μg dye based on the 0.24 mg/kg standardized dosage, with a mouse plasma volume of approximately 1.5 mL based on literature ratios of 58.5 mL plasma /kg body weight (Macon et al., 2011). This results in an initial concentration of approximately 4 μg dye/mL in plasma.

Using the curvefit tool in Matlab, average data points at 0, 15, 30, 60 minutes, and 24 hours were fit to both monoexponential and biexponential curves via a least squares algorithm. As discussed before, researchers attempting to model pharmacokinetic behavior often choose to start with the simplest model that is theoretically sound for a given set of experimental data, and progress to more complicated models as needed based on fit results. In our case, literature shows that ICG pharmacokinetics have been modeled by other authors with either a one-compartment or a two-compartment model approach (Achilefu et al., 2002). Given these sources, there is justification to attempt to fit the data for ICG, IR820, and IRPDcov to monoexponential and biexponential curves as an initial approach. We do not truly know if these will be appropriate for IR820 and IRPDcov, because nothing has been reported in the literature regarding IR820 pharmacokinetics, and IRPDcov is a novel conjugate. Regardless, it seems wise to start our modeling efforts by utilizing what has been reported by others for ICG. We would expect the behavior of these agents to be somewhat similar to ICG, especially in the case of IR820. Thus, we focused on one-compartment and two-compartment pharmacokinetic models. The resulting monoexponential and biexponential fit equations were used to determine the overall half-life (in the case of the monoexponential model), or the half-lives of distribution and elimination (in the case of the biexponential model). Other calculated pharmacokinetic values included the area under the pharmacokinetic curve, the mean plasma residence time, and the clearance rate.

The area under the curve (AUC) is the integral of the concentration vs. time curve, which we calculated using Simpson's rule.

$$\text{Area under the curve} = \text{AUC} = \int_0^{\infty} C(t)dt \quad \text{Equation 12}$$

The mean residence time in plasma, t_p , is the average time spent by the agent of interest in plasma, and is given in its simplest expression by:

$$\text{Mean plasma residence time} = t_p = \frac{\text{AUC}}{C_0} \quad \text{Equation 13}$$

where C_0 is the modeled original concentration. This value corresponds to the coefficient C_0 in a monoexponential model, and to the sum of coefficients $A+B$ in a biexponential model.

The total body clearance rate (i.e. volume of agent cleared from the body per unit time) is given by:

$$\text{Total body clearance rate} = \frac{\text{Dose}}{\text{AUC}} \quad \text{Equation 14}$$

Based on the preceding calculations, we compared IRPDcov, IR820 and ICG pharmacokinetic parameters using one-way ANOVA ($p < 0.05$) followed by Bonferroni post-hoc test.

6.3. Results and Discussion

6.3.1. Animal imaging

Figure 30 shows representative images obtained from ICG, IR820, and IRPDcov animals 15 minutes and 24 hours after injection.

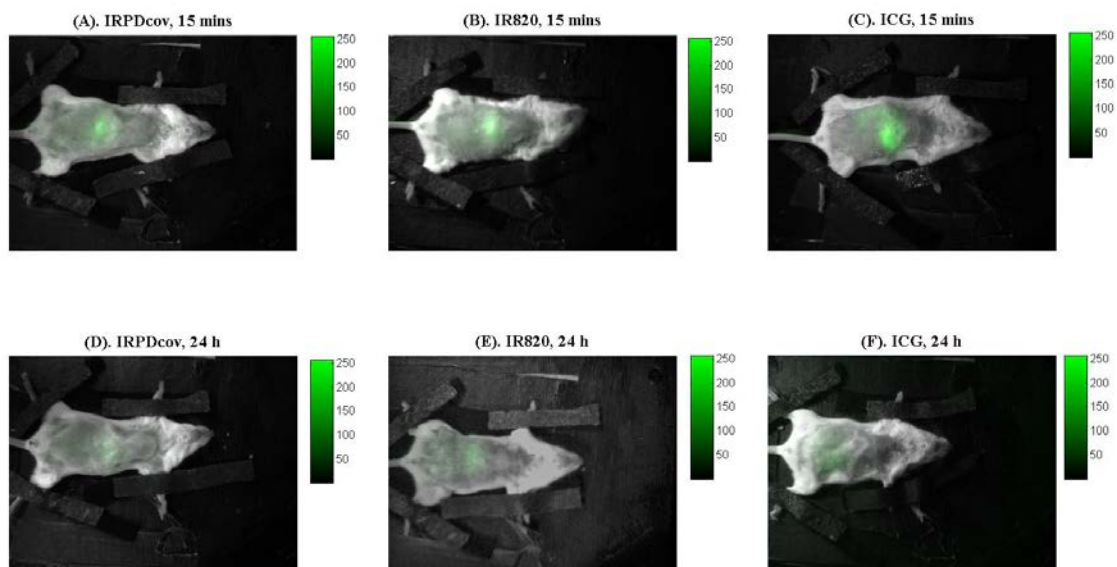


Figure 30. Images taken 15 minutes and 24 hours after i.v. injection for IRPDcov, IR820, and ICG.

These images prove that IRPDcov can be used for *in vivo* imaging and that it provides an imaging signal comparable to that of IR820. As expected based on our prior rat imaging experiments, the signal ratio for ICG at 15 minutes after injection was higher than that of IR820 or IRPDcov. However, in agreement with our previous data, by 24 hours the intensity of ICG had dropped significantly in comparison with the other two agents. The 24-hour ICG signal also seemed to be located in the lower abdomen, instead of in the liver region as is the case for the other two agents.

6.3.2. Organ imaging

Organ images obtained after 24 hours demonstrate a very different biodistribution for ICG compared to the other two agents. Figure 31 provides a qualitative comparison of organ signals for IRPDcov, IR820, and ICG, and Table 6 summarizes the organ signal

intensity per unit area ratios for each dye. The information obtained from the ratio data indicates that the biodistribution of IRPDcov, IR820, and ICG shows a different pattern between agents 24 hours after i.v. injection.

	Image intensity per area, R ($1/\mu\text{m}^2$)		
	IRPDcov	IR820	ICG
Liver	$6.35 \pm 0.44^{*(p<0.001)}$	$6.13 \pm 1.44^{*(p=0.002)}$	0.76 ± 0.35
Lungs $^{**}(p=0.003)$	$0.64 \pm 0.08^{*(p=0.04)}$	$2.48 \pm 0.47^{*(p=0.001)}$	0.18 ± 0.32
Kidneys	$1.34 \pm 0.13^{*(p=0.003)}$	$2.95 \pm 1.88^{*(p=0.04)}$	0.20 ± 0.34
Intestines	0.65 ± 0.10	1.00 ± 0.45	2.01 ± 1.43

Table 6. Signal intensity ratios for liver, lungs, kidneys and intestines collected 24 hours after i.v. injection of IRPDcov, IR820, or ICG. Values represent average \pm SD. * = Significant difference ($p<0.05$) with ICG values for the same organ; ** = Significant difference ($p<0.05$) between IRPDcov and IR820 values for the same organ.

Although an ICG signal was still present in the liver, the ratio was significantly lower ($p<0.05$) than for IR820 or IRPDcov. The amount of ICG present in the kidneys and the lungs was also significantly smaller ($p<0.05$) than for the other two agents. In the case of the intestines, a higher signal was observed for ICG than for IR820 or IRPDcov, however, the effect did not reach statistical significance due to large standard deviation for ICG measurements in the intestines. We expect that inter-subject variability in intestinal motility rates would affect ICG more markedly, given that most of the dye is being eliminated via the gastrointestinal tract at the 24-hour time point.

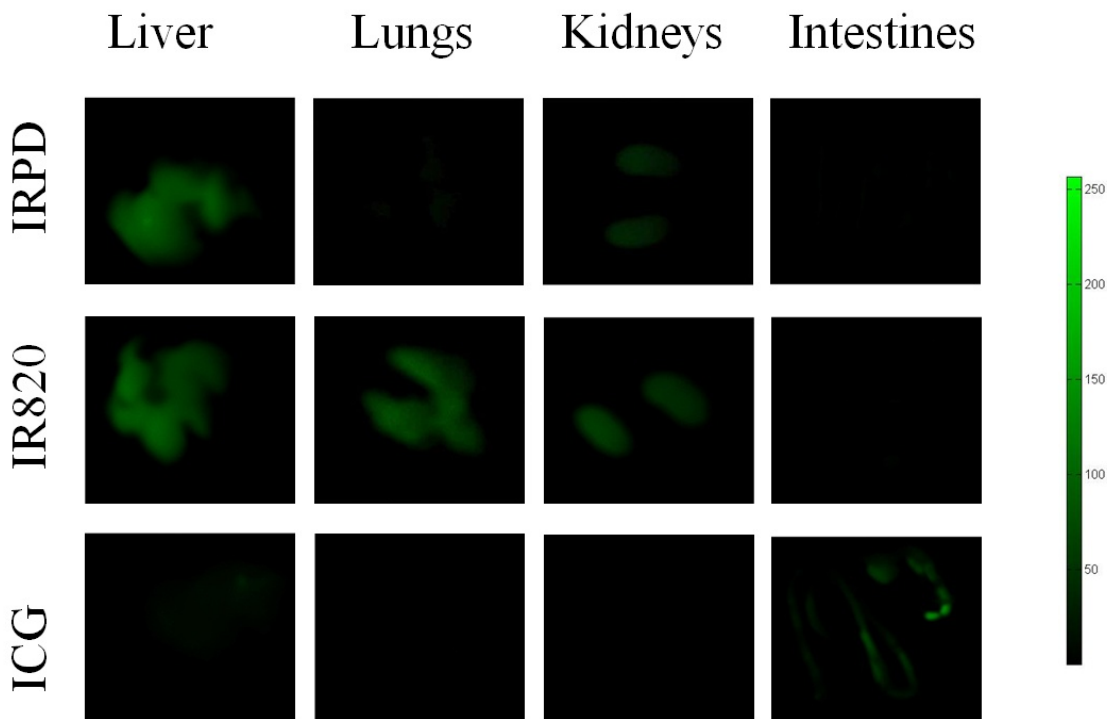


Figure 31. Organ images taken 24 hours after i.v. injection of IRPDcov, IR820, or ICG.

In the case of IR820, a strong signal was observed in the liver, kidneys, and lungs, with a small signal in the intestines. IRPDcov showed a strong signal in the liver, some signal in the kidneys, and a small signal in lungs and intestines. Statistical analysis comparing IR820 and IRPDcov showed that there were no differences in liver or intestinal image ratios. There was a significant difference ($p < 0.05$) in lung image ratios, with IRPDcov showing a smaller signal ratio than IR820. This possibly indicates that the nanoformulation was able to escape detection by alveolar macrophages thanks to the presence of PEG, which reduces binding to serum proteins (Li et al., 2008). In the kidneys, the IRPDcov signal was smaller than that of IR820, but the difference did not reach statistical significance. There may be a somewhat smaller degree of elimination of

IRPDcov through the kidneys, which would be consistent with the expectation that the larger size of the conjugate compared with the free dye would result in decreased renal clearance based on a low molecular size cutoff for renal excretion (Li et al., 2008), as well as the fact that the presence of PEG could result in reduced reticuloendothelial system uptake. However, the small number of subjects in our study may not provide enough sensitivity to detect a significant difference. Another reason for the lack of significance could be variability in renal elimination rates between subjects. Additionally, imaging ratios may not be sensitive enough to detect quantitative differences.

From these images we can conclude that there are clear differences in the biodistribution patterns of ICG versus IRPDcov and IR820, with ICG being more rapidly cleared from major organs than the other two agents, and primarily localizing in fecal elimination pathways by 24 hours. In terms of comparing IRPDcov with IR820, our lung images support the hypothesis of reduced mononuclear phagocyte system uptake (Li et al., 2008), which we can probably owe to the presence of PEG. Additionally, it is possible that further studies with larger numbers of subjects could also detect reduced localization to the kidneys.

6.3.3. Organ dye content

Table 7 shows the average dye content in $\mu\text{g dye/g}$ tissue for liver, lungs, kidneys and intestines 24 hours after an i.v. injection of IRPDcov, IR820, or ICG. The data is consistent with our qualitative observations and quantitative signal ratios from the optical imaging samples, and provides increased sensitivity to detect differences.

	Organ dye content ($\mu\text{g dye/g tissue}$)		
	IRPDcov	IR820	ICG
Liver	0.25 (4.1%) \pm 0.03*	0.21(3.6%) \pm 0.11*	0.01(0.6%) \pm 0.003
Lungs**	0.12(2.0%) \pm 0.02*	0.28(4.7%) \pm 0.03*	0 - Background signal
Kidneys	0.31(5.2%) \pm 0.10*	0.42(6.9%) \pm 0.11*	0 - Background signal
Intestines	0.03(0.5%) \pm 0.01*	0.05(0.8%) \pm 0.01*	0.07(1.2%) \pm 0.02

Table 7. Quantitative organ content 24 hours after after i.v. injection of IRPDcov, IR820, or ICG.

Values represent average \pm SD(%ID). * = Significant difference ($p < 0.05$) with ICG values for the same organ; ** = Significant difference ($p < 0.05$) between IRPDcov and IR820 values for the same organ

When we compare the results for ICG with those of IRPDcov and IR820, we see that organ content was significantly higher in the intestines, and significantly lower in all other organs. For lung and kidneys, ICG sample readings were at background level.

When comparing IRPDcov and IR820, the only significant difference was a reduced content of IRPDcov in the lungs. IRPDcov kidney content was lower than for IR820, but the difference was not significant. Thus, the interpretation presented in section 6.3.2. is supported by our quantitative analysis of organ dye content. Additionally, the difference between intestinal uptake of ICG, IRPDcov, and IR820 becomes significant once quantitative organ dye content was used as a measurement.

6.3.4. Plasma dye concentration

Table 8 shows the average dye concentration in plasma in $\mu\text{g/mL}$ for IRPDcov, IR820, and ICG at each of the time points under study. We observed significantly higher

($p < 0.05$) plasma concentrations of IR820 and IRPDcov compared to ICG for all time points, with plasma values 20 times higher at 24 hours for IRPDcov, and 10 times higher for IR820. We also found significantly higher ($p < 0.05$) concentrations of IRPDcov compared to IR820 at the 30-minute, 60-minute, and 24-hour time points, with plasma concentration of IRPDcov double that of IR820 at the 24-hour sampling time.

Time	Dye		
	IRPDcov	IR820	ICG
15 minutes	2.52±0.99 ^{*(p=0.008)}	1.94±1.17 ^{*(p=0.03)}	0.20±0.16
30 minutes ^{** (p=0.01)}	1.80±0.29 ^{*(p<0.001)}	0.97±0.15 ^{*(p<0.001)}	0.07±0.004
60 minutes ^{** (p<0.001)}	0.83±0.03 ^{*(p<0.001)}	0.34±0.03 ^{*(p<0.001)}	0.05±0.02
24 hours ^{** (p<0.001)}	0.20±0.02 ^{*(p<0.001)}	0.10±0.01 ^{*(p<0.001)}	0.01±0.003

Table 8. Plasma concentrations ($\mu\text{g/mL}$) of IRPDcov, IR820, and ICG at different time points after i.v. injection. Values represent average \pm SD. * = significant difference from ICG, $p < 0.05$; ** = significant difference between IRPDcov and IR820, $p < 0.05$.

Based on these results, not only were IR820 formulations superior to ICG as expected in terms of plasma concentration over time, but we also observed a clear advantage of the IRPDcov conjugate over IR820 after initial distribution. This confirms the applicability of the theoretical foundation that justified the formulation of this conjugate, which relied on the possibility that the presence of PEG could contribute to improved plasma concentration profiles by reducing detection by macrophages and other circulating agents in plasma. IRPDcov is thus analogous to other formulations where the inclusion of PEG

has provided some stealth characteristics in an *in vivo* environment. The differences observed between IR820 and IRPDcov are most likely due to differences in charge, size, and surface characteristics, which are discussed in section 6.2.5.

The recovered percent injected dose at 24 hours in plasma was 3.3% for IRPDcov, 1.7% for IR820, and 0.8% for ICG. If we add these numbers to the percent values of the recovered injected doses found in our organ content studies, we reach an overall percent of 15.1% for IRPDcov, 17.7% for IR820, and 2.6% for ICG.

In the case of ICG, almost the entire injected dose has been lost after 24 hours, which demonstrates a clear advantage of the IR820 formulations in terms of injected dose recovery at this time point. Surprisingly, we did not observe a larger percent dose recovery for IRPDcov compared to IR820. A possible explanation may be that, as the circulating concentration of IRPDcov is still double that of IR820 at 24 hours, it is possible that a considerable amount of the conjugate may yet be present in other non-sampled tissues, such as fat, skin, muscle, bone, or the lymphatic system.

6.3.5. Pharmacokinetic modeling

Figure 32 below shows a representative screenshot of the Matlab curvefit tool. All dyes were fit to both a monoexponential and a biexponential model, and goodness of fit was assessed by R^2 , RMSE, and calculated RMSPE. The latter two were calculated as previously described by comparing model predictions with experimental data.

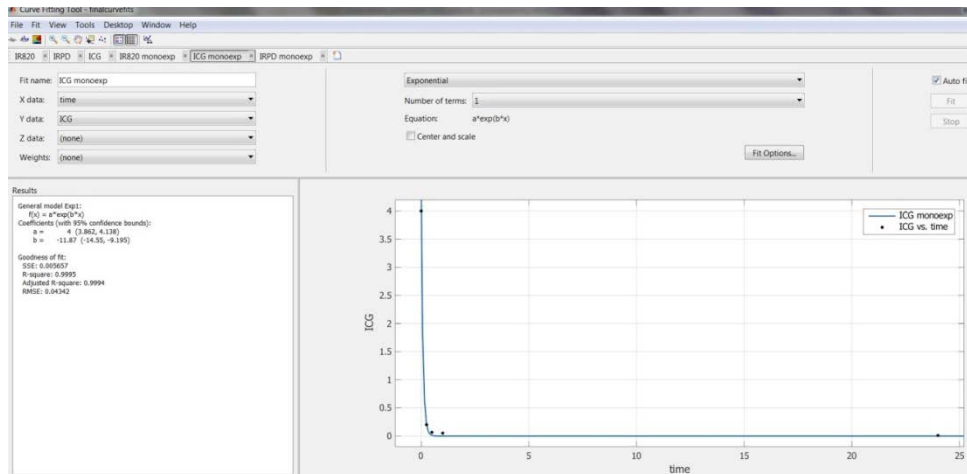


Figure 32. Sample curve fit for plasma concentration data using the curvefit tool in Matlab

Figure 33 shows the plasma pharmacokinetic profiles for IRPDcov, IR820, and ICG, in a graph created using Sigmaplot (Systat Software, San Jose, CA).

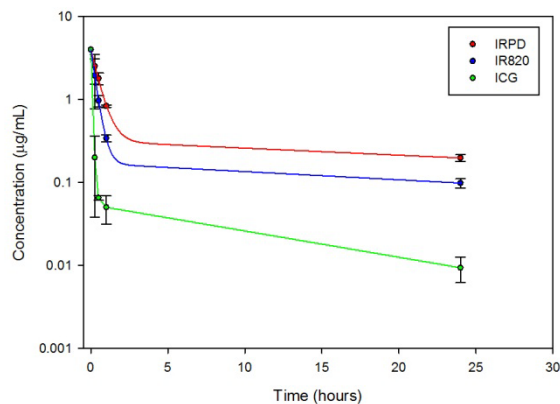


Figure 33. Pharmacokinetics of IRPDcov, IR820, and ICG plasma concentrations vs. time after i.v. dose.

a. One-compartment modeling

Table 9 shows the resulting parameters from a one-compartment modeling approach to IRPDcov, IR820, and ICG data, given the monoexponential equation:

$$C(t)=C_0 * e^{-kt}$$

	IRPDcov	IR820	ICG
Model equation	$C(t)=3.952 * e^{-1.619t}$	$C(t)=3.984 * e^{-2.805t}$	$C(t)=4 * e^{-11.87t}$
R ²	0.9912	0.9971	0.999
RMSE	0.1396	0.0848	0.0434
RMPSE	2.40%	2.00%	1.94%
Half-life (hours)	0.428±0.010 ^{†, ††}	0.247±0.005 ^{†, ††}	0.058±0.001
AUC [µg-h/mL]	2.441±0.059 ^{†, ††}	1.420±0.028 ^{†, ††}	0.340±0.007
Mean plasma residence time, t _p (h)	0.610±0.015 ^{†, ††}	0.355±0.007 ^{†, ††}	0.085±0.002
Total body clearance rate (ml/h)	2.46±0.06 ^{†, ††}	4.22±0.08 ^{†, ††}	17.6±0.34

Table 9. Pharmacokinetic parameters from one-compartment analysis of dye data in mice. † = significant difference (p<0.05) with ICG; †† = significant difference (p<0.05) between IRPDcov and IR820.

The monoexponential model provided a good fit to our data, with R² values over 0.99 for all dyes, and percent errors under 2.5%. According to this model, both IR820 and IRPDcov demonstrate significantly longer half-lives, larger AUC, longer t_p, and slower body clearance rates than ICG. All of these are signs of prolonged blood circulation (Li et al., 2008). Additionally, IRPDcov also showed a significant advantage over IR820 for all of these parameters, indicating that the nanoformulation resides longer in plasma and is eliminated from the body more slowly. However, it seems that the calculated clearance rates represent quite large volumes for a mouse, which leads us to question the physiological validity of the model.

b. Two-compartment modeling

Table 10 shows the resulting parameters from a two-compartment modeling approach to IRPDcov, IR820, and ICG data, given the biexponential equation:

$$C(t)=A * e^{-at} + B * e^{-bt}$$

	IRPDcov	IR820	ICG
Model equation based on plasma data	$C(t)=3.666*e^{-1.905t}+0.3162*e^{-0.01955t}$	$C(t)=3.831*e^{-3.108t}+0.1702*e^{-0.02275t}$	$C(t)=3.927*e^{-13.54t}+0.0734*e^{-0.3752t}$
R ²	0.9953	0.9999	0.9999
RMSE	0.1023	0.0120	0.0094
RMPSE	1.59%	1.49%	1.51%
Distribution half-life (h)	0.364±0.006 ^{†, ††}	0.223±0.003 ^{†, ††}	0.051±0.001
Elimination half-life (h)	35.46±0.56 ^{†, ††}	30.45±0.45 ^{†, ††}	1.85±0.03
AUC [µg-h/mL]	7.98±0.13 ^{†, ††}	4.38±0.07 ^{†, ††}	0.490±0.007
Mean residence time in plasma (h)	1.99±0.03 ^{†, ††}	1.09±0.02 ^{†, ††}	0.12±0.002
Total body clearance rate (ml/h)	0.75±0.01 ^{†, ††}	1.37±0.02 ^{†, ††}	12.25±0.18

Table 10. Pharmacokinetic parameters from two-compartment analysis of dye data in mice. † = significant difference (p<0.05) with ICG; †† = significant difference (p<0.05) between IRPDcov and IR820.

As can be seen in Table 10, the biexponential model modestly improved the fit for IRPDcov in terms of R² values compared to the monoexponential model, and did not improve the fit for IR820 and ICG, which was expected because the value of R² was already very good for both dyes in the monoexponential model. The percent errors inherent in the biexponential model are all 1.6% and lower, which is a reduction from the monoexponential model. Total body clearance rates seem more physiologically plausible.

Based on this, it seems that the biexponential model may provide a better understanding of our data. It can also provide us with separate insight into the distribution and elimination behavior of each agent, and allow further comparisons between formulations. According to this model, both IR820 and IRPDcov demonstrate significantly longer (p<0.05) distribution half-lives, longer elimination half-lives, larger AUC, longer plasma

residence times, and slower body clearance rates than ICG. Although distribution happens quite fast for all agents, ICG distribution half-life is approximately 3.06 minutes, whereas the value for IR820 is 13.4 minutes, and for IRPDcov 21.8 minutes. The value of distribution half-life for ICG is consistent with that previously reported by other authors, which ranges from 2 to 4 minutes (Desmettre et al., 2000; Mordon et al., 1998). The calculated elimination half-lives for IRPDcov and IR820, which both exceed 30 hours, is in stark contrast with that of ICG, which is 1.85 hours. These values are also well aligned with some of the conclusions reached by Prajapati's group, who determined that IR820 binds to albumin and should have a clearance half-life close to that of albumin, which is in the order of 35 hours (Prajapati et al., 2009). The elimination half-life value we obtained for ICG is consistent with literature data, as other authors report an elimination half-life of over 1 hour at low concentrations (Desmettre et al., 2000).

Both the distribution and the elimination phases show improved profiles for IR820 formulations compared to ICG in terms of providing a wider time window for theranostic action. As far as the area under the concentration-time curve, both IRPDcov and IR820 are an order of magnitude larger than ICG, indicating an increased overall exposure to the theranostic agent. Additionally, IRPDcov also shows a significant advantage ($p < 0.05$) over IR820 for all the above calculated parameters, with almost double the AUC and the mean plasma resident time of IR820, and almost half the clearance rate of IR820. The nanoformulation is present in plasma for longer periods of time, eliminated more slowly from the body, and the cumulative exposure of body compartments to the conjugate is larger than for any of the two free dyes. The time that the IRPDcov is bioavailable is also

significantly longer, as the elimination half-life of IRPDcov is 1.16 times longer than that of IR820, and 19 times longer than that of ICG; whereas the distribution half-life of IRPDcov is 1.6 times longer than that of IR820, and 7 times longer than that of ICG.

Given that the enhanced permeability and retention effect is proportional to the time and amount of agent circulating in blood (Saxena et al., 2006), we would theoretically expect IRPDcov to result in a greater amount of dye accumulated and retained in tumors. However, further studies in a tumor-bearing model would be needed to explore this possibility.

Other authors have studied the pharmacokinetics of nanoformulations and the general consensus is that nanoformulations may result in improved pharmacokinetic profiles, in many cases as a result of stabilization of the drug and reduced liver metabolism and renal clearance (Li et al., 2008). Still, loss of nanocomplexes from the circulation can occur by binding to serum proteins in the process known as surface opsonization, which subsequently causes recognition and removal by circulating phagocytes or macrophages (Albanese et al., 2012; Moghimi et al., 2012). In the case of PEGylated formulations, steric hindrance reduces the degree of protein binding, resulting in prolonged circulation times and giving PEGylated formulations an improved pharmacokinetic profile compared to their non-PEGylated counterparts (Albanese et al., 2012; Li et al., 2008). This seems to be applicable to formulations incorporating PEG as a conjugated moiety as is the case of the IRPDcov conjugate.

Another consideration which is intimately tied to these profiles is the surface charge of the formulation. Our nanoconjugates are zwitterionic, presenting both positive and negative charges and with an overall zeta potential that approaches neutrality. Other authors have found that, for other physical characteristics being similar, neutral and zwitterionic nanoformulations exhibit prolonged plasma half-lives and reduced clearance compared to largely positive or largely negative formulations, which indicates that charge may play a large role in maximizing circulation time (Arvizo et al., 2011).

Nanocomplex size also has an effect on circulation time, with particles around 100 nm diameter demonstrating longer blood circulation profiles than larger or smaller particle sizes (Li et al., 2008). Liu et al studied the effect of size on biodistribution of liposomes, and found that sizes between 100 and 200 nm were present in circulation for longer times than those greater than 250 nm or smaller than 50 nm (Liu et al., 1992). Given that our nanoconjugates are around 150 nm per SEM measurement, it seems that size is also contributing to their prolonged circulation times.

6.3.6. Limitations

Our analysis is not without possible limitations. First, the pharmacokinetic models we have used have important assumptions such as uniform distribution, no absorption, rapid equilibration before sampling, and no degradation. Uniform distribution may be an issue, as we know that nanoformulations are distributed to tissues depending on pore size, in a different manner than their free form counterparts (Cho et al., 2008; Dhanikula et al., 2005; Li et al., 2008). Regarding absorption, both the monoexponential and biexponential

models were good fits for our data and they both ignore absorption, thus we are quite confident that absorption is negligible enough to not impact our interpretation of the data. In terms of rapid equilibration, others have reported that equilibration of injected solutions in mice plasma can be assumed to happen within 2 minutes (Berezhkovskiy, 2009). Since our first sample was taken at 15 minutes, we can assume that equilibration has occurred by that time, and we do not expect this assumption to be broken. Regarding the possibility of degradation into other byproducts, other authors have shown that ICG is mostly excreted in its intact form in bile (Achilefu et al., 2000; Saxena et al., 2006). Our *in vitro* studies show that IRPDcov conjugates are very stable and retain their characteristics for at least 72 hours in phosphate buffered saline. Based on this, we do not expect degradation to be a significant concern within the time periods studied *in vivo*. However, the *in vivo* environment cannot be fully mimicked by *in vitro* conditions, and some *in vivo* factors such as the presence of plasma proteins, reticuloendothelial system scavengers, and metabolism in liver or other tissues may result in aggregation, degradation, or changes in the structure of these molecules.

A final consideration in terms of calculated pharmacokinetic parameters is the recent discussion regarding classical estimates of plasma residence time versus newer estimates that adjust for drug or agent elimination during the initial distribution period. Berezhvosky has proposed a revised plasma residence time equation that takes into consideration the time that it takes to reach a uniform plasma distribution (Berezhkovskiy, 2009). When we repeated our calculations using his equation, the values of plasma residence time for IRPDcov, IR820, and ICG were all within 0.02 hours of the

values we calculated using classical equations. Thus, although the revised equation may be useful for agents that have initial extremely rapid elimination profiles, we are confident that this is not a significant issue in the case of IRPDcov, IR820, or ICG, and we have chosen to report the classically calculated values of plasma residence time as a function of AUC and initial estimate of concentration. Moreover, the fact that our values barely changed using either of the two calculation approaches also provides some confidence that our assumed initial concentration in plasma is likely to be reasonably accurate.

There are other concerns besides those arising from the models we used to approximate the *in vivo* pharmacokinetics of these agents. An important one may be the fact that we used parallel sampling, in which each data point is an isolated animal, rather than serial sampling, where samples are taken from the same animal over time. Although serial sampling has the advantage of reducing inter-subject variability in the concentration vs. time curves, it also puts the subjects at risk due to repeated blood sampling based on the procedure itself as well as the cumulative amount of blood lost that could lead to hypovolemic shock (Wolfensohn et al., 2003). Blood collection by heart puncture is best considered a terminal collection method (Hoff, 2000), and the alternative which is typically tail blood collection may not give us correct information as there is the potential for residual dye contamination of the tail. The fact that we achieved good model fits using parallel sampling seems to indicate that no large inter-subject variations were introduced by the method we used.

Another concern is the inability to flush the tail due to injection volume limitations. Other authors have reported that a large amount of sample can be left in the tail vein (Yaseen et al., 2009), which complicates the interpretation of the pharmacokinetic analysis by assuming an initial concentration in plasma that is not an accurate representation of the percentage dose that reached the central compartment. Goodness of the model fit seems to provide reassurance that this was not a significant concern in our studies.

Additionally, when considering our organ localization analysis based on imaging and quantitative content data, the applicability of our conclusions is limited by the fact that we only collected organs at the 24-hour data point. However, based on the results showing that IR820 and IRPDcov have much slower distribution and elimination profiles than ICG, we would not expect that additional data collected in the range of one hour after injection would reveal any further information than that provided to us by the 24-hour time point. This time point allows us to clearly highlight the differences between agents, and provides us with information within a clinically relevant theranostic window. The same could be said for our plasma data and the selection of four time points in terms of whether there are sufficiently representative. Although of course obtaining as many samples for as many time points as possible is always desirable, one of the central tenets of science is the ability to prioritize while designing an experiment. Our goal should be to design an experiment that allows us to obtain the most relevant pieces of information, i.e., those which will help us answer our starting questions. We are confident that the data we have collected provides a good insight into the behavior of these agents in an *in vivo* model.

6.4. Summary

Biodistribution and pharmacokinetic studies of IRPDcov, IR820, and ICG in mice show that IRPDcov is a feasible alternative to IR820 for *in vivo* imaging, and that it demonstrates an improved pharmacokinetic profile over the free dye form as well as over the commonly used near-infrared dye ICG. The IRPDcov conjugate has different organ localization than free IR820, with potential reduced accumulation in the kidneys and significantly lower ($p < 0.05$) accumulation in the lungs. Both IRPDcov and IR820 had entered fecal elimination pathways to a lesser extent than ICG after 24 hours, with larger overall recovered percent injected dose from major organs and plasma compared to ICG. Plasma IRPDcov concentration was significantly higher than that of IR820 for time points after the initial 15 minutes post-injection, and both IR820 formulations (conjugate and free form) showed higher plasma concentrations than ICG at all sampling points after injection. When plasma concentration was modeled using a two-compartment approach, the conjugate demonstrated a biphasic profile with significantly longer distribution and elimination half-lives, longer mean plasma residence time, larger overall exposure as indicated by AUC, and slower clearance rate compared to either IR820 or ICG. The nanosize nature of our conjugate, as well as surface and charge characteristics provided by the presence of PEG, is likely to be responsible for these differences. The use of IRPDcov conjugates could provide wider dye *in vivo* availability windows for theranostic applications.

Chapter 6 References

- Achilefu, S. and R. B. Dorshow (2002). *Dynamic and Continuous Monitoring of Renal and Hepatic Functions with Exogenous Markers*, Springer.
- Achilefu, S., R. B. Dorshow, et al. (2000). Novel receptor-targeted fluorescent contrast agents for in vivo tumor imaging. *Invest Radiol* **35**(8): 479-485.
- Albanese, A., P. S. Tang, et al. (2012). The effect of nanoparticle size, shape, and surface chemistry on biological systems. *Annu Rev Biomed Eng* **14**: 1-16.
- Arvizo, R. R., O. R. Miranda, et al. (2011). Modulating pharmacokinetics, tumor uptake and biodistribution by engineered nanoparticles. *PLoS One* **6**(9): e24374.
- Bauer, L. (2008). *Applied Clinical Pharmacokinetics*. New York, NY, McGraw Hill.
- Berezhkovskiy, L. M. (2009). Determination of mean residence time of drug in plasma and the influence of the initial drug elimination and distribution on the calculation of pharmacokinetic parameters. *J Pharm Sci* **98**(2): 748-762.
- Cho, K., X. Wang, et al. (2008). Therapeutic nanoparticles for drug delivery in cancer. *Clin Cancer Res* **14**(5): 1310-1316.
- de Chermont, Q. L., C. Chaneac, et al. (2007). Nanoprobes with near-infrared persistent luminescence for in vivo imaging. *Proc. Natl. Acad. Sci. U. S. A.* **104**(22): 9266-9271.
- Desmettre, T., J. M. Devoisselle, et al. (2000). Fluorescence properties and metabolic features of indocyanine green (ICG) as related to angiography. *Surv Ophthalmol* **45**(1): 15-27.
- Dhanikula, A. B., D. R. Singh, et al. (2005). In vivo pharmacokinetic and tissue distribution studies in mice of alternative formulations for local and systemic delivery of Paclitaxel: gel, film, prodrug, liposomes and micelles. *Curr Drug Deliv* **2**(1): 35-44.
- European Commission, Research & Innovation - Health Department. (2010). *Of Mice and Men – Are Mice Relevant Models for Human Disease?* London, UK. Available at: http://ec.europa.eu/research/health/pdf/summary-report-25082010_en.pdf. Accessed September 24, 2012.
- Fournier, R. L. (2007). *Basic Transport Phenomena in Biomedical Engineering*. New York, NY, Taylor & Francis.
- Hoff, J. (2000). Methods of blood collection in the mouse. *Lab Animal* **29**(10): 47-53.

- Li, S. D. and L. Huang (2008). Pharmacokinetics and biodistribution of nanoparticles. *Mol Pharm* **5**(4): 496-504.
- Liu, D., A. Mori, et al. (1992). Role of liposome size and RES blockade in controlling biodistribution and tumor uptake of GM1-containing liposomes. *Biochim Biophys Acta* **1104**(1): 95-101.
- Macon, M. B., L. R. Villanueva, et al. (2011). Prenatal perfluorooctanoic acid exposure in CD-1 mice: low-dose developmental effects and internal dosimetry. *Toxicol Sci* **122**(1): 134-145.
- Moghimi, S. M., A. C. Hunter, et al. (2012). Factors controlling nanoparticle pharmacokinetics: an integrated analysis and perspective. *Annu Rev Pharmacol Toxicol* **52**: 481-503.
- Mordon, S., J. M. Devoisselle, et al. (1998). Indocyanine green: physicochemical factors affecting its fluorescence in vivo. *Microvasc Res* **55**(2): 146-152.
- Prajapati, S. I., C. O. Martinez, et al. (2009). Near-infrared imaging of injured tissue in living subjects using IR-820. *Mol Imaging* **8**(1): 45-54.
- Rajagopalan, R., P. Uetrecht, et al. (2000). Stabilization of the optical tracer agent indocyanine green using noncovalent interactions. *Photochem Photobiol* **71**(3): 347-350.
- Saxena, V., M. Sadoqi, et al. (2006). Polymeric nanoparticulate delivery system for Indocyanine green: biodistribution in healthy mice. *Int J Pharm* **308**(1-2): 200-204.
- Truskey, G. A., F. Yuan, et al. (2009). *Transport Phenomena in Biological Systems*. Upper Saddle River, NJ, Pearson Prentice Hall.
- van Vlerken, L. E., T. K. Vyas, et al. (2007). Poly(ethylene glycol)-modified nanocarriers for tumor-targeted and intracellular delivery. *Pharm Res* **24**(8): 1405-1414.
- Wolfensohn, S. and M. Lloyd (2003). *Handbook of Laboratory Animal Management and Welfare*. Oxford, UK, Wiley-Blackwell.
- Yaseen, M. A., J. Yu, et al. (2009). Biodistribution of encapsulated indocyanine green in healthy mice. *Mol Pharm* **6**(5): 1321-1332.
- Zuegge, J., G. Schneider, et al. (2001). Prediction of hepatic metabolic clearance: comparison and assessment of prediction models. *Clin Pharmacokinet* **40**(7): 553-563.

CHAPTER 7: OVERALL DISCUSSION AND CONCLUSIONS

The development of multifunctional agents for cancer management is a rapidly growing field which can result in improved diagnosis and therapy for patients with cancer. Recent developments in nanotechnology have fueled the growth of theranostics research, because nanoformulations have unique characteristics that make them well-suited to customized therapy approaches and multimodal applications. Nanosize therapeutic and diagnostic agents can be tailored to a specific application by manipulating their size, shape, surface characteristics, and other physiochemical properties, resulting in personalized strategies to treat disease. This frame of thought involves the customization of diagnostic and therapeutic approaches to a specific disease process, and is especially relevant in disorders such as cancer, which is very heterogeneous and encompasses a large spectrum of alterations in cellular processes and behavior. Customizable medicine, along with the combination of diagnostic and therapeutic approaches to improve management such as the ability to use imaging to guide therapy, opens the door to a new era in patient care.

Near-infrared dyes can be used as theranostic agents in cancer management based on their optical imaging and localized hyperthermia capabilities, however, they have important limitations which limit their applicability for theranostic use, especially in terms of photobleaching, *in vivo* instability and non-specific biodistribution (Frangioni, 2003). Another concern based on these disadvantages is the ability to provide convenient timing for combined imaging and therapy. In our work, we studied the properties of the

cyanine dye IR820, and provided the first detailed report of its potential for use in theranostics. We studied the applications of IR820 in optical imaging and hyperthermia, and we prepared nanoconjugate formulations that retain or improve upon these theranostic capabilities.

We chose to study the cyanine dye IR820 because of its chemical structure. IR820 is structurally similar to indocyanine green (ICG), which is a clinically approved cyanine dye. ICG can be used in imaging and hyperthermia applications, so we expected IR820 to have similar multi-functionality. On the other hand, we hypothesized that the presence of a chlorohexene ring in IR820 which is absent in ICG could mean that IR820 would have improved stability as well as more amenability to conjugation. Our results showed that IR820 has optical and thermal generation properties similar to indocyanine green, but with improved *in vitro* and *in vivo* stability. The fluorescent emission of IR820 has a lower quantum yield than ICG, but less dependence of the emission peak location on concentration. This predictability of peak location for IR-820 could facilitate the design of imaging systems targeting IR-820 emission wavelengths. Additionally, IR820 demonstrated higher stability than ICG in aqueous solution under all temperature and light conditions, with degradation half-times approximately double those of ICG for a given experimental condition. IR820 is still susceptible to photobleaching, but less so than ICG. In hyperthermia applications, IR820 generated lower peak temperatures than ICG (4-9%) after three-minute laser exposure. However, it was still able to cause temperature increases into the desired hyperthermia range of 40-43°C that is able to selectively impact tumor cell growth. There was no significant difference in hyperthermia

cytotoxicity between IR820 and ICG, with both dyes causing cancer cell growth inhibition at 5 μ M and cell killing at 10 μ M upon laser exposure. Free IR820 can be used for *in vitro* and *in vivo* optical imaging, with a strong detectable signal still present in rats 24 hours after i.v. injection, a plasma half-life in the order of hours, and primary biodistribution to the liver, lung, and kidneys. Our study shows that IR820 is a feasible agent in experimental models of imaging and hyperthermia, and could be an alternative to ICG when greater stability, longer image collection times, or more predictable peak locations are desirable.

Even though IR820 is a promising theranostic agent, clinical translation of NIR-imaging and hyperthermia approaches in cancer must overcome the challenges presented by free dye formulations in terms of plasma circulation times and non-specific biodistribution. Nanotechnology provides some opportunities to improve *in vivo* stability and target delivery. Physicochemical characteristics of nanoformulations such as size, surface charge, and surface characteristics can be modified to alter their interactions with circulating immune system components and with cellular membranes. In terms of the behavior of nanoformulations *in vivo*, it has been shown that nanosize agents are less susceptible to reticuloendothelial system clearance and have better penetration into tissues and cells than larger size agents (Brigger et al., 2002; Xu et al., 2006). Nanoformulations can also take advantage of the enhanced permeability and retention (EPR) effect thanks to their size, and thus are inherently able to accumulate preferentially at tumor sites through passive targeting (Iyer et al., 2006).

We chose to conjugate IR820 with polyethylene glycol (PEG) to create a nanoformulation with additional desirable properties in terms of *in vivo* behavior, besides the advantages imparted by its nano nature. Research has shown that the presence of PEG in nanoformulations can reduce capture by the immune system, and result in improved plasma circulation times (Harris et al., 2001). Longer exposure to the theranostic agent provides a wider window of opportunity for diagnosis and therapy, and allows more flexibility in terms of timing, one with respect to the other, as needed for a specific application. Additionally, PEG can be used as a linker to conjugate other moieties and impart new functionality such as specific targeting.

The first step in exploring the potential of an IR820/PEG nanoconjugate for theranostic applications was to create ionic conjugates and determine if the optical and thermal generation properties of IR280 were preserved as part of a conjugate lattice. We successfully prepared ionic IR820-PEG-diamine nanoconjugates (IRP820-DNCs) which were approximately 50 nm diameter in SEM images, and had a zeta potential of 2.0 ± 0.9 mV. IRPDNCs showed enhanced cellular internalization in SKOV-3, MES-SA, and Dx5 cells for imaging purposes compared to the free dye, possibly due to osmotic stress on cellular membranes induced by the proximity of PEG. Cytotoxicity studies in SKOV-3, MES-SA and Dx5 cancer cell lines showed comparable cytotoxicity of IR820-PDNCs versus free IR820 after 24 hours. IR820-PDNCs were able to produce hyperthermic cell growth inhibition in all three cancer cell lines after excitation with laser, and they significantly enhanced hyperthermia-mediated cytotoxicity in MES-SA and Dx5 compared to hyperthermia using free dye. We concluded that this formulation can

potentially provide an advantage over the use of free agents by enhancing cell uptake, allowing simultaneous co-localization of imaging and therapy, and accentuating the cytotoxic effect of hyperthermia.

After proving that IR820 retained its ability to generate heat and fluoresce when interacting in close proximity with PEG as part of an ionic formulation, we hypothesized that modifying this formulation to create covalent conjugates could improve on the stability of the lattice and result in nanosize conjugates that may be used in *in vivo* applications with improved pharmacokinetic profiles compared to the free dye. Thus, we prepared and characterized covalent conjugates of IR820 and PEG-diamine (IRPDcov).

IRPDcov retained the ability to fluoresce after 785-nm excitation and to be used for *in vitro* optical imaging of cancer cells as well as *in vivo* imaging. *In vitro* cellular internalization was not as large as for ionic conjugates, but it was still larger than for free dye. IRPDcov also retained the heat-generation ability of IR820 upon exposure to 808-nm laser, and was significantly more stable than IR820 in aqueous solution over a period of 72 hours. In mouse plasma samples, IRPDcov and IR820 when compared to ICG demonstrated significantly longer ($p < 0.05$) distribution half-lives, elimination half-lives, and area-under-the-curve values. For IRPDcov, the area under the kinetic curve was almost 16 times larger than that of ICG, and approximately double that of IR820, indicating significantly longer overall exposure to the probe. This could pose an advantage in therapeutic probe applications such as hyperthermia or drug delivery. Regarding organ biodistribution, both IR820 and IRPD showed a very strong signal in the liver and lower-intensity signal in the kidneys 24 hours after i.v. injection, whereas the

predominant signal for ICG was weak and located in the intestines, demonstrating a much more rapid GI elimination. IRPDcov was different from IR820 in that the latter showed a signal in the lungs, which was not present in IRPDcov subjects. This indicates that IRPDcov may have been able to escape detection by alveolar macrophages. Our results are consistent with existing literature reports of increased half-life and decreased immune system uptake for PEGylated nanoformulations (Albanese et al., 2012; Arvizo et al., 2011; Brigger et al., 2002). We concluded that IRPDcov conjugates have potential applications as dual imaging-hyperthermia agents, are more stable in aqueous solution than IR820, can enhance the effect of hyperthermia in MES-SA and Dx5 cells, improve cell uptake with respect to free dye, and can provide improved theranostic windows *in vivo*.

The conjugation of PEG-diamine with a NIR dye provides a multifunctional delivery vector whose localization can be monitored with noninvasive techniques and that may also serve for guided hyperthermia cancer treatments. Future work should focus on studying the biodistribution of these conjugates in tumor-bearing animals in order to determine *in vivo* tumor uptake, as well as on the design and optimization of minimally invasive *in vivo* methods for combined imaging and hyperthermia, possibly through fiber optic technology. Additionally, there may be opportunities for active targeting of these conjugates. Terminal functional groups in PEG may be conjugated via amide bonding or bisulfide bridges with proteins, peptides, aptamers, and other small moieties for active targeting (van Vlerken et al., 2007). Functionalization can create specific interactions with cell surface receptors and result in enhanced uptake at sites of interest, with the

subsequent potential for customization of cancer therapies. Finally, it may also be possible to incorporate other therapeutic agents, such as chemotherapy drugs during nanoconjugate formulation in order to encapsulate them within the nanoplexes. This would result in a versatile multifunctional agent providing imaging, chemotherapy, and hyperthermia capabilities. Image-guided therapy using IR820 conjugates shows promise for clinical translation as it can be coupled with minimally invasive light delivery techniques such as endoscopic or orthoscopic approaches.

We believe that there are many unexplored possibilities for customizable IR820 conjugates besides the ones discussed in this dissertation which focused on PEG-containing conjugates. Researchers are actively pursuing the use of IR820 in different applications, including the use of IR820 as a blood pool contrast agent, the preparation of conjugates of IR820 with photodynamic therapy agents, and the incorporation of IR820 into multifunctional nanoparticles (Pandey et al., 2008; Prajapati et al., 2009; Thierry et al., 2009). Our group also continues to explore possible theranostic applications of IR820. For instance, one of our formulations covalently coupled IR820 with chitosan to form IR820-chitosan conjugates that also enhanced hyperthermic cell growth inhibition in MES-SA and Dx5 cells after 808-nm laser exposure, and can be used for *in vitro* and *in vivo* imaging. In a rat model, IR820-chitosan conjugates were eliminated through the gastrointestinal tract, with potential applications as contrast agents and gene delivery vehicles passively targeted to the digestive system. These results highlight the possibility of developing IR820 conjugates for different applications based on the identity of the

linker or conjugated moiety, thus creating opportunities for customizable theranostic agents and furthering the vision of personalized medicine.

Chapter 7 references

- Albanese, A., P. S. Tang, et al. (2012). The effect of nanoparticle size, shape, and surface chemistry on biological systems. *Annu Rev Biomed Eng* **14**: 1-16.
- Arvizo, R. R., O. R. Miranda, et al. (2011). Modulating pharmacokinetics, tumor uptake and biodistribution by engineered nanoparticles. *PLoS One* **6**(9): e24374.
- Brigger, I., C. Dubernet, et al. (2002). Nanoparticles in cancer therapy and diagnosis. *Adv. Drug Delivery Rev.* **54**(5): 631-651.
- Frangioni, J. V. (2003). In vivo near-infrared fluorescence imaging. *Curr. Opin. Chem. Biol.* **7**(5): 626-634.
- Harris, J. M., N. E. Martin, et al. (2001). Pegylation: a novel process for modifying pharmacokinetics. *Clin. Pharmacokinet.* **40**(7): 539-551.
- Iyer, A. K., G. Khaled, et al. (2006). Exploiting the enhanced permeability and retention effect for tumor targeting. *Drug Discov Today* **11**(17-18): 812-818.
- Pandey, R. K., N. James, et al. (2008). Cyanine-based compounds for tumor imaging with and without photodynamic therapy. *Top Heterocycl Chem* **14**: 41-74.
- Prajapati, S. I., C. O. Martinez, et al. (2009). Near-infrared imaging of injured tissue in living subjects using IR-820. *Mol Imaging* **8**(1): 45-54.
- Thierry, B., F. Al-Ejeh, et al. (2009). Multifunctional core-shell magnetic cisplatin nanocarriers. *Chem Commun (Camb)*(47): 7348-7350.
- van Vlerken, L. E., T. K. Vyas, et al. (2007). Poly(ethylene glycol)-modified nanocarriers for tumor-targeted and intracellular delivery. *Pharm Res* **24**(8): 1405-1414.
- Xu, Z. P., Q. H. Zeng, et al. (2006). Inorganic nanoparticles as carriers for efficient cellular delivery. *Chem. Eng. Sci.* **61**(3): 1027-1040.

APPENDICES

APPENDIX I. PERMISSION FROM AMERICAN SCIENTIFIC PUBLISHERS

11/25/12

Gmail - Permission Granted



Alicia Fernandez-Fernandez <joseyali@gmail.com>

Permission Granted

Dr. H. S. Nalwa <nalwa@mindspring.com>

Tue, May 29, 2012 at 9:11 PM

To: joseyali@gmail.com

Cc: omathanu.perumal@sdstate.edu

Dear Alicia Fernandez-Fernandez:

American Scientific Publishers grants permission to use the following article in your PhD thesis to be submitted to the Florida International University.

Romila Manchanda, Alicia Fernandez-Fernandez, Denny A. Carvajal, Tingjun Lei, Yuan Tang, and Anthony J. McGoron Nanoplexes for Cell Imaging and Hyperthermia: In Vitro Studies , J. Biomed. Nanotechnol. 8, 686-694 (2012)

H. S. Nalwa, PhD

AMERICAN SCIENTIFIC PUBLISHERS

www.aspbs.com

-----Original Message-----

From: Perumal, Omathanu [mailto:Omathanu.Perumal@sdstate.edu]

Sent: Tuesday, May 29, 2012 4:17 PM

To: Dr. H. S. Nalwa (nalwa@mindspring.com)

Subject: FW: Use of JBN manuscript in dissertation

Dr. Nalwa,

Can you pls respond to the request below

Thanks

[https://mail.google.com/mail/u/0/?ui=2&ik=983e688abf&view=pt&q=COPYRIGHT DISSERTATION&qs=tru...](https://mail.google.com/mail/u/0/?ui=2&ik=983e688abf&view=pt&q=COPYRIGHT%20DISSERTATION&qs=tru...)

1/3

11/25/12

Om

Omathanu Perumal, PhD
Editor-In-Chief- Journal of Biomedical Nanotechnology
www.aspbs.com/jbn
2010 Impact Factor- 2.63

Associate Professor
Department of Pharmaceutical Sciences
South Dakota State University
Brookings, SD-57007
Ph: 605-688-4745; Fax:605-688-5993
Email: omathanu.perumal@sdstate.edu

-----Original Message-----

From: joseyali@gmail.com [mailto:joseyali@gmail.com] On Behalf Of Alicia Fernandez-Fernandez

Sent: Tuesday, May 29, 2012 3:13 PM

To: Perumal, Omathanu

Subject: Use of JBN manuscript in dissertation

Hello,

I am a co-author of a manuscript accepted for publication in Journal of Biomedical Nanotechnology.

Nanoplexes for Cell Imaging and Hyperthermia: In Vitro Studies Romila Manchanda, Alicia Fernandez-Fernandez, Denny A. Carvajal, Tingjun Lei, Yuan Tang, and Anthony J. McGoron J. Biomed. Nanotechnol. 8, 686-694 (2012)

<https://mail.google.com/mail/u/0/?ui=2&ik=983e688abf&view=pt&q=COPYRIGHT DISSERTATION&qs=tru...>

2/3

The work in the manuscript was completed as part of my PhD dissertation. I am now writing my dissertation manuscript in preparation for graduation, and I am wondering what steps I need to take in order to use my work in my dissertation write up without infringing on our copyright transfer to the journal. Common sense tells me that using the material for a dissertation is probably okay, but I figured it was best to ask first. Are there any forms I need to fill in in order to get a permission letter from the publisher or the editors?

Thanks for the information, I'm really sorry if you're not the correct person to contact about this.

--

Alicia Fernandez-Fernandez, DPT
PhD candidate, Biomedical Engineering
Florida International University
Alpha Eta Mu Beta National Treasurer
(305) 609 6852
afern042@fiu.edu

APPENDIX II. PERMISSION FROM DECKER PUBLISHING



69 John Street South, Suite 310
Hamilton, Ontario L8N 3K7 Canada
1.905.522.8526 Fax 1.905.522.9273

55-B Jinnah Avenue, Blue Area, Suite 509
Islamabad Stock Exchange Building
Islamabad -44000 Pakistan

customercare@deckerpublishing.com
www.deckerpublishing.com
www.acpmedicine.com
www.acsurgery.com

November 27, 2012

Dear Alicia:

Permission is granted for you to use the following article in your PhD dissertation to be submitted to Florida International University.

Fernandez-Fernandez, A., R. Manchanda, et al. (2012). Comparative study of the optical and heat generation properties of IR820 and indocyanine green. *Mol Imaging* **11**(2): 99-113

Sincerely,

Paula Mucci
Journals Manager
Decker Publishing

VITA

ALICIA FERNANDEZ-FERNANDEZ

Born, Asturias, Spain

- 1994-1997 Diploma in Physical Therapy
Universidad de Oviedo
Oviedo, Spain
- 2000-2001 B.S., Health Sciences
Florida International University
Miami, Florida
- 2001-2002 M.S., Physical Therapy
Florida International University
Miami, Florida
- 2003-2007 B.S., Biomedical Engineering
Florida International University
Miami, Florida
- 2006-2010 Doctor of Physical Therapy
Nova Southeastern University
Fort Lauderdale, Florida
- 2007-2013 Doctoral Candidate, Biomedical Engineering
Florida International University
Miami, Florida
- 2011-present Assistant Professor, Physical Therapy Department
Nova Southeastern University
Fort Lauderdale, Florida

PUBLICATIONS AND PRESENTATIONS (ABRIDGED LIST)

Fernandez-Fernandez, A., R. Manchanda, D.A. Carvajal, T. Lei, and A.J. McGoron. Covalent IR820-PEG diamine conjugates: Characterization and in vivo biodistribution. *Proceedings of SPIE BiOS 2013*, in press.

Fernandez-Fernandez, A., R. Manchanda, T. Lei, Y. Tang, S.Z. Raza Kazmi, and A.J. McGoron. Comparative study of optical and heat generation properties of IR820 and indocyanine green. *Molecular Imaging*. 2012 Apr 1;11(2):99-113. PubMed ID: 22469238

Fernandez-Fernandez, A., R. Manchanda, and A.J. McGoron. Theranostic applications of nanomaterials in cancer: Image-guided therapy and multifunctional platforms. *Applied Biochemistry and Biotechnology*. 2011; 165(7-8):1628-51. PubMed ID: 21947761.

Fernandez-Fernandez A, R. Manchanda, T. Lei, and A.J. McGoron. Preparation and Characterization of Covalent IR820-PEG Diamine Conjugates. BMES 2012, October 24-27, Atlanta, GA. Poster presentation.

Fernandez-Fernandez, A., R. Manchanda, T. Lei, S. Srinivasan, and A.J. McGoron. Covalent IR820-PEG diamine nanoconjugate for imaging and hyperthermia. NanoFlorida 2012, September 28-29, Tampa, FL. Oral presentation. Received presentation award.

Fernandez-Fernandez, A., R. Manchanda, S. Srinivasan, T. Lei, D. Carvajal, and A.J. McGoron. IR820-chitosan conjugates for imaging and hyperthermia. SNM 2012, June 9-13, Miami, FL. Proceedings citation: J Nucl Med. 2012; 53 (Suppl. 1):1172

Fernandez-Fernandez, A., R. Manchanda, T. Lei, S. Srinivasan, and A.J. McGoron. IR820 Conjugates for Image-Guided Cancer Therapy. World Congress on Medical Physics and Biomedical Engineering, Beijing, China. May 26-31, 2012. IFMBE proceedings, volume 39, in press, ISBN 978-3-642-29304-7. Presented by AJM.

Lei, T., S. Srinivasan, Y. Tang, R. Manchanda, A. Nagesetti, A. Fernandez-Fernandez, and A.J. McGoron. Comparing cellular uptake and cytotoxicity of targeted drug carriers in cancer cell lines with different drug resistance mechanisms. *Nanomedicine:NBM*. 2011;7(3):324-332. PubMed ID: 21094277.

Manchanda, R., A. Fernandez-Fernandez, D.A. Carvajal, T. Lei, Y. Tang, and A.J. McGoron. Nanoplexes for cell imaging and hyperthermia: in vitro studies. *J Biomed Nanotechnol*. 2012, 8(4):686-694. PubMed ID: 22852478

Manchanda, R., A. Fernandez-Fernandez, A. Nagesetti, and A.J. McGoron. Preparation and characterization of a polymeric (PLGA) nanoparticulate drug delivery system with simultaneous incorporation of chemotherapeutic and thermo-optical agents. *J Colloids Surf B Biointerfaces*. 2010;75(1):260-7. Pubmed ID: 19775872.

Srinivasan, S., R. Manchanda, A. Fernandez-Fernandez, T. Lei, A.J. McGoron. Near-infrared fluorescing IR820-chitosan conjugate for multifunctional cancer theranostic applications. *J Photochem Photobiol B*, in press.

Tang, Y., T. Lei, R. Manchanda, A. Nagesetti, A. Fernandez-Fernandez, and A.J. McGoron. Simultaneous delivery of chemotherapeutic and thermal-optical agents to cancer cells by a polymeric (PLGA) nanocarrier: an in vitro study. *Pharm Res*. 2010; 27(10):2242-2253. PubMed ID: 20694526.